Study of the blistering phenomenon of molten glass in contact with refractories

Julien Hell

Université Grenoble Alpes

THÈSE

Pour obtenir le grade de

DOCTEUR DE L'UNIVERSITÉ GRENOBLE ALPES

Spécialité : **Matériaux, Mécanique, Génie Civil, Électrochimie**

Arrêté ministériel : 25 mai 2016

Présentée par

Julien HELL

Thèse dirigée par **Marlu César Steil**
Co-dirigée par **Isabelle Cabodi**

préparée au sein du **Laboratoire d'Électrochimie et de Physico-chimie des Matériaux et des Interfaces (LEPMI, Grenoble)**
dans **l'École Doctorale IMEP²**

Étude du phénomène de bullage des verres en contact des matériaux réfractaires

Thèse soutenue publiquement le **11 mars 2021**,
devant le jury composé de :

Mme Céline DARIE
Professeure, Université Grenoble Alpes, Présidente
M. Jorge FRADE
Professeur, Université d'Aveiro (Portugal), Rapporteur
M. Pierre-Marie GEFFROY
Directeur de Recherche CNRS, IRCER Limoges, Rapporteur
M. Michel GAUBIL
Ingénieur de Recherche, SEPR Le Pontet, Examinateur
M. Olivier CITTI
Ingénieur, Saint-Gobain Research Provence, Invité
Mme Isabelle CABODI
Ingénieure, Saint-Gobain Research Provence, Co-encadrante de thèse
M. Marlu César STEIL
Ingénieur de Recherche CNRS, LEPMI Grenoble, Directeur de thèse

STUDY OF THE BLISTERING PHENOMENON OF A GLASS IN CONTACT WITH REFRACTORIES IN GLASS FURNACES

Abstract

The interactions between glass melts and refractories in glass industry have a large impact on the final glass quality. One of the consequences of these interactions is the potential blistering phenomenon within the glass melt. It has been shown by various authors that the blistering results from electrochemical reactions. However, the proposed mechanisms are based on assumptions that appear highly questionable. The objective of this study is to define the key parameters of the blistering process and to propose a mechanism for blistering of soda–lime–silica glass melts in contact with fused-cast zirconia-based.

Physico-chemical and electrical characterizations of the studied refractories were performed during this thesis. Apart from the standard tests made in Saint-Gobain, XANES experiments to determine the redox state of the refractories and impedance spectroscopy measurements as functions of temperature and oxygen partial pressure to estimate the partial ionic and electronic conductivities were carried out. The studied refractories being bi-phasic composite materials composed of crystallized zirconia and a vitreous phase, X-ray tomography measurements were used to reconstruct the distribution of the two phases to assess their possible percolation and their tortuosity in three dimensions.

Original set-ups were realized during this work for in-situ studies of the blistering phenomenon like permeation set-ups working at temperature up to 1500°C coupled to mass spectrometer to study the transport through the refractory and allowing the temporal study of the blistering process and a sessile drop set-up to estimate the lifetime of the bubble.

Keywords

Bubbles, blistering, refractory, glass/refractory interface, zirconia, zircon, glassy phase, redox state, oxygen semipermeability.

Résumé

Les interactions entre le verre fondu et les réfractaires dans l'industrie verrière ont un impact important sur la qualité finale du verre. L'une des conséquences de ces interactions est le potentiel phénomène de bullage au sein du verre fondu. Il a été montré par divers auteurs que la formation de bulles résulte de réactions électrochimiques entre le verre et le matériau réfractaire tapissant les parois du four. Cependant, les mécanismes proposés reposent sur des hypothèses discutables. L'objectif de cette étude est de définir les paramètres clés du processus de bullage et de proposer un mécanisme de bullage du verre au contact de réfractaires à base de zircone fondue.

Des caractérisations physico-chimiques et électriques des réfractaires étudiés ont été réalisées au cours de cette thèse. En plus des tests standards réalisés à Saint-Gobain, des expériences XANES pour déterminer l'état redox des réfractaires et des mesures de spectroscopie d'impédance en fonction de la température et de la pression partielle d'oxygène ont été effectuées afin d'estimer les conductivités ioniques et électroniques partielles. Les réfractaires étudiés étant des matériaux composites biphasés à base de zircone cristallisée et d'une phase vitreuse, des mesures de tomographie aux rayons X ont permis de reconstituer la distribution des deux phases afin d'évaluer leur éventuelle percolation et leur tortuosité en trois dimensions.

Des montages originaux ont été fabriqués au cours de ce travail pour des études in-situ du phénomène de bullage, comme des montages de perméation fonctionnant à haute température (jusqu'à 1500°C), couplés à un spectromètre de masse pour étudier le transport à travers le réfractaire tout en permettant l'étude temporelle du bullage ainsi qu'un montage de goutte posée pour estimer la durée de vie de la bulle.

Mots-clés

Bulles, bullage, réfractaire, interface verre/réfractaire, zircone, zircon, phase vitreuse, état redox, semiperméabilité à l'oxygène.

Acknowledgements

Par ces lignes je souhaite remercier l'ensemble des personnes ayant contribué à ce projet entre le Laboratoire d'Électrochimie et de Physico-Chimie des Matériaux et des Interfaces (Grenoble) et Saint-Gobain Research Provence (Cavaillon).

Je tiens dans un premier temps à remercier l'ensemble des membres du jury qui m'ont fait l'honneur d'évaluer mon travail de thèse. Je remercie particulièrement Pierre-Marie Geffroy et Jorge Frade d'avoir accepté d'être rapporteurs de ce travail ainsi que Céline Darie d'avoir présidé ce beau moment d'échange scientifique.

Un grand merci à Marlu César Steil, directeur de cette thèse. Merci pour son accompagnement tout au long de ces trois années. Je tiens à le remercier pour toutes les compétences que j'ai pu acquérir grâce à son expérience dans le domaine des céramiques et de l'impédance complexe. Un énorme merci à Jacques Fouletier. Je rends hommage à sa connaissance de l'électrochimie et de la semiperméabilité. Merci pour son soutien sans faille tout au long de ce projet. Un merci tout particulier à Franck Fournet-Fayard pour sa disponibilité et son aide, pour tous les échantillons usinés, pour les réparations en urgence, le montage de nouvelles manip, etc.

Je remercie toute l'équipe SEFPRO de SGR Provence et SGR North America. Merci à vous de m'avoir transmis vos connaissances sur les matériaux réfractaires. Je tiens particulièrement à remercier Isabelle Cabodi, co-encadrante de cette thèse, et Pierrick Vespa. Merci à vous deux pour tous nos échanges et nos débats autour de ces bulles. Merci à Johan Combes pour la préparation des échantillons et tous les essais lancés à Cavaillon. Je remercie également Olivier Citti pour son expérience sur le sujet.

Un grand merci à Deniz Cetin pour nos nombreux échanges sur le sujet et sa connaissance sur les verres et les phases vitreuses, merci à Damien Boloré pour son partage d'expérience sur les bulles et à Darren Rogers.

Merci aux membres de SGR Provence, en particulier Maxime Mayer et Lugdivine Barbosa pour toutes les analyses microsonde. Merci à Paul Leplay pour m'avoir formé au traitement d'images. Merci à Magaly Diaz pour nos échanges sur la spectroscopie d'impédance. Merci à Jean-Marc Poujade pour tous les essais de bullage lancés sous vidéo.

Un grand merci à toutes les personnes de SGR Paris qui m'ont appuyé tout au long de cette thèse. Je remercie particulièrement Eric Janiaud et Guillaume Barba Rossa pour le partage de leur expérience sur les verres. Merci à Julien Durst et Sophie Brossard, pour les mesures et surtout les traitements des données XANES. Merci à Cécile Jousseaume, Alexandre Blanchet, Nicolas Bost et Fabien Faderne pour toutes les analyses qu'ils ont réalisées afin d'alimenter la compréhension du phénomène de bullage.

Je remercie les membres du Consortium des Moyens Technologiques Communs (Grenoble) pour toutes les caractérisations effectuées sur mes matériaux. Merci à Joëlle Masson, Frédéric Charlot, Rachel Martin, Francine Roussel et Thierry Encinas. Un grand merci à Stéphane Coindeau pour toutes les mesures tomographiques effectuées.

Merci également à Pierre Lhuissier pour la partie tomographie et surtout merci à Luc Salvo pour son aide précieuse sur l'interprétation des résultats.

Un grand merci à Olivier Proux pour son aide lors des premières mesures XANES et des traitements à l'ESRF. Merci à Emiliano Fonda et Andrea Zitolo pour leur appui lors des mesures XANES à SOLEIL.

Je remercie également Renaud Bouchet pour toutes les discussions que nous avons pu avoir sur les problématiques liées à mes mesures d'impédance complexe.

Un grand merci à Véronique Ghetta pour le partage de ses connaissances sur les expériences de goutte posée.

Je tiens également à remercier Jean-Louis Souquet et Alexander Pisch pour leur connaissance de la thermodynamique.

Merci à Céline Darie et Jean-Marc Chaix, membres du comité de suivi de ma thèse, de m'avoir accompagné au cours de ces trois années.

Table of Contents

Introduction

During the glass fabrication process, the contact between refractories and molten glass is sometimes leading to a blistering phenomenon within the melt. This blistering phenomenon occurs at several levels of intensity, depending on the glass/refractory couple and on the external conditions. In order to avoid the blistering and, consequently, defects in final products, it is crucial to identify the different parameters playing a role in this phenomenon. The objective of this thesis is to propose a scenario to the blistering phenomenon. My thesis work was carried out as part of a collaborative research project between Saint-Gobain Research centres (SGR North-America, SGR Paris, SGR Provence) and the LEPMI in Grenoble, a laboratory specialized in electrochemistry of solid.

Special glasses require very high final quality since they are used in applications requiring perfect transparency without any defect: solar cells, television screen, smartphone screen, etc. Due to their composition, they undergo very high melting temperature during their process. This is why the materials constituting the walls of the glass furnaces must withstand high stresses. Refractory materials capable of maintaining their properties up to very high temperatures are used. In addition to thermal stresses, a refractory material in a glass furnace also undergoes chemical, thermomechanical and electrical stresses [1]. According to ISO/R836 or AFNOR NF B 40-001 standards [2]: "Refractory materials are materials and products other than metals and alloys (without excluding those containing a metallic component), whose pyroscopic resistance is equivalent to 1500°C minimum". Indeed, depending on its position in the furnace, the refractory material is in contact with temperatures varying from 1000°C to 1600°C. This is why this material must have a high refractoriness as well as a low thermal conductivity.

At very high temperatures, glass is extremely corrosive [3]. The refractory material therefore undergoes direct chemical attacks when it is in contact with the molten glass but also because of the carryovers generated by the mixture of the powders of raw materials. The refractory material inside the furnace suffers thermomechanical stresses due to a very strong thermal gradient between the inside and the outside of the furnace. Note that, for example, a float furnace is around 70 meters long and the melting tank

can reach up to 500 m^2. This represents a significant number of refractories that have to be properly chosen for each part of the furnace which has its specificity in the glass production process [4].

The choice of refractories is crucial since they constitute much of the cost for a glass furnace; moreover, they define the campaign duration [5]. A campaign is the operating time between two total demolition of the furnace, it lasts between 2 and 20 years depending on the type of glass produced, the cumulative output (tonnage of glass produced) and the type of furnace. As the replacement of refractories often requires the complete shutdown of the furnace and therefore of the production for many months, the longevity of refractories is a key parameter for glassmakers. Glassmakers want to produce a good quality glass, for a considerable time and this at the best price. The refractory materials are then carefully chosen for each part of the furnace in order to combine the best price with good resistance over time without generating defects in the glass. The glass contact area in the melting tank is the most strategic area of the furnace because in most cases it is the state of the refractories at this location which determines the quality of the glass as well as the lifetime of the furnace. This is the place where the refractories are subjected to very high temperatures and strong thermal convection currents [6-10].

Many studies have already been performed in the last 45 years by SEFPRO (company of the Saint-Gobain group) to better understand the blistering phenomenon at the glass/refractory contact, especially on fused-cast refractories. The various theories found in the literature to explain the blistering process are up to now under debate.

The present knowledge and theories on bubbles formation at the glass/refractory interface are presented in Chapter 1. The studied materials and the experimental methods are then detailed in Chapter 2. The electrical and transport properties of the refractories studied during this work are described in Chapter 3. Chapter 4 is devoted to the study of the key parameters of the blistering. Finally, the blistering scenarios are presented in Chapter 5, with some perspectives about the future studies which could be performed.

Chapter I: Present knowledge on bubbles formation at the glass/refractory interface

I.1 ORIGINS OF BUBBLES IN GLASS

During the glass making process, raw materials are mixed as powders before being melted. Dissolution of powders is a complex phenomenon and is the place of a large number of chemical reactions [11]. Molten soda-lime-silica glass (taken as example as it is the most produced one) is obtained, among other things, from carbonaceous raw materials such as $CaCO_3$ and Na_2CO_3. Glass melting process involves the release of CO_2 gases in the melt by decomposition reactions during the fusion of these raw materials ($CaCO_{3(s)} \rightarrow CaO_{(s)} + CO_{2(g)}$ and $Na_2CO_{3(s)} + SiO_{2(s)} \rightarrow Na_2O{\cdot}SiO_{2(s)} + CO_{2(g)}$) and H_2O vapor (due to the previous humidification of the powders). In order to remove the bubbles from the melt (glass refining), the size of all gaseous inclusions is increased, enhancing the buoyancy-driven ascension [12]. Fining agents are added in the batch composition to improve bubbles removal. Sodium sulfate (Na_2SO_4) is the most used chemical fining agent in flat glass industry. Bubblers are also used in furnaces to add bubbles in the melt and make them coalesce faster. Fining step is essential to obtain a bubble-free melt with a low tendency toward gas reboil. Reboil of gases is caused by sudden changes in temperature or in redox state; gases present during the glass melting are dissolved up to the limits of their solubility and appear again as bubbles while reaching a critical temperature, since the gas solubility decreases with increasing temperature [13]. Addition of fining agents leads to redox reactions at high temperatures, producing gases that diffuse into carbonate or water bubbles formed earlier in the melting process: the so obtained larger bubbles ascend more easily to the surface of the melt. While reaching the surface of the melt, bubbles burst and remove the gas out of the glass melt. Another important effect of refining gases is to enhance the complete dissolution of powders, by stirring continuously by convection (Figure 1) the melt in the whole batch [14].

Figure 1: Illustration of the convective movements enhanced by the blistering in a champagne glass as a comparison of the stirring phenomenon in a glass furnace [15].

At the end of the fining step, the liquid is almost entirely homogeneous, but it can still contain small bubbles of O_2 and SO_2 which did not have time to rise. The glass is then in the second part of the furnace where the temperature gradually decreases. As a result, the solubility of the gases in the melt increases, and the small bubbles present dissolve in the glass [12]. This stage constitutes the secondary refining [16]. The glass cooling step is relatively critical in order to obtain a final product without any defects. It is important that the duration of this step is sufficient to complete the dissolution of all the remaining bubbles. In fact, insufficient temperature control can lead to the formation of hot spots which could be the source of a local decrease in the solubility of gases and therefore of possible reboil. The bubbles resulting from this phenomenon do not have time to dissolve again in the glass and therefore constitute a defect in the final product [17].

This thesis is devoted to the study of the role of the glass/refractory interface on the blistering phenomenon. Consequently, all these bubbles formation processes are not directly included in our problematic. However, they have to be kept in mind since an insufficient fining process or a reboil phenomenon may play a role in our experimental results and interfere in the interpretation of the observed phenomena.

I.2 GAS SOLUBILITY IN GLASS

I.2.1 Introduction

Molten glass has the ability to react with gases (chemical dissolution) or to dissolve them physically (physical dissolution) [18]. The solubility of gases (like oxygen, nitrogen, carbon dioxide and sulfur dioxide) in glass melt is defined, like in other liquids, as the equilibrium concentration of dissolved gases in the melt at a given gas pressure and temperature [19, 20]. If the melt is supersaturated by a gas, bubbles nucleation in molten glass is susceptible to occur [21]. Supersaturation occurs, when the total equilibrium gas pressure of the dissolved gases, exceeds 1 bar.

The solubility of gases in a glass melt depends on temperature, glass composition and gas fugacity. These factors, as well as the transport of dissolved gases by diffusion, are of great importance to gas release and gas absorption mechanisms in melting and refining steps. Additionally, the amount and the type of dissolved gases in glasses can influence the properties of these glasses. For instance, it can influence density, viscosity, thermal expansion, surface tension and refractive index [18].

I.2.2 Bubbles nucleation in glass

Supersaturation and nucleation are the two key parameters to form bubbles. In this manuscript, nucleation is used to describe a process leading to the formation of a bubble. The bubble nucleation process involves two stages, the stage of nucleation itself and the stage of nucleus growth. A bubble nucleus may be understood as a cluster of gas molecules. The necessary condition for the formation of a stable nucleus is to reach the critical value of Gibb's enthalpy [22] (Figure 2).

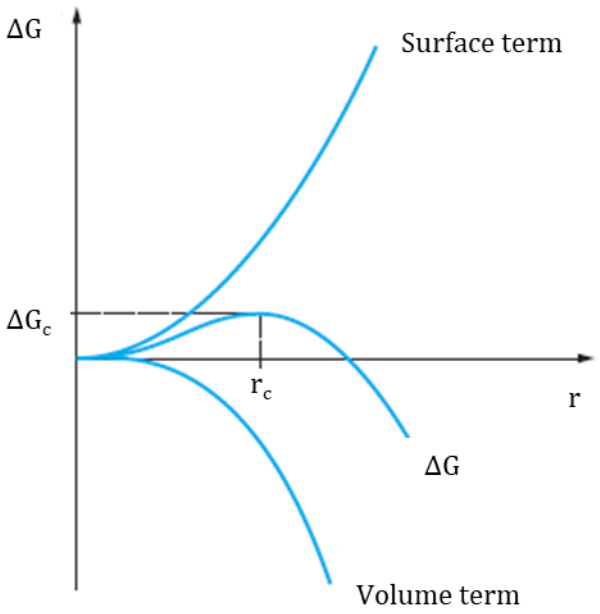

Figure 2: Enthalpy as a function of the bubble radius, with r_c the critical radius associated to the critical enthalpy ΔG_c to form a bubble [23].

As the formation of a new phase in a glass melt requires breaking several neighbouring strong bonds of Si–O, the supersaturation of the melt by the concerned component is needed [21]. In the absence of pre-existing gas cavities, bubble nucleation requires exceedingly high levels of supersaturation. Nucleation is favoured at the location where the dissolved gas concentration is the highest. At low levels of supersaturation, however, gas bubbles only nucleate within the liquid at pre-existing metastable gas cavities, in the vessel surface in contact with the liquid, on suspended particles or from metastable micro-bubbles in the liquid bulk [24]. To create bubbles within a liquid phase, it is necessary to overcome the cohesive forces connecting the molecules of the melt (surface-tension). The nucleation theory is based on the evaluation of the minimum energy brought to the system to create gas bubbles. If the bubbles appear in the liquid phase bulk, a homogeneous nucleation has to be considered. If the bubbles appear on the walls of the container, heterogeneous nucleation has to be referred.

I.2.3 Bubbles behaviour in glass

Bubbles of various sizes exist in the molten glass. Since some of the gases originally contained in the bubble are dissolved in glass melt and others diffuse into the bubbles, the number of bubbles and the gas composition in the bubble change gradually with melting time [16, 20, 25, 26]. Fining process has three tasks: (i) eliminate the residual bubbles, (ii) homogenize the melt through the bubbles motion and (iii) decrease the amount of dissolved gases in the melt to avoid reboil. In the case of typical melts with bubbles smaller than 0.2 mm in diameter, the velocity of rise is too small to eliminate bubbles during usual tank residence times. Consequently, fining process is a critical step to enlarge the bubble diameter, since the radius (r) is a decisive parameter in this equation (see equation (4)). If the bubble is big enough, bubble rises to the surface of the melt.

Hadamard, Rybczynski and Němec, determined the rising velocity of a spherical gas bubble in an infinite fluid medium [27, 28]. Three forces act over the bubble in a melt: the Archimedean buoyant force (Π); the thrust force (T); and the Stokes' law (F) an opposing force to the movement of the bubble applied by the melt (only valid if far enough from the walls [28]).

$$\Pi = m_{gas}\, g = V_{gas}\, \rho_{gas}\, g = \frac{4}{3}\, \pi\, r^3\, \rho_{gas}\, g \qquad (1)$$

$$T = -V_{gas}\, \rho_{glass}\, g = -\frac{4}{3}\, \pi\, r^3\, \rho_{glass}\, g \qquad (2)$$

$$F = -6\, \pi\, r\, \mu_{glass}\, \vartheta \qquad (3)$$

- r is the bubble radius,
- ρ_{glass} is the density of glass,
- ρ_{gas} is the density of gas in a bubble,
- g is the gravity acceleration,
- ϑ is the ascension velocity of the bubble,
- μ_{glass} the dynamic viscosity of the molten glass,

It should be noted that bubbles do not exactly rise as solid spheres and a correction should be applied as explained by Greene [29]. However, it can be assumed that the laminar flow around the bubble maintains, at a first approximation, a spherical shape of the bubble. Using equations (1) to (3) with Π = T + F, the ascension velocity of a bubble is described as:

$$\vartheta = \frac{2\,(\rho_{glass} - \rho_{gas})\,g\,r^2}{9\,\mu_{glass}} \qquad (4)$$

Considering that the density of the bubble is very low compared to the density of the molten glass ($\rho_{glass} >> \rho_{gas}$), the expression for the ascension velocity (rate of ascent) of a bubble in a viscous liquid becomes [20, 27]:

$$\vartheta = \frac{2\,\rho_{glass}\,g\,r^2}{9\,\mu_{glass}} \qquad (5)$$

This equation gives the influence of the parameters that enhance the removal of the bubbles. Indeed, viscosity must be as low as possible, which is possible while changing the composition or increasing temperature of the medium. To further decrease the process duration, it is also possible to increase the size of the bubbles with a fining agent.

According to equation (5), the lower the viscosity of the glass, the faster the rising velocity. As the viscosity of glass decreases exponentially with temperature, as shown in Figure 3.

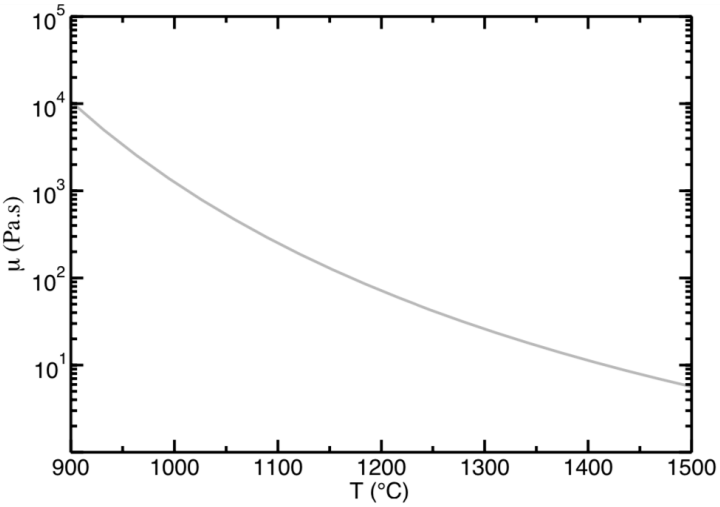

Figure 3: Viscosity as a function of the temperature for an ordinary soda-lime-silica glass (75 wt.% SiO_2 – 15 wt.% Na_2O - 10 wt.% CaO) [27].

Knowing the viscosity and the density of the glass, and assuming that the bubble diameter does not change, it is possible to estimate the time necessary for a bubble to escape from the molten glass. Surface tension and contact of the bubble with other elements like the walls are not considered in this calculation. Assuming that the bubble is a rigid sphere to simplify calculations, the rising rate of a bubble, with a radius of 0.1 mm and a glass viscosity equal to 10 Pa.s at 1450°C, is less than 50 cm/day [29]. Table 1 shows that the rising velocity decreases considerably with temperature.

Table 1: Time (in hours) needed to rise 1 meter or 5 mm for a bubble with a 0.1 mm radius in an ordinary soda-lime-silica glass.

	1450°C	1200°C	1100°C
Density ($kg.m^{-3}$)	2450		
Viscosity (Pa.s)	10	70	300
Time to rise 1 m (hours)	52	364	1561
Time to rise 5 mm (hours)	0.3	1.8	7.8

This long bubble life-time is an important parameter in glass process, but also while studying the influence of a parameter on the blistering phenomenon, as it will be shown in Chapter 4. Table 2 gives a comparison between the rising times of a bubble of 0.1 mm in radius in different media.

Table 2: Comparison of time (in hours) needed to rise 1 meter for a bubble with a 0.1 mm radius in different media.

	Glass	Water	Oil
	1100°C	20°C	20°C
Density ($kg.m^{-3}$)	2450	997	900
Viscosity (Pa.s)	300	0.001	0.1
Time to rise 1 m (hours)	1561	0.01	1.4

I.3 OXYGEN BUBBLES

Oxygen gas is present in molten glass in three forms [16]: molecularly dissolved, ionic oxygen chemically bonded to variable-valence ions or in gas bubbles. As explained previously, oxygen can be absorbed in glasses containing polyvalent ions by reacting with the lower valence forms of the elements in the glass. Therefore, the ability of molten glass to absorb oxygen is related to the quantity of reduced iron since the amount of oxygen absorbed by glasses increased with the ferrous ion concentration in the melt [25]. Indeed, the shrinkage rate of an oxygen bubble increases with the reduced (ferrous) iron content. As a bubble shrinks, gas is transported from the bubble to the melt [30]. One critical conclusion for glass melting is that the redox state of iron at high temperature is mainly driven by oxygen transfer [31].

The rate of bubble dissolution depends also on the difference in gas concentration at the melt/bubble interface and on the gas concentration in the melt. If this difference is large, the bubble dissolves rapidly. Bubbles can shrink by the diffusion of gases from the bubble into the glass melt if the melt is undersaturated [20]. Consequently, the growth or shrinkage of bubbles in molten glass is determined by diffusion and redox reactions of oxygen gas in the melt.

I.4 INTERACTIONS BETWEEN GLASS AND REFRACTORY

Refractory quality is crucial because it influences the lifespan of the furnace and the final quality of the glass product. Most of the studies about glass/refractories interactions found in the literature were performed on AZS (Al_2O_3 – ZrO_2 – SiO_2) fused-cast products. The contact zone, between molten glass and ceramic refractory, is subjected to high temperatures and very complex physico-chemical interactions; the molten glass being described as a chemically active ionized liquid [32].

Diffusion and dissolution interactions between molten glass and refractory occur at high temperature. Indeed, at the interface, the refractory is enriched through diffusion of glass elements (as Na_2O or CaO in the case of sodalime glass) whereas glass is enriched in refractory elements (mainly Al_2O_3 and ZrO_2 for AZS) [33, 34].

The main chemical interactions of the molten glass with the refractories are ascribed to the action of the alkali ions initially present in the glass composition. The penetration of these ions into the refractory occurs through the vitreous phase. It means the refractory is mainly enriched in Na_2O and CaO content in its vitreous phase at the interface and its composition is slowly decreased in Al_2O_3 and ZrO_2. This area between the initial glass composition and the initial refractory composition is described as a "glassy reaction layer", which is the result of these diffusion and dissolution processes reaching a saturation concentration in this area to form a "new compound" (Figure 4).

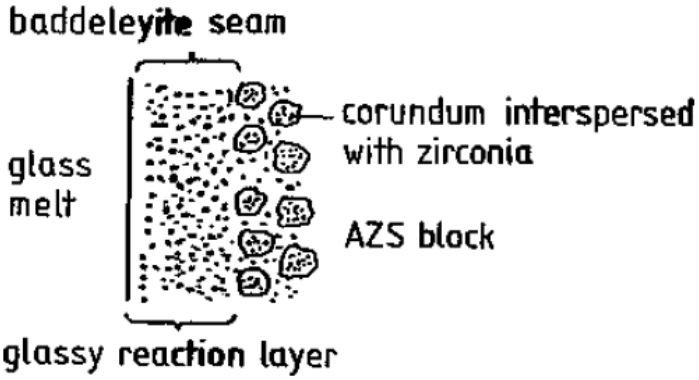

Figure 4: Diagram of the interaction layer at the glass/refractory interface [34].

The chemical reactivity and so the diffusion and dissolution processes are increased with the high temperatures of the furnace, but also with the convection movements in the glass tank and the contact time between glass and refractory [1, 35].

This diffusion phenomenon through the molten glass/refractory interface is divided into 3 regions at the direct surface of the refractory. It means in a thin layer (around 500 µm) of the glass in contact with the refractory block:

1. Directly in contact with the surface of the refractory, creation of a "diffusion layer" in which the molten glass is enriched with molten particles of the refractory.
2. At a short distance from the glass/refractory interface, a constant distribution of molten particles of the refractory is observed.

3. At a greater distance from the glass/refractory interface, the concentration of dissolved refractory is negligible and the glass chemistry is the one of the sane glass.

All these studies were carried out with AZS products, whereas our study on the fused-cast products is performed on high zirconia fused-cast products. In the case of high ZrO_2 content refractories, a different interface is created by a higher ZrO_2 content and a very low level of Al_2O_3 in the region in contact of the glass and the refractory. By increasing the zirconia content in the fused-cast products, as the dissolution of ZrO_2 is lower than those of Al_2O_3 in the glass, the corrosion rate of furnaces walls is globally decreased [36].

Surface phenomena play an important role in the breakdown of the refractories in glass furnaces, especially due to corrosion or exudation as a result of the complex interactions between glass and refractory. Exudation is the expulsion of vitreous phase from the product when it rises in temperature [37]. These interactions are also changing the molten glass composition ("knots") or introducing insoluble defects ("stones") in glass that have to be avoided. Knots are made of vitreous particles with a different chemical composition compared to the glass. It leads to a different index of refraction, inducing a local lens effect. Stones are solid recrystallized or un-melted material inclusions in the glass melt that are found in the final product.

Besides, the blistering phenomenon studied in this thesis and occurring at the molten glass/refractory interface may also lead to problems in the glass making industry. All these defects in the final glass products may cause some production losses by rejecting products due to the presence of extremely small bubbles, knots or stones. The origin of the blistering phenomenon is explained in the following parts. However, surface phenomena have to be kept in mind since it is impossible for a bubble to appear in a homogeneous molten glass. In this case, the formation of a bubble involves necessarily the creation of new surfaces in the bath [38].

I.5 BLISTERING SOURCES IN GLASS IN CONTACT WITH REFRACTORIES

According to the literature, several parameters lead to the blistering phenomenon [39]: the porosity or the cracks of the refractories, a poor refining stage before removal from the furnace, impurities present in the glass, electrochemical reactions between the glass and the refractory, etc. It should be pointed out that the blistering mechanism is still not well understood.

I.5.1 Influence of refractory manufacturing on the blistering phenomenon

During the refractory manufacturing process, gas bubbles can be captured in the refractory matrix creating pores inside the material. The pores are divided into two categories: open porosity and closed porosity. For open porosity, pores are percolating. Whereas, for closed porosity, pores are isolated in the material structure. While the refractory is used in the glass furnace, it is subjected to various stresses leading to corrosion. This corrosion can open the pores contained in the material releasing gases in the glass. These released gases in the glass lead to bubble formation [39]. It turned out that closed pores in the refractory could contain nitrogen, hydrogen and carbon dioxide depending on the refractory making process [40]. However, fused-cast refractories are generally very dense materials with low porosity rate (less than 5% of total porosity). Then, the corresponding quantity of gases released is low.

Open pores or cracks in the refractory structure may lead to an external air source into the molten glass to form bubbles. This phenomenon generates bubbles only in localized areas.

Other studies trying to explain the blistering phenomenon can be found with AZS products. Reboil of gases (in vitreous phase in this case) of an AZS products is caused by sudden changes in temperature and can be the source of bubbles in glass. Gases dissolved during melting and casting in AZS up to the solubility limits are leading later to a blistering of the glassy phase, while the temperature is increased and the gas solubility is decreased. However, this phenomenon takes place only during the first heating of the furnace in the concerned area [41, 42]. Gases released in the glassy phase

of the AZS blocks can only exit through the high viscous "reaction zone" defined previously. The strong increase of the saturated layer in Al_2O_3 and ZrO_2 content, associated with the decrease of SiO_2 and Na_2O content, lead to an increase of the viscosity and the surface tension of this layer in comparison to the sane glass [34]. The surface tension of the glassy phase is higher than the one of the molten glass. This is why the bubble nucleation occurs at the limit between the refractory and the glass. However, for HZFC refractories in contact with glass melt, lower glass defects are observed since these refractories are composed of lower content of glassy phase and do not exudate as much as AZS products [43]. This could possibly generate blistering but in a very temporary way at the first heating of the refractory. No further changes in the redox states of polyvalent ions and so no more blistering can occur after a certain time [44]. This temporary phenomenon is not responsible of high continuous blistering as observed at the glass/refractory interface. Gas desorption of previously adsorbed gases at the refractory surface can also cause the blistering phenomenon: gas molecules previously adsorbed on the heterogeneous surface of the refractory are detached and liberated in the molten glass [45]. However, this bubble source is only momentary during the first contact with molten glass.

I.5.2 Electrochemical reactions between glass and refractory

At the beginning of the thesis, the only consistent theory to explain the blistering phenomenon was the one proposed by F.G.K. Baucke [46]. Later on the proposed mechanism has been taken up in van Dijk's thesis [39]. The Baucke's experiments have been carried out on zircon (ZS: $ZrSiO_4$) materials of high density (less than 3 % porosity) and the glass melts were alkali calcium silicates. $ZrSiO_4$ is considered, at high temperature, as a poor mixed ionic/electronic conductor (Na^+ and electrons) ascribed to impurities such as Fe_2O_3, TiO_2 and Na_2O. Van Dijk's experiments have been carried out on fused cast AZS (Al_2O_3 (45-51 wt.%) – ZrO_2 (32-41 wt.%) – SiO_2 (12-16 wt.%)), including 1 wt.% Na_2O and 0.2 – 0.3 wt.% CaO, Fe_2O_3, TiO_2, MgO. The glassy phase of AZS refractory (17 – 21 wt.%) consisted of ca. 70 wt.% SiO_2, 4 wt.% Na_2O, 22 wt.% Al_2O_3 and 3 wt.% ZrO_2.

The main experimental result reported by Baucke is schematized in Figure 5 and Figure 6. When a cube of ZS with two layers – an oxidized flesh-colored material and a less oxidized light-grey material (Figure 6 a) – was immersed in a molten glass, as shown in Figure 5, oxygen bubbles in the glass evolved only on the oxidized surface of the refractory.

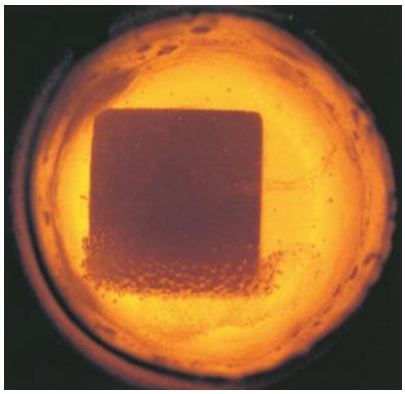

Figure 5: At 1230°C, oxygen bubble formation was only observed on the oxidized surface of the zircon pellet immersed in glass [47].

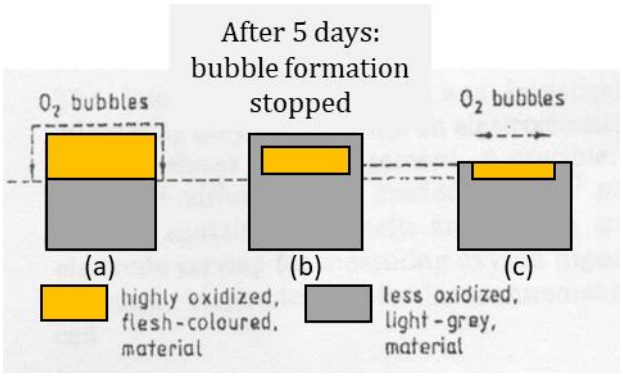

Figure 6: Illustration of the blistering phenomenon on ZS refractories, according to F.G.K. Baucke [46].

After a few days, bubble formation stopped and, as illustrated in Figure 6 (b), a grey layer was formed on the cube. After cutting off the grey layer (Figure 6 (c)), oxygen bubbles in glass evolved again on the oxidized surface of the refractory.

The proposed mechanism is based on an electrochemical process at the interface between ZS and the glass melt, as schematized on Figure 7. The formation of oxygen bubbles results from an oxidation of oxide ions of the glass melt by impurities dissolved within zirconium silicate refractories, such as Fe(III). Baucke considers that the blistering phenomenon can be explained according to an electrochromic mechanism [48], i.e. the oxidation and reduction reactions do not take place at the same interface. It is assumed that the oxidation takes place at the ZS/glass interface and the reduction of Fe(III) at the interface between a reduced zone and the oxidized ZS. Consequently, a reduced layer is growing within the ZS bulk. The reaction rate is controlled by solid state diffusion of charge-balancing alkali ions.

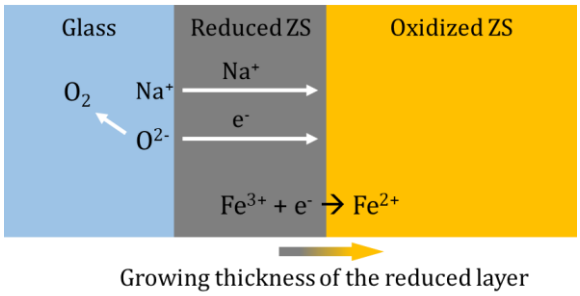

Figure 7: Scheme of the blistering phenomenon at the interface between zircon refractory and a molten glass.

However, the proposed mechanism is based on assumptions that appear questionable. The global electrochemical reaction [46, 49]:

$$4Fe^{3+}_{(refractory)} + 2O^{2-}_{(glass)} \leftrightarrow 4\ Fe^{2+}_{(refractory)} + O_2(g)_{(glass)} \qquad (6)$$

requires that Fe^{3+} ions are more oxidizing than oxygen O_2. A few attempts to compare the electromotive force (emf) of redox systems involved in glass industry at high temperature have been published. Rüssel [50] has determined the standard emf of various couples by voltammetry, at 1100°C, in soda-lime glasses (see Table 3). As an example, at 1100°C, Sb^{5+} can oxidize O^{2-}, which is not the case of Fe^{3+}.

Table 3: Example of standard potentials measured by voltammetry, at 1100°C, in a glass melt (74 SiO_2 – 16 Na_2O – 10 CaO).

Redox couple	E° (V vs. YSZ/Pt, O_2, (pO_2 = 0.21 bar))
Ce^{4+}/Ce^{3+}	+ 0.08
Sb^{5+}/Sb^{3+}	+ 0.05
Cr^{6+}/Cr^{3+}	+ 0.03
O_2/O^{2-} (pO_2 = 0.21 bar)	0.00
Sn^{4+}/Sn^{2+}	- 0.11
Ag^+/Ag^0	- 0.37
Fe^{3+}/Fe^{2+}	- 0.56
Ni^{2+}/Ni^0	- 0.59

Rüssel also determined the variation of the standard potential of these polyvalent pairs as a function of temperature (see Figure 8).

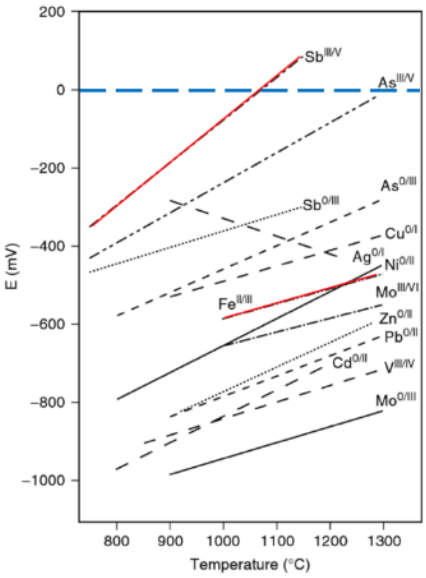

Figure 8: Variation of the standard potential of various couples of polyvalent ions as a function of temperature, E in mV vs. YSZ/Pt, O_2 (pO_2 = 0.2 bar).

This result indicates that at temperatures higher than 1400°C, only Sb^{5+}/Sb^{3+} and As^{5+}/As^{3+} exhibit a positive standard potential vs. O_2 (pO_2 = 0.21 bar)/O^{2-} pair and the Fe^{3+}/Fe^{2+} standard potential is approximately - 0.45 V vs. O_2 (pO_2 = 0.21 bar)/O^{2-} pair. Consequently, Sb^{5+} and As^{5+} can oxidize O^{2-} in molecular oxygen and are used as fining agent. However, according to these results, Fe^{3+} cannot oxidize O^{2-}. Rüssel's results have been confirmed more recently by De Best [20] who carried out voltammetry experiments on glass (75 SiO_2 - 15 Na_2O - 10 CaO) containing 0.4 wt.% Fe_2O_3 (see Figure 9). There is a pretty good agreement between the standard potential of the Fe(III)/Fe(II) couple obtained independently by these authors. Moreover, the variation vs temperature of the standard potential Fe_2O_3/FeO in their solid form is plotted in Figure 9. For temperatures higher than 1000°C, a good agreement is observed. According to Rüssel et al. [51] this agreement could be ascribed to clustering of iron in the molten glass. These clusters would have similar properties to those of crystalline species, i.e., Fe_2O_3 and FeO.

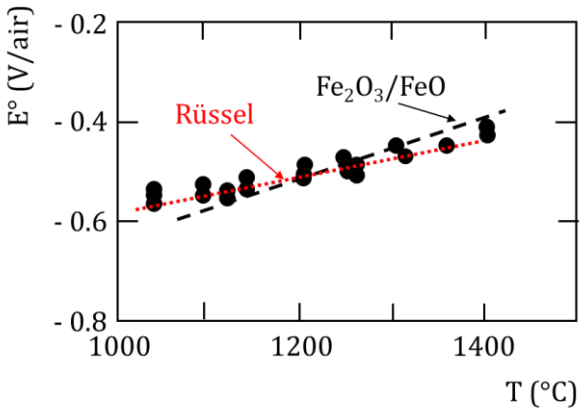

Figure 9: Variation of the standard potential of the Fe^{3+}/Fe^{2+} couple in glass containing 0.4 wt.% Fe_2O_3 as a function of temperature. The calculated standard potential of the Fe_2O_3/FeO system in solid form, and the results obtained by Rüssel [51] (see Figure 8) are plotted for comparison, from de Best [20].

Considering a redox pair, such as Fe^{3+}/Fe^{2+}, it is well known that increasing the basicity of the melt enhances the stability of the upper oxidation state at the expense of the lower. As demonstrated by Baucke and Duffy [52], the reason is that increasing the basicity rises the power of the oxide ions to donate their charge clouds to the metal ions which becomes instable. By losing this excess negative charge they acquire a higher oxidation state. The electron density on the oxide ions can be viewed as the basicity in the Lewis sense. Using this approach, Duffy et al. [53-55] defined the optical basicity: the optical basicity, Λ, is determined by UV spectroscopy from the position of the peak corresponding to the 6s - 6p energy transition of Pb^{2+} added as an O^{2-} ion probe in the glass. It can be calculated or measured using an appropriate probe, from the composition of the melt. Baucke and Duffy [56] determined the variation of the redox ratio (R) of lower to upper states of polyvalent ions vs. optical density, at 1400°C, under air atmosphere for various redox couples. Figure 10 shows the plot for the $[Fe^{2+}]/[Fe^{3+}]$ redox system. A linear relationship was obtained, i.e.,

$$log\ R\ =\ log\ \frac{[Fe^{2+}]}{[Fe^{3+}]}\ =\ 3.2 - 6.5\ \Lambda \quad (7)$$

For an optical basicity of 0.57, at 1400°C, under air, the redox ratio is ca. 0.31. Consequently, from a thermodynamical point of view, Fe^{3+} cannot oxidize O^{2-} ions, according to equation (5).

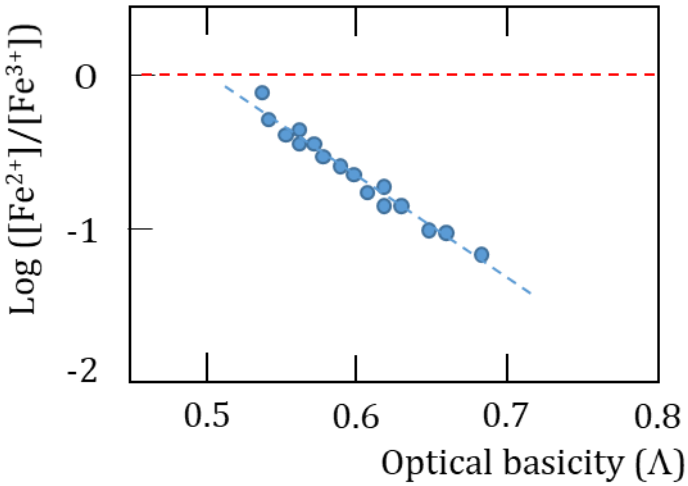

Figure 10: Relationship between redox ratio of lower to upper states and optical basicity in silicate melts, at 1400°C and air atmosphere, for Fe^{3+}/Fe^{2+}, from Baucke and Duffy [56].

Following another approach, Pinet and Di Nardo [57-59] obtained similar results. These authors proposed a classification of the redox couples, based on a characteristic oxygen pressure ($p(O_2)_{Charac}$) which corresponds to the oxygen partial pressure for which the concentrations of reduced and oxidized forms of the couple are equal. The quantity $p(O_2)_{Charac}$ depends mainly on the redox couple considered, on the basicity and on the temperature of the glass melt. It may be defined as follows:

$$log\,\frac{[Red]}{[Ox]} = \frac{n}{4}[\log p(O_2)_{Charac} - \log p(O_2)] \qquad (8)$$

where n is the number of electrons involved in the redox equilibrium.

When log $p(O_2)$ is higher than log $p(O_2)_{Charac}$, $\frac{[Red]}{[Ox]}$ is lower than 1. In Figure 11 is plotted the variation of the characteristic oxygen pressure vs temperature in glasses with the same level of basicity. At 1400°C, the characteristic oxygen pressure for the Fe^{3+}/Fe^{2+} couple is ca. 10^{-3} bar. Consequently, under air, the redox ratio is noticeably lower than 1: under equilibrium, at 1400°C, $\frac{[Fe^{2+}]}{[Fe^{3+}]}$ is less than 0.27, which is very close to the value estimated by Baucke et al, i.e., 0.31.

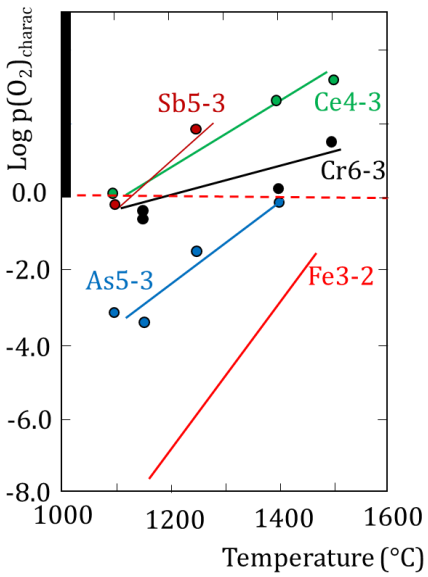

Figure 11: Variation of the characteristic oxygen pressure vs temperature in glasses with the same level of basicity (optical basicity: 0.57 ± 0.02), from Di Nardo et al. [58].

All these results, which are consistent despite different and sometimes empirical approaches, disagree with the hypothesis of Baucke, i.e., Fe^{3+}, thermodynamically, cannot oxidized O^{2-} to form molecular oxygen.

1. Baucke assumes that at the oxygen rich side of the refractory, the electrode is blocking for ions, i.e., under short-circuit of the cell or during cathodic polarization of the electrode, only electrons are flowing across the interface. Consequently, with this hypothesis, even if ZS is considered as a mixed ionic-electronic conductor, no flux of matter can be considered through the oxidized refractory. This result is the basis of the Baucke's model. However, as it will be reported later on, we demonstrated that the interface ZS/Air is not blocking for ions (see Section 4.3.2). Consequently, a flux of matter through the "oxidized" zone could be considered. It should be also recalled that if the external electrode in contact with air is blocking for ions, this electrode cannot be used for measuring the oxygen fugacity as assumed by these authors (see Figure 3 in reference [46]).

2. Another hypothesis underlying Baucke's model is that the dissociation of zircon, at the ZS/glass melt interface, to form ZrO_2 and SiO_2, is excluded. However, we have demonstrated that in contact with alkaline glass a rapid decomposition of zircon is observed.

3. The reaction layer below the ZS/glass melt interface has been observed mainly visually: from a "flesh-coloured" to "light-grey", with a sharp boundary. No investigation indicating the possible formation of new phases has been carried out. The reaction layer (200 µm thick, in 24 hours) was only analysed by electron microprobe, indicating an increase of the sodium ion concentration. However, the author himself indicated a possible penetration of sodium through the porosity of the ZS refractory.

As recalled previously, Van Dijk's experiments have been carried out on AZS electro-fused refractories. However, the proposed model was an adaptation of Baucke's one. Van Dijk considers, as Baucke did, that redox reactions involving iron and titanium lead to the generation of oxygen bubbles and that the reaction rates are controlled by the diffusion of cations of the glass melt into the refractory material. It is wrongly assumed that "the diffusion of cations transports a positive charge in the AZS, which is balanced by electrons moving simultaneously from the glass melt/AZS interface into the AZS interior. The electrons shift the Fe^{3+}/Fe^{2+} ratio and O_2 is formed, as long as there is cation diffusion". Electrochemical measurements (voltage measurements, short-circuit of the cell, and external polarization) do not at all demonstrate the validity of the proposed mechanism.

In addition, not only iron impurity is described in past studies as influencing the blistering tendency. Carbon impurities in refractories could also be a blistering source [60]. Regarding the studies, the more carbon content, the more bubbles created at the glass/refractory interface. [45, 60]. With carbon impurities, blistering could occur and, in this case, Fe_2O_3 would play an essential role: $C + 2\,Fe_2O_3 = CO_2 + 2\,FeO$. Carbon impurity is mostly caused by the use of graphite electrodes during the fused-cast process. It is one of the most-prone to blistering impurity in the refractory composition [61, 62]. Its presence leads to a reduced refractory material increasing the porosity rate at high temperature since the exudation occurs at lower temperature than for an oxidized refractory. Moreover, closed porosity in fused-cast refractories and the presence in the pores of impurities may significantly increase the number of bubbles in the glass. Therefore, reducing the content of impurities is a necessary condition to improve the quality of glass produced with the use of fused-cast refractories [40].

I.6 PREVIOUS RESULTS

The blistering phenomenon of glass in contact with refractories can happen in industrial glass furnaces in some specific conditions of use. Several methods have been developed at laboratory scale in order to observe that phenomenon [63]. The three main tests are presented in Figure 12: “Bossard test”, “Le Pontet test” and the “self-crucible test”.

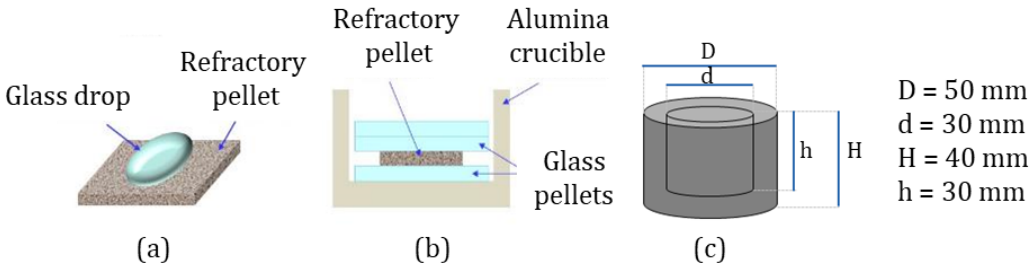

Figure 12: Blistering characterization methods: (a) Bossard test, (b) Le Pontet test and (c) self-crucible test [63].

In Bossard test, a piece of glass is melted on a piece of refractory. It means the glass and the refractory are in contact with the furnace atmosphere.

In Le Pontet test, a piece of the refractory is set in between pieces of glass into an alumina crucible. In this case, the refractory is not in contact with the furnace atmosphere because it is completely immersed in the molten glass.

The self-crucible test allows the best post-mortem observations and characterizations of bubbles, interface and refractory bulk.

Other experimentations with innovative set-ups have been performed to study the influence of the external surface atmosphere (Figure 13). They are described later on.

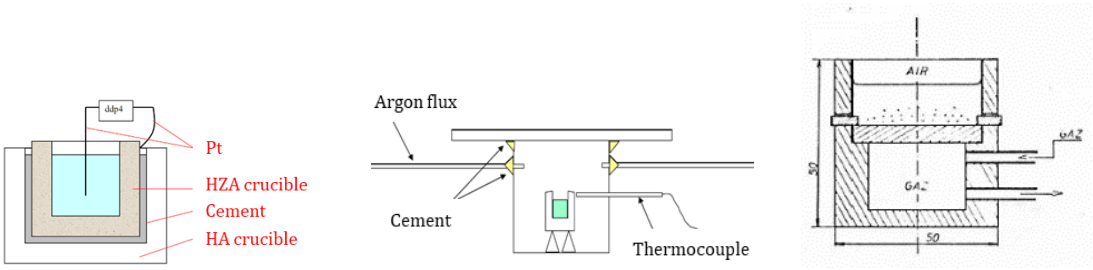

Figure 13: Various set-ups used to study the influence of the external atmosphere [64, 65].

Results of previous studies performed by SEFPRO are presented below to understand well the blistering problematic and to present the main parameters inducing bubbles in the molten glass. Various fused-cast refractories with high zirconia content (HZFC) were studied. Since these materials are very complex, glasses in contact with refractory can blister under specific conditions, depending on each refractory.

The main parameters influencing blistering in fused-cast high zirconia refractories are listed in Figure 14. The huge number of parameters, determined in previous studies, reinforces the complexity of this blistering phenomenon.

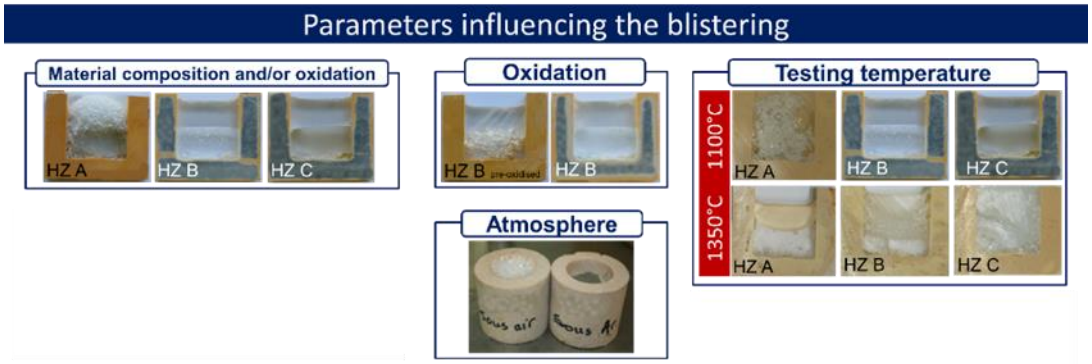

Figure 14: Summary of parameters influencing the blistering phenomenon of molten glass in contact with fused-cast high zirconia refractories (HZFC) [63].

The most relevant parameters are the refractory composition, the atmosphere composition, the oxidation state of the refractory and also the temperature. All these parameters summed up in Figure 14 are detailed in the following section.

I.6.1 Fused-cast refractories

As mentioned before, past studies allow us to identify some critical parameters influencing the blistering phenomenon. In this part, the main parameters involved in the blistering phenomenon are exposed.

Testing Temperature

The most important parameter seems to be the temperature because it considerably influences the appearance of the blistering by impacting the soda-lime-silica glass viscosity, the zirconia structure, the wettability of the refractory by the glass, etc. Indeed, below a certain temperature, the blistering is not observed. The glass/refractory system needs a critical temperature from which the blistering phenomenon is possible. Likewise, from a certain temperature, the blistering phenomenon is susceptible to disappear. This concept of blistering is easily illustrated in the following pictures of Figure 15. The blistering appears after reaching the temperature of 1122°C, Figure 15 (b), in this example and is not observed anymore after 30 hours at 1400°C, Figure 15 (d).

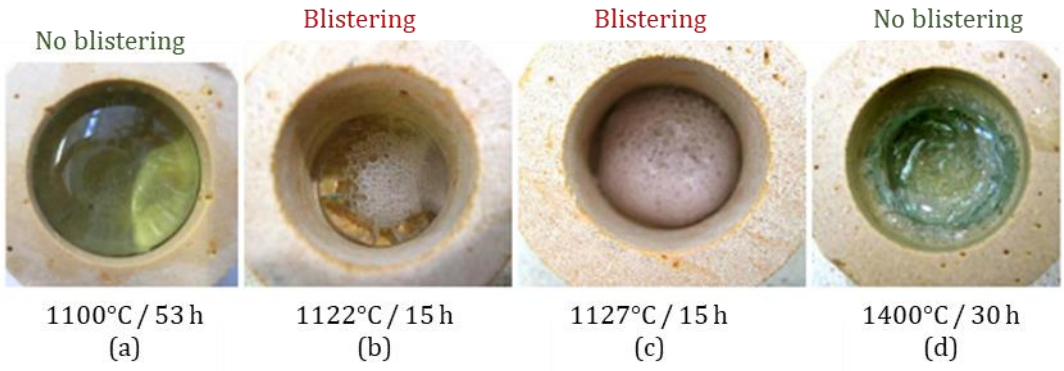

Figure 15: Self-crucible test of HZA with cover glass at different temperatures and testing durations [66].

The temperature has an influence on the blistering, on the interaction between the molten glass and the refractory, but also on the crystallographic structure of the

refractory. A strong blistering phenomenon may be observed with monoclinic phase – at temperatures below the monoclinic/tetragonal phase transformation temperature of zirconia (around 1150°C for HZFC products). However, in the previous studies, it has been observed that with quadratic phase (at 1350°C) a blistering phenomenon can also be present in some glass/refractory systems. Regarding the pictures in Figure 16 and Figure 17, it means that a system can blister at low temperature (1100°C) and not at high temperature (1350°C) like HZA or oxidized HZB, but the contrary is also possible looking at HZB.

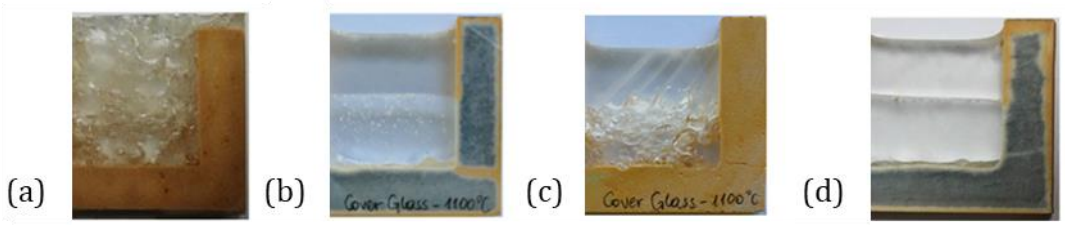

Figure 16: Self-crucible test for fused-cast refractories (a) HZA, (b) HZB, (c) pre-oxidized HZB and (d) HZC at 1100°C in contact with cover glass for 30 hours under air [63].

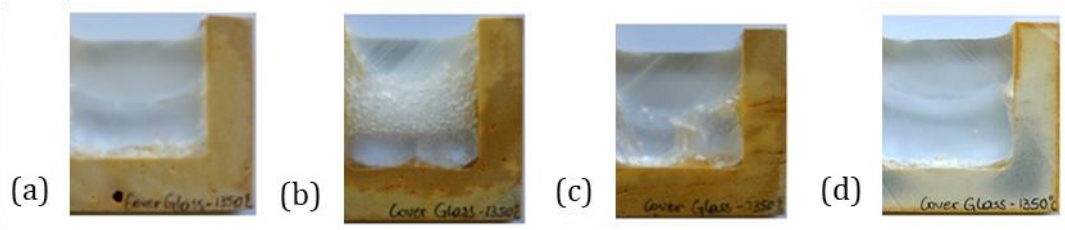

Figure 17: Self-crucible test for fused-cast refractories (a) HZA, (b) HZB, (c) pre-oxidized HZB and (d) HZC at 1350°C in contact with cover glass for 30 hours under air [63].

The tests presented in Figure 16 and Figure 17 show the complex influence of temperature and, eventually, the role of the zirconia phase (monoclinic or tetragonal). It is also possible to observe that the most reactive systems seem the ones with the most oxidized refractory under certain conditions. That is why the oxidation state of the refractory (but also of the glass) should be studied (Figure 18).

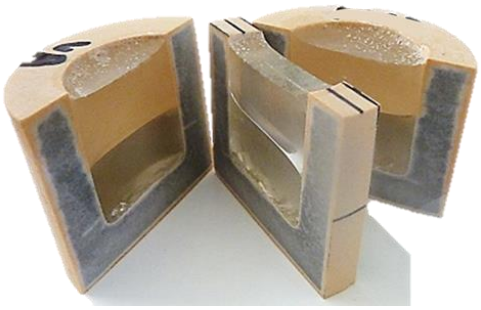

Figure 18: Cutting of a HZC self-crucible for post-mortem study [63].

The zirconia phase transformation (detailed in chapter 2) can be characterized by dilatometry measurement (Figure 19).

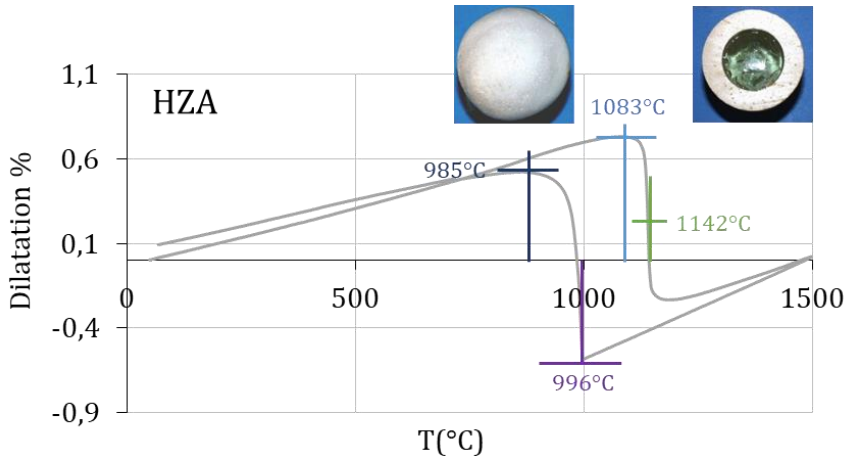

Figure 19: Thermal expansion of HZA as a function of temperature to see the influence of the zirconia phase transformation [66].

Nevertheless, the effect of the temperature is subject of debate. Electrical measurements were previously performed (Figure 20) [67]. An increase of the total conductivity is observed after passing the phase transition at around 1150°C from monoclinic to tetragonal zirconia, without knowing if it is an increase of the ionic or electronic conductivity. Moreover, it should be pointed out that the studied materials are biphasic, with a zirconia and a vitreous phase. The conductivity measurement, using impedance spectroscopy, gives a global information involving both phases, as it will be shown in Chapter 3.

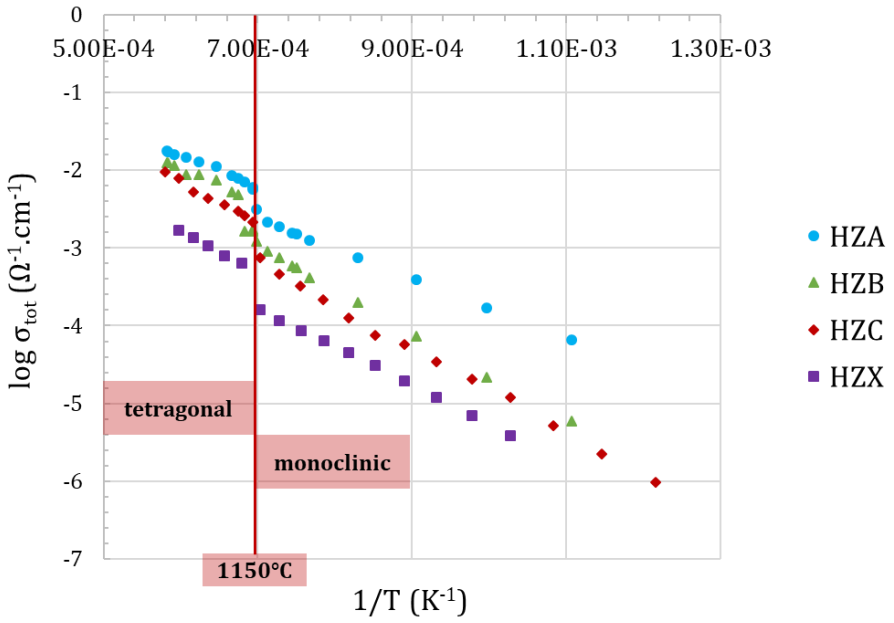

Figure 20: Arrhenius plot of HZA, HZB, HZC and HZX refractories, between 550°C and 1450°C (heating), under air atmosphere, with platinum electrodes [67].

HZA is the most conductive material and it is the refractory containing the highest amount of Na_2O, so its glassy phase is the most conductive one [67]. In comparison, HZB, which has the same amount of glassy phase, is less conductive. The absence of Na_2O, a highly mobile (by Na^+ ions) network modifier, lowers the conductivity. In the same way, HZC has a more viscous vitreous phase than HZB (because it contains more silica) and it is less conductive. The presence of this poor-conductive glassy phase has an impact on the total conductivity measured. In the same way, HZX, which exhibits the lowest conductivity, is the refractory which contains the highest percentage of glassy phase. Zirconia is doped with tantalum, which is blocking oxygen vacancies and so the ionic conductivity. Additionally, its glassy phase does not contain Na_2O but B_2O_3, which makes it also less conductive.

These previous experiments clearly show that the temperature plays an essential role in the blistering. However, due to the complexity of the materials, in our opinion the explanations offered seem sometimes contradictory. It is, moreover, possible that the role of temperature differs according to the composition of the refractory and the experimental conditions. We have, therefore, carried out many conductivity measurements in an attempt to clarify the role of temperature. The corresponding results are presented in chapter 3.

Refractory composition

As mentioned above, the composition of the refractory considerably influences the blistering aptitude. Not only the zirconia content but the whole chemistry of the refractory plays an important role in the interaction with the molten glass. As it is shown in the pictures below (Figure 21), in the same experimental conditions, i.e., 1100°C for 30 hours, intense blistering is observed with HZA. On the contrary, no blistering was observed for HZB and HZC.

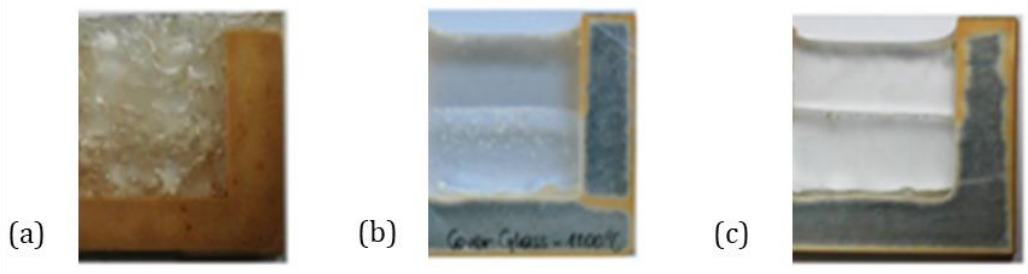

Figure 21: Self-crucible test for (a) HZA, (b) HZB and (c) HZC fused-cast refractories at 1100°C in contact with cover glass for 30 hours at air atmosphere [63].

Refractory redox

The influence of a pretreatment was studied previously [63]. HZB and HZC materials were preheated 24 hours at 1250°C in air. The HZB self-crucible, pre-treated under air, was completely oxidized at the end of the blistering test (30 hours at 1100°C) whereas in raw HZB, oxidation was only observed near cracks. The complete oxidation of the material led to an intense blistering phenomenon (Figure 22 b). On the opposite, only a few bubbles were observed near the cracks of the raw refractory (Figure 22 a).

Figure 22: Self-crucible test for (a) raw HZB and (b) pre-oxidized HZB refractories at 1100°C in contact with cover glass for 30 hours at air atmosphere [63].

HZC pretreated was not completely oxidized, even after 30 hours more at 1100°C and did not blister at all (Figure 23). This difference in oxidation rate could be explained by the lower conductivity of HZC than HZB refractories. These features will be discussed in Chapter 4.

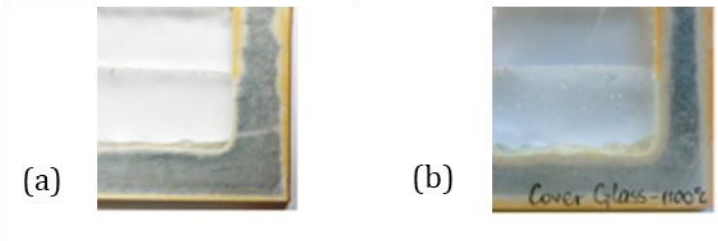

Figure 23: Self-crucible test for (a) raw HZC and (b) pre-oxidized HZC fused-cast refractories at 1100°C in contact with cover glass for 30 hours at air atmosphere [63].

Working atmosphere

Other experiments were performed in order to eliminate the contact of external air atmosphere from the external wall of HZA. To do so, another refractory (HA) has been used to insulate the self-crucible from the air atmosphere (Figure 24).

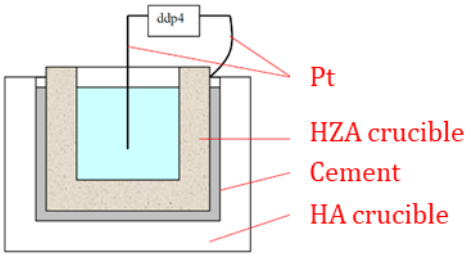

Figure 24: Self-crucible test without external contact with air [64].

This insulation has permitted to reduce considerably the intensity of the blistering phenomenon [64]. The presence of air in contact with external walls of the refractory (referred to as “extrados”) seems to be another important parameter in the blistering scenario. Moreover, by performing the blistering test in inert atmosphere, no blistering is produced (Figure 25).

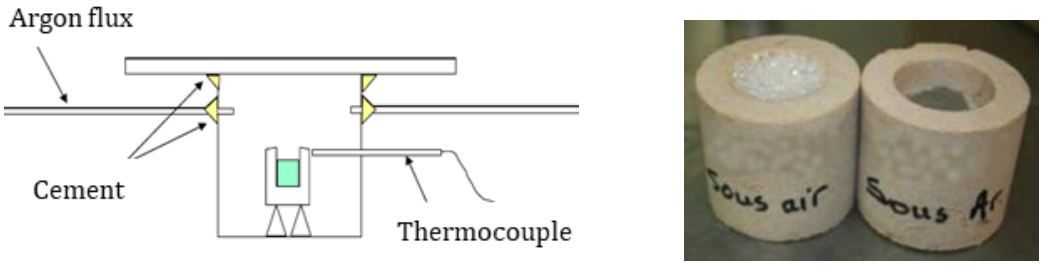

Figure 25: Set-up to control the atmosphere for self-crucible test using HZA/soda-lime glass at 1100°C for 30 hours [64].

Another study performed in the 70s had already demonstrated the influence of the nature of the ambient atmosphere with a setup (Figure 26) very similar to the one used in LEPMI (described later in this manuscript) [65].

The material studied was an AZS refractory. The set-up has been built in an aluminous fused-cast refractory. When the controlled atmosphere was at the extrados of the refractory, the following observations can be made:

- No blistering with argon, nitrogen, carbon dioxide or water vapor
- Intense blistering with air or oxygen

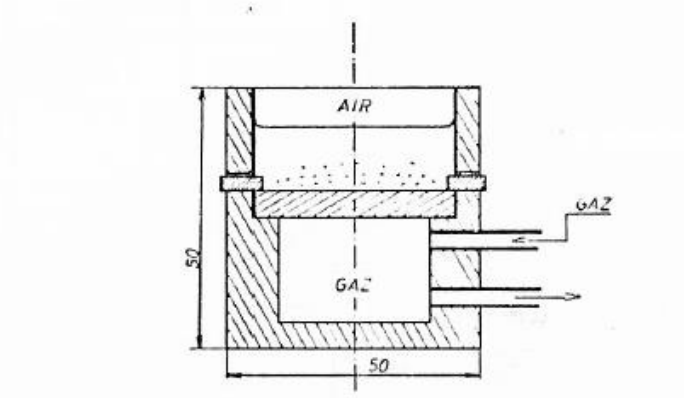

Figure 26: The controlled atmosphere is at the external surface (extrados) of the refractory [65].

When the controlled atmosphere was in contact with glass and the air atmosphere in contact with the refractory, an intense blistering was always occurring (Figure 27).

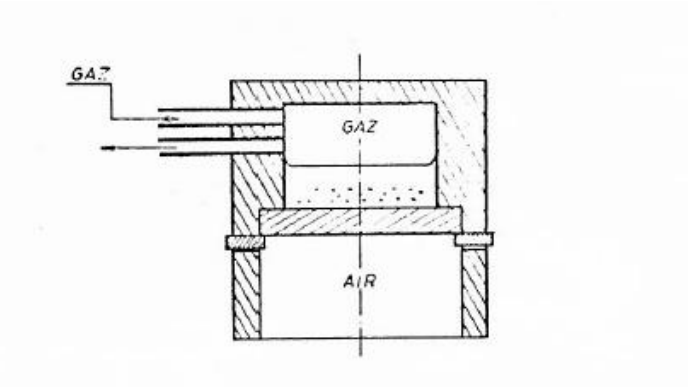

Figure 27: The controlled atmosphere is at the external surface of the glass [65].

This set-up demonstrates that an oxygen partial pressure at the extrados of the refractory is a substantial parameter in the blistering scenario.

I.7 CONCLUSION

As reported is this chapter, the bibliography and intern studies made before starting this project allowed to make preliminary conclusions on the influence of important parameters in the understanding of the blistering phenomenon [63-68]. The main conclusion of our bibliographic research was that the phenomena are complex and that it is necessary to consider many parameters, such as the transport properties within the refractories, their microstructure, the various phases present, their composition, impurities, etc.

From the various tests carried out previously, we proposed either additional measurements (characterization of the electrical transport and of material transport properties of the refractories, XANES analysis, tomographic study), presented in chapter 3, or the design of original devices (set-ups for measuring the electrochemical semipermeability flux, the so-called "sessile drop" method, the coupling of electrochemical analysis of the gas with a mass-spectrometer) which will be presented in chapter 4. Original mechanisms are proposed in chapter 5 to explain the blistering

phenomenon at the interface between glass melts and various refractories, taking into consideration all the experimental phenomena.

Chapter II: **Studied materials and experimental methods**

II.1 MATERIALS OF THE STUDY

The difficulty of this study is found in the diversity of all the materials that can form the refractory/glass couple because a glass furnace is composed by several refractory references. Moreover, the structure of the studied refractories is complex since they are multiphased materials. They contain a crystallized structure surrounded by a glassy phase.

II.1.1 Fused-cast refractories

Historically, the first fused-cast refractories were based on mullite obtained by the fusion of a mixture of silica and alumina. Zirconia was then added to the mixture to improve corrosion resistance, thereby increasing the life of refractories in glass furnaces. Today, fused-cast zirconia refractories manufactured by Saint-Gobain SEFPRO by electro-fusion (fusion temperature between 1800°C and 2500°C) are mainly divided into two families for glass furnaces application:

- Refractories with very high zirconia content (HZFC) with a mass percentage of zirconia higher than 85 wt.% [69], which are the ones studied.

- Alumina-zirconia-silica (AZS) whose composition differs from the first family by the presence of alumina and so less zirconia but more vitreous phase [70].

Zirconia, the main component of fused-cast refractories, can be found in three different crystal forms as shown in the Zr-O phase diagram in Figure 28. It is often a non-stoichiometric compound that has the formula ZrO_{2-x}. At atmospheric pressure, zirconia has 3 allotropic forms:

- α-ZrO_2 with monoclinic structure ($T < 1170°C$). Zirconia is present in nature in the mineralogical form of baddeleyite (monoclinic phase). The stable phase, present

from ambient temperature to 1170°C has an extremely distorted structure of fluorine type CaF_2. In this structure, zirconium atom is linked to seven oxygen.

- β-ZrO_2 of tetragonal structure (1170°C < T < 2350°C). Between 1170°C and 2350°C, zirconia adopts a structure which can be described as a cubic-face-centered lattice derived from fluorine. In this configuration, each zirconium atom is linked to eight oxygen.

- γ-ZrO_2 with cubic structure (T > 2350°C).

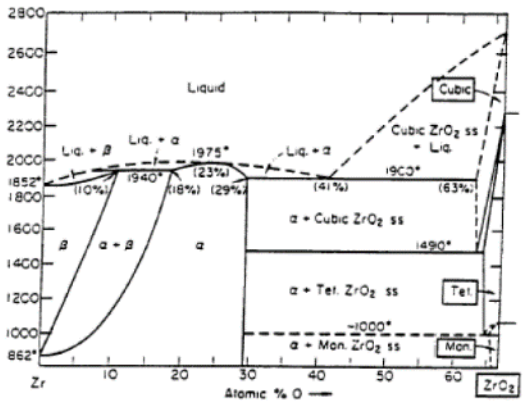

Figure 28: High-temperature phase diagram for Zr-O system [71].

When zirconia temperature increases, it undergoes a first phase transformation switching from the monoclinic phase to the tetragonal phase around 1170°C. The α-ZrO_2 → β-ZrO_2 phase transformation has been studied in the literature. In fact, it takes place in a temperature range from 1000°C to 1200°C, in which the two phases can coexist [72, 73]. The transformation temperature is very affected by the stoichiometry and the purity of ZrO_2 [74]. This transformation of the zirconia lattice is accompanied by a volume contraction of the order of 4%. However, when the temperature goes down, the transformation of zirconia from tetragonal phase to monoclinic phase takes place around 950°C accompanied by a volume expansion also of the order of 4% [75].

This phenomenon therefore follows a hysteresis: the phase transformation is not achieved at the same temperature depending on whether the material is heated up or cooled down (Figure 29). The thermal expansion of a zirconia-based refractory is therefore marked by this hysteresis associated with the martensitic transformation (non-diffusional and athermic) of the zirconia present at a high amount in the

refractory materials studied. It is noticed that the amplitude of this transformation is stronger for HZFC than for AZS, because of its much higher zirconia content (> 80 % compared to an AZS, around 30-40 wt.%). Of course, this phase transition - and the consequent change of properties - as well as the thermal expansion must be considered in the cooling process and during the glass furnace life-cycle.

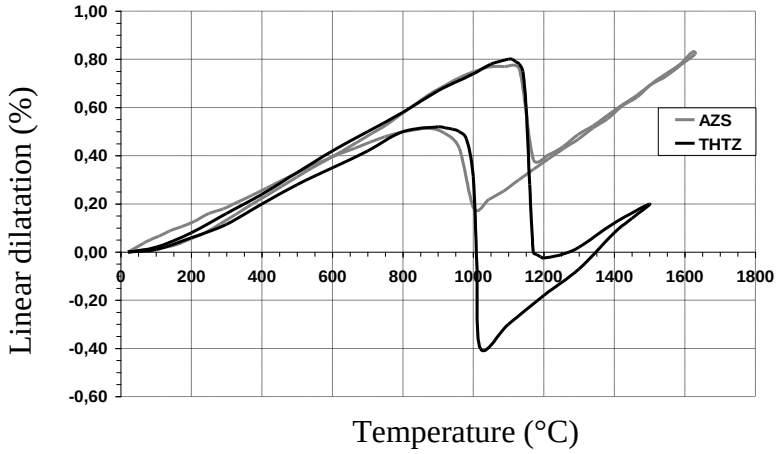

Figure 29: Expansion curve showing the linear dilatation of zirconia based refractories during the heating and the cooling of the material [76].

In the case of fused-cast refractories, the zirconia is not stabilized, but the effects of the phase transformation are reduced thanks to the influence of the glassy phase. In order to improve the corrosion resistance of refractories, the zirconia content was significantly increased in the case of HZFC. The vitreous phase and the crystals are strongly imbricated with a strong three-dimensional percolation. The decrease in viscosity of this intergranular glassy phase promotes the deformation of the material at high temperature, to the detriment of its cracking, thus improving its breaking limit [77]. Indeed, the vitreous phase plays a crucial role in the case of fused-cast refractories, especially during the phase transformation which is accompanied by a volume variation which can create micro cracks. It reduces the effect of stresses caused during this phase transformation which would cause a loss of the entire cohesion in the material if the glassy phase was not there to encompass the volume change of the zirconia matrix. In addition, it should be noted that this vitreous phase recovers the impurities and segregations of minor components which cannot be integrated into the crystallized zirconia grains. The viscosity of the glassy phase was studied using a

synthetic product developed by Saint-Gobain Research Paris. The viscosity of the glassy phase is higher than the one of a conventional soda-lime glass. Its glass transition temperature is close to 780°C against 530°C in the case of a soda-lime glass (Figure 30).

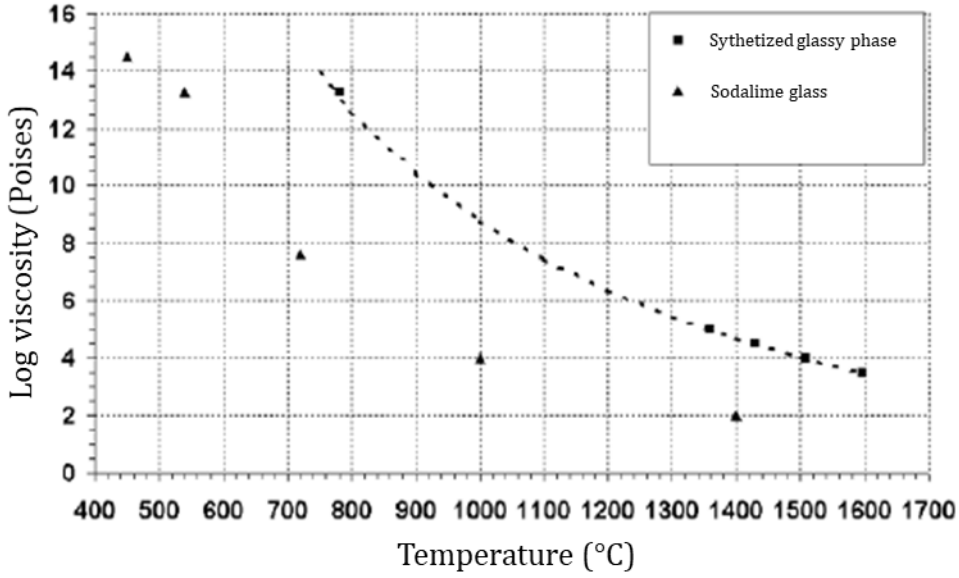

Figure 30: Evolution of the viscosity in function of temperature for soda-lime glass and a synthetized vitreous phase [78].

HZFC are mainly used in furnaces producing specialty or electronic glasses, because of their very good resistance to corrosion, their low ability to create defects (which could be found later in molten glass and so in final product) and their high electrical resistivity. Since these materials are very rich in zirconia (for instance around 94 wt.% and 88 % by volume), their thermomechanical and chemical properties depend on the microstructure of the zirconia phase as well as on the vitreous phase present between the zirconia grains. Figure 31 is a representation of the structure of a two-phase fused-cast material (HZFC family) representing the arrangement between the zirconia grains and the intragranular glassy phase. A very high density is clearly observed thanks to the entanglement of the glassy phase around the crystallized phase. A high degree of compactness allows to reduce the penetration of the glass into the refractory as much as possible and limits the reactive surface. In addition, glassy phase, which is well percolating around the zirconia grains, promotes the deformation of the material at the expense of cracking at high temperatures by glassy phase rearrangement. In particular,

during phase transformation of zirconia associated with a volume expansion of the whole material but also during the manufacturing process.

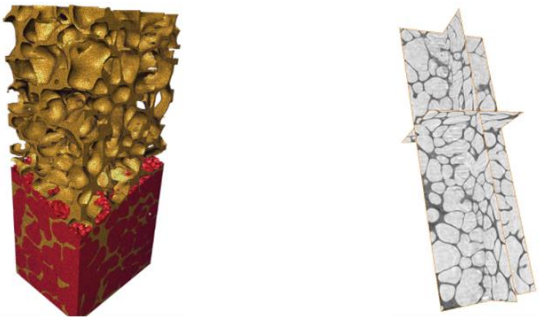

(a) (b)

Figure 31: Bi-phased microstructure of a HZFC, (a) monoclinic zirconia in red and vitreous phase in yellow, (b) zirconia in grey, vitreous phase in black [79].

Once the various steps of the manufacturing process have been carried out to shape the refractory, the refractory block is ready to face the aggressive conditions inside a glass furnace. When the furnace is started, the heat-up is normally the first rise in temperature of the refractories since they are almost kept at constant temperature thereafter (Figure 32). However, the materials are subject to other stresses: large temperature gradients, influence of the expansion of the materials as a function of the different temperatures in the furnace, corrosion by glass or dust, etc. [80].

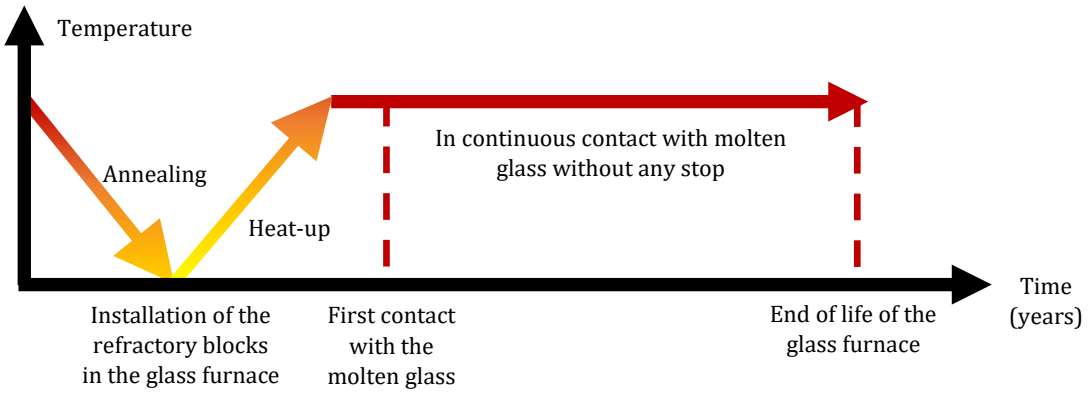

Figure 32: Life-cycle of a refractory block.

AZS refractories are probably the most common type of refractory used in contact with glass for the production of container and flat glass [61, 81]. They are more specifically recommended in tanks and as melting, refining, working area, feeders, throat and weir blocks. HZFC, the main family of material of this study, is recommended to obtain better corrosion resistance mostly necessary in contact with glass ceramic, borosilicate glasses, and other special glasses. HZFC is recommended for tank walls, throat, distribution channels, feeders, and electrode holders.

Several fused-cast references were studied during this project.
Table 4 presents the composition of the high zirconia fused-cast materials (HZFC). All these materials are from the same family, it means similar composition and porosity (around 1-2%).

Table 4: Composition of fused-cast refractories studied (in wt.%).

Reference	ZrO_2	SiO_2	Al_2O_3	Na_2O	B_2O_3	Ta_2O_5	Y_2O_3
HZA	94.1	X	X	X			
HZAB	93.9	X	X	X	X		
HZX5	93.8	X	X		X	X	
HZB	93.8	X	X		X		
HZBC	92.6	X	X	X	X		
F2590-2	91.3	X	X	X			
HZC	90.4	X	X		X		
HZX	88.4	X	X		X	X	
HZSY	88.1	X	X	X	X		X
HZS	86.9	X	X	X	X		X
F2590-3	86.6	X	X	X			
F2603-3	86	X	X	X	X		
F2590-4	83.2	X	X	X			
F2603-1	82	X	X	X	X		
F2590-5	76.7	X	X	X			

II.1.2 Glass of the study

An industrial soda-lime-silica glass was used during this experimental work. The AKM glass contains high amount of alkaline oxides (Na_2O + K_2O ~ 15-22 wt.%), alkali-earth oxides (MgO + CaO > 5 wt.%), and also alumina (Al_2O_3 > 8 wt.%).

II.1.3 Samples preparation

The samples are taken from a refractory block after the sintering or fused-cast process. A core sample is first taken in SGR Provence or SGR North-America and the final shape is machined in LEPMI, Grenoble. Indeed, each experimental set-up needs a specific shape. The size of the samples is described in the dedicated parts. For fused-cast references, two states of the refractories are studied: the raw refractory and the oxidized one. A complete oxidation is obtained after 30 hours at 1350°C for the small samples used in this study. For sintered refractories, raw and heat-treated materials are also studied. In this case the heat treatment is described in each test procedure.

II.2 CHARACTERIZATION OF THE REFRACTORIES

II.2.1 Electrical properties

Principle

The electrical properties of the refractories were characterized by impedance spectroscopy. This technique is often used in the case of ceramics and its advantage is the separation of the dielectric relaxations as well as the blocking phenomena within the material, from the response of the electrodes. While using conventional techniques, the electrode response generates an interference in the interpretations of the properties only related to material. The principle of the technique consists in applying an alternating voltage $U = U_0.exp(j\omega t)$ to the sample positioned between two metallic

electrodes, and measuring the intensity $I = I_0.exp(j\omega t + \Phi)$ (Figure 33). The impedance is the ratio between the applied sinusoidal voltage U over the resulting current I as expressed on equation (9), and the pulsation ω ($\omega = 2\pi f$, with f, the oscillating frequency) and Φ the dephasing [82].

$$Z = \frac{U}{I} = \frac{Uo.\exp(j\omega t)}{Io.\exp(j\omega t+\Phi)} \qquad (9)$$

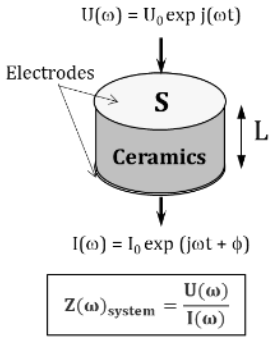

Figure 33: Principe of impedance spectroscopy technique [82].

The electrical impedance is a complex number that can be represented in polar coordinates by its module | Z | and dephasing Φ (Bode plane) or in cartesian coordinates (called the Nyquist plot in electrochemistry). Cartesian coordinates are the most used in our field of application [82]:

$$Z\ (\omega)\ =\ Re\ (Z\ (\omega))\ +\ j\ Im\ (Z\ (\omega)) \qquad (10)$$

- Z is the complex impedance;
- Re(Z) is the real part of the impedance, in other words the resistance;
- Im(Z) is the imaginary part of the impedance, in other words the reactance with the dephasing Φ of the intensity I(t) with respect to the voltage U(t).

The impedance diagrams are theoretically made up of a succession of semicircles more or less off-centered with respect to the real axis (Figure 34). The diagram can be separated into two main parts: one at higher frequencies which corresponds to the electrical properties of the ceramic and another one at lower frequencies which corresponds to the response of the electrodes [83, 84].

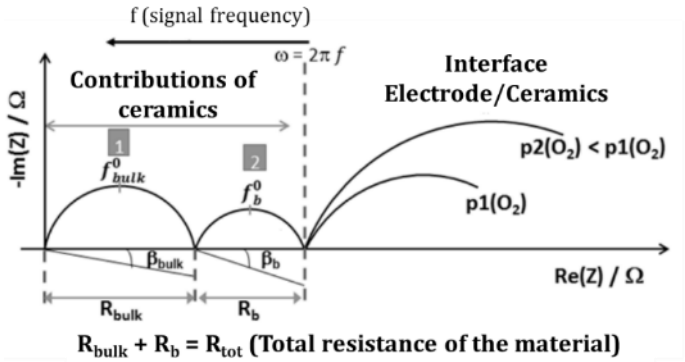

Figure 34: Typical impedance diagram of ceramics. R_b is defined as $R_{blocking}$ in this manuscript [84, 85].

The impedance semicircles can be characterized by a relaxation frequency $f°$, a resistance R, a depression angle β and a capacitance C (also called a capacitive effect when its value is too high to correspond to a conventional physical property, for instance, when it is an electrochemical pseudocapacitance). The semicircles can be also characterized by resistances and constant-phase elements (CPE) [84, 86]. Analysis and interpretation of the impedance diagrams depends on the physico-chemical characteristics of the sample. We can distinguish two main cases: single-phase or dense ceramics and composite or porous materials.

Case of single-phase and dense ceramics

It is admitted that in the case of dense ceramics, the semicircle obtained for high frequencies represents the bulk (grains) while the medium frequency semi-circle corresponds to the microstructure defects (grain boundaries, cracks, or insulating inclusions) [85, 87, 88]. From the high frequency response, we can determine the intrinsic properties of the phase that makes up the grains, such as its electrical conductivity (σ), relaxation frequency ($f°$) and dielectric constant (ε). The conductivity of grains is calculated according to the following relationship:

$$\sigma_{bulk} = \frac{1}{R_{bulk}} \cdot \frac{L}{S} \qquad (11)$$

where R_{bulk} is the resistance determined by the intersection of the bulk semicircle on the real axis of the Nyquist plot, L is the sample thickness and S its surface area. The

relaxation frequency $f°_{bulk}$ (in Hz) is determined at the top of the semicircle in Nyquist plot. The dielectric constant ε of the material can be determined from the capacitance which is calculated according to the relaxation equation of a semi-circle:

$$2\pi\, R_{bulk}\, C_{bulk}\, f°_{bulk} = 1 \text{ or } R_{bulk}\, C_{bulk}\, \omega° = 1 \qquad (12)$$

Concerning the medium frequency semicircle, we can obtain information on the blocking effects on the internal surface of the material linked to the presence of grain boundaries or cracks (conductivity and capacitance). The apparent conductivity of grains boundaries can be calculated from equation (11) by replacing R_{bulk} by $R_{blocking}$, determined by the intersection of the blocking semicircle on the real axis of the Nyquist plot (Figure 34).

Case of composite or porous materials (conductive phase + insulating phase)

In the case of heterogeneous materials, the semi-circle of the bulk corresponds to the overall electrical properties of the conductive matrix modified by the presence of a second phase [84, 89, 90]. In this case, R_{bulk} and $f°_{bulk}$ depend on the volume fraction and on the morphology (tortuosity) of the conductive phase. The dielectric constant ε calculated from C_{bulk} is a combination of the dielectric constant of the conductive and insulating phases. The medium frequency semicircle is an electrical response linked to the presence of the insulating phase. This blocking effect depends on the contact between the conductive and insulating grains. *It should be emphasized that in the case of a two-phases material we cannot extract the intrinsic electrical properties of two phases from the impedance diagrams.*

In both cases, the total resistance (R_{tot}) of the sample corresponds to the resistance of the bulk summed to the resistance associated with the blocking effect (Figure 34). The conductivity of the material can be calculated according to the following relationship:

$$\sigma_T = \frac{1}{R_{tot}} \cdot \frac{L}{S} \qquad (13)$$

Set-up

Conductivity measurements were carried out up to 1500°C. The sample holder, in alumina, is surrounded by an alumina tube limiting convection effects and stabilizing the temperature. It can hold 3 samples, allowing simultaneous measurements in the same conditions (Figure 35 and Figure 36). Moreover, the atmosphere around the samples was controlled to study the influence of several pO_2 on the conductivity of the refractory. Symmetric cells were studied: electrode material (platinum) | refractory | electrode material (platinum). Data acquisition was carried out by a 1260 Solartron frequency analyser, an impedancemeter measuring impedance modules between 10^7 and 0,01 Hz. The impedance measurements were sometimes made with another impedancemeter (Hewlett Packard HP 4192A) over the 1.3 x 10^7 Hz to 5 frequency range.

The geometric factor k of the sample is defined by the ratio of the thickness of the sample L (in cm) and its surface area S (in cm^2). All measurements must be normalized by the geometric factor $k = L/S$ so that they are comparable to each other. To obtain good accuracy on the geometric factor, it is advisable to use symmetrical electrodes and so cylindrical samples. The standard size of the samples used is a cylinder of 8 mm of diameter and 6 mm of thickness. The electrode material is thus deposited on the two bases of the sample.

The electrode material used is platinum. A platinum paste is deposited on the two surfaces and then dried at 100°C. The organic binder contained in the platinum paste was then removed during an annealing for 2 hours at 1000°C under air atmosphere. The platinum paste was deposited twice until a resistivity of less than 1 Ω on the two metallic surfaces was obtained.

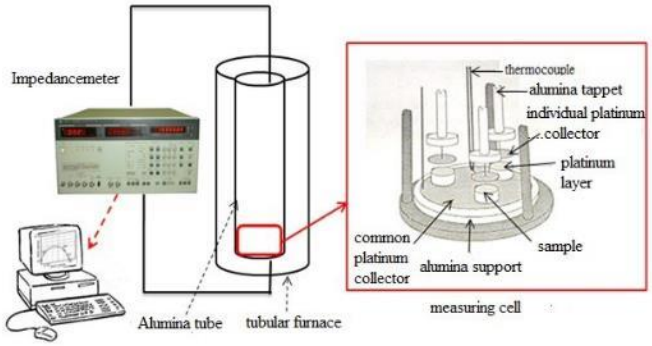

Figure 35: Impedance Spectroscopy set-up used in LEPMI [91].

Figure 36: Sample holder of the conductivity set-up.

II.2.2 Electrochemical semipermeability

Principle

When a mixed ionic electronic conductor (MIEC) material is exposed to an oxygen partial pressure gradient (rich oxygen pressure on one side and lean oxygen pressure on its other side), a phenomenon of semipermeability (oxygen electrochemical permeability) may occur. Oxygen is transported in the form of O^{2-} ions and an electronic flux in the opposite direction must be present to maintain the charge neutrality [92-96].

The redox half-reaction on the oxygen rich side is:

$$\frac{1}{2}\,O_2 + 2e^- \rightarrow O^{2-} \quad (14)$$

and the reverse half-reaction governing the interface of the oxygen lean side is [97]:

$$O^{2-} \rightarrow \frac{1}{2} O_2 + 2e^- \quad (15)$$

inducing an oxygen flux across the material from the oxygen-rich to the oxygen-lean side, as schematized in Figure 37.

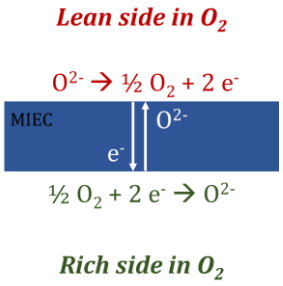

Figure 37: Oxygen flux through mixed ionic and electronic conductor [98].

More information on the permeation process will be given in Chapter 3.

Electrochemical semipermeability of oxygen without glass contact

In order to have the capacity to measure a semipermeability flux, a three-atmosphere set-up has been used for years in LEPMI, and was improved to reach higher temperatures (up to 1500°C) [67, 97, 99].

With the three-atmosphere set-up, it is possible to quantify the permeability of a refractory pellet with a diameter of 19 mm and variable thicknesses. However, the sample has to be thick enough so the physical permeability does not exceed the semipermeability flux. The pellet is placed between two alumina tubes and the sealing is made with platinum O-rings (Figure 38). As gold has a temperature of fusion of 1064°C, it is only possible to use it as a seal below 1000°C. As platinum has a fusion temperature of 1768°C, it is possible to use it in furnaces reaching 1500°C.

Even if seals enhance the airtightness, the sample between the alumina tubes is surrounded by an argon flux to avoid the presence of air contamination in the upper chamber containing the argon flux, analysed by the oxygen sensor.

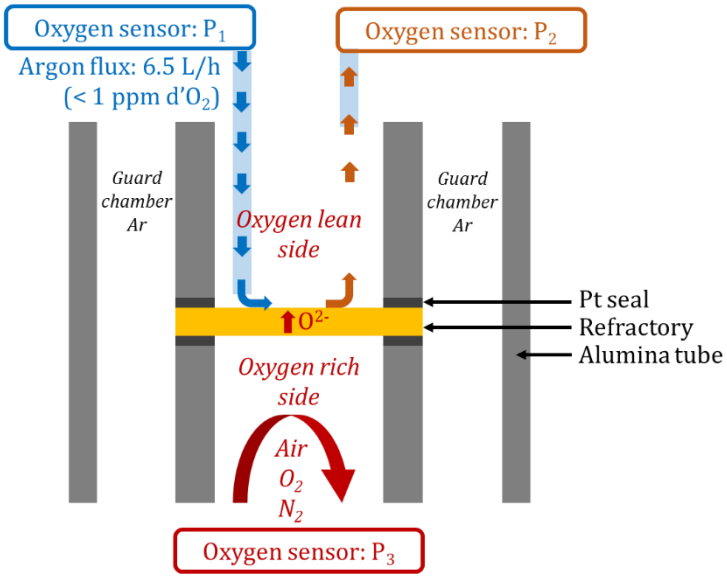

Figure 38: Semipermeability set-up used in LEPMI: three atmosphere set-up.

The oxygen pressure upstream the cell (as shown in Figure 38 as P_1 and P_3) is controlled and monitored by flowmeters, electrochemical pumps and oxygen sensors (see Appendix A). The oxygen pressure downstream the cell P_2 is also controlled by an oxygen sensor [97].

It is possible to measure the variations of the after-passing partial pressure P_2-P_1 through the cell, i.e., the oxygen that penetrated into the oxygen lean side through the refractory material, with a very high precision. These highly sensitive sensors (Oxygen sensor 1 and Oxygen sensor 2) measure the oxygen pressure in the argon flow according to the Nernst law, expressed in equation (16) [97, 100, 101]:

$$E = \frac{RT}{4F} \ln\left(\frac{P_2}{pO_2(air)}\right) \qquad (16)$$

- E: e.m.f of the sensor (V)
- F: Faraday constant (= 96 485 $C.mol^{-1}$)
- T: temperature (K)
- R: Universal gas constant (= 8.314 $J.mol^{-1}.K^{-1}$)
- pO_2 (air): reference oxygen partial pressure (here air: 0.2 bar))
- P_2: measured oxygen partial pressure

Electrochemical semipermeability of oxygen with glass contact

In order to characterize the blistering phenomenon, an improvement of the existing set-up was made with F. Fournet-Fayard to be able to study the influence of the glass/refractory contact on the semipermeability phenomenon. The pellet was replaced by a small self-crucible able to contain glass, creating a new interface between the glass and the refractory to be studied. The following drawing Figure 39 shows the self-crucible in yellow.

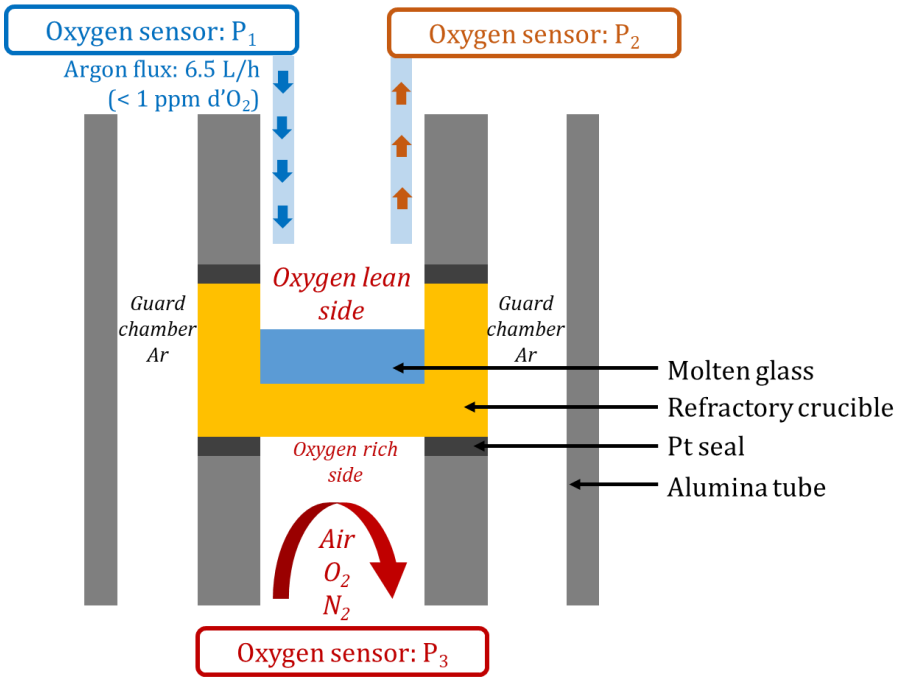

Figure 39: Improvement of the semipermeability set-up to study the influence of the glass in contact with the refractory at high temperature.

In the studies presented below, the self-crucible has always the same dimensions (Figure 40) and contains always the same amount of glass (approximately 5 mm thick for 1.5 g).

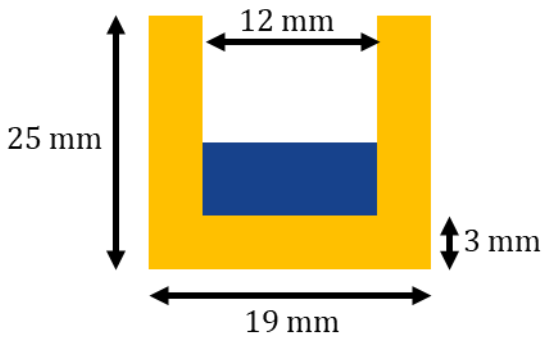

Figure 40: Dimensions of the self-crucible containing the glass, for the three-atmosphere set-up.

In some experiments a mass spectrometer was added, downstream the permeation set-up, after the oxygen sensor, to analyse, in addition to oxygen, all the components of the gas, especially nitrogen, sulfur oxides, carbon oxides, etc.

Experimental procedure and data treatment

The self-crucible is put in the set-up with the solid glass in it. The glass used was initially pre-melted to avoid blistering linked to glass reactions. All the samples went through the following heat treatment (Figure 41) to have comparable measurement. Indeed, the thermal history of the material has to be considered in the interpretation since it influences the blistering. As the atmosphere containing O_2 is influencing the results, the heating ramp is performed under argon atmosphere in the whole set-up until reaching the testing temperature (Figure 41).

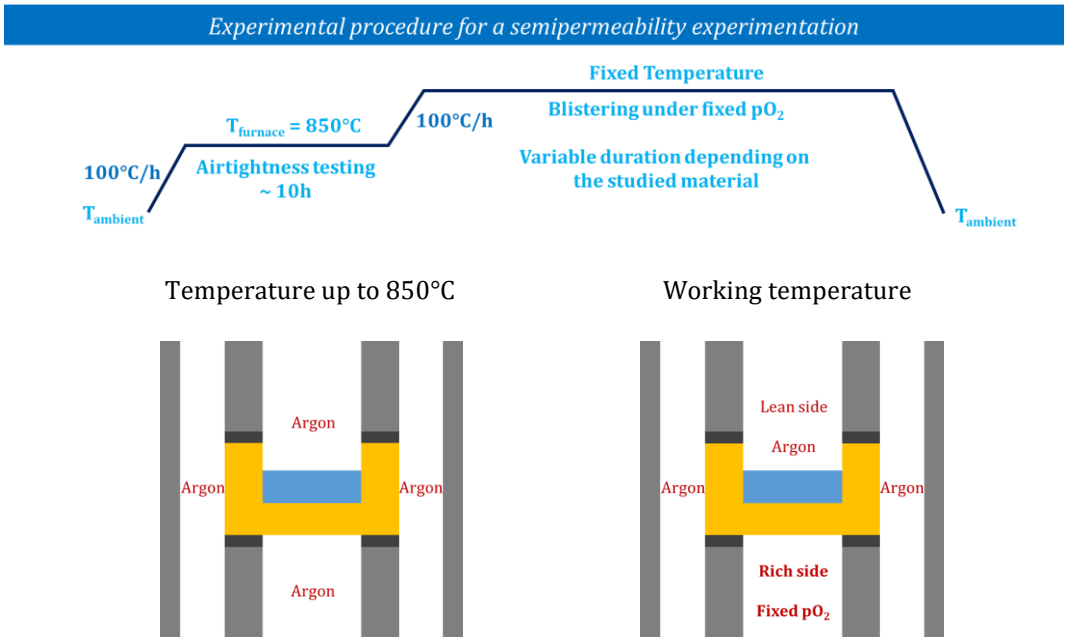

Figure 41: Temperature cycle of a self-crucible containing glass into the three-atmosphere set-up to study the semipermeation phenomenon.

In this configuration, an oxygen flux is measured at 1100°C under pO_2 = 0.2 bar at the rich side. When bubbles burst in flowing argon, an oxygen peak is recorded by the oxygen gauge (Figure 42).

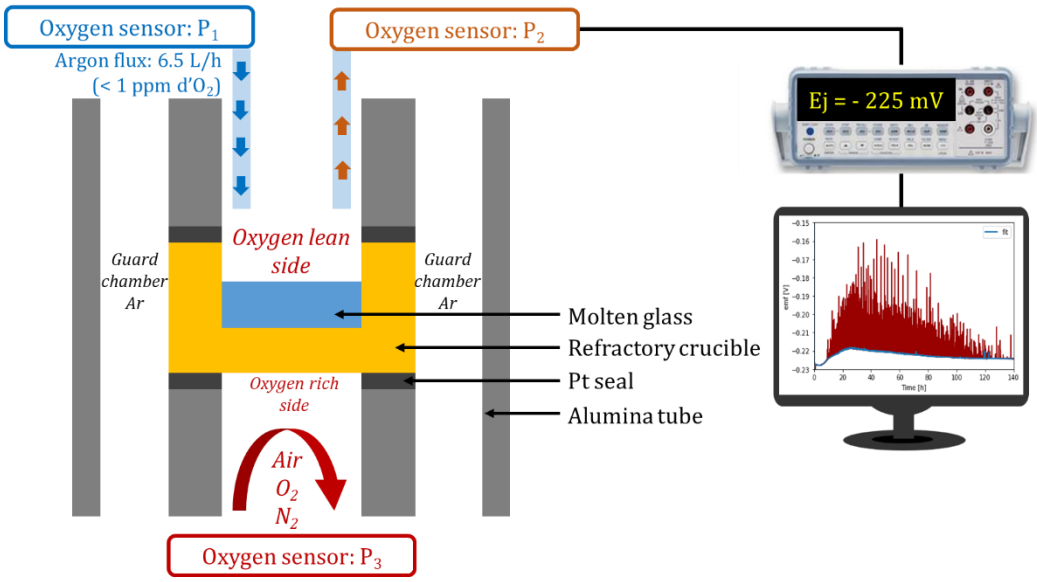

Figure 42: Improved semipermeability set-up to characterize the blistering phenomenon as functions of temperature, time and partial pressure of oxygen.

The raw measurement is directly taken from the oxygen sensor. Raw data are expressed as a voltage in function of time. As a measurement is taken each second and the experiment lasts for several days, a huge amount of data has to be treated. For this reason, a Python code was developed to transform the raw measurement into an oxygen flux as a function of time, in order to study the beginning of the blistering and the blistering duration (Figure 43). To do so, the Nernst equation (17) was used. Indeed, as the raw data are given as a voltage in function of time (Figure 43 (a)), by using the following equations we can change the sensor emf into an oxygen mole fraction per second (19) and then into an oxygen flux per hour (20 and 21):

$$E = \frac{R\,T}{4\,F} \ln\left(\frac{P_2}{pO_{2\,(air)}}\right) \qquad (17)$$

$$P_2 = pO_{2\,(air)} \times \exp\left(\frac{4\,F\,E}{R\,T}\right) \text{ (bar)} \qquad (18)$$

Considering the same total pressure in both side of the zirconia wall:

$$x_2 = xO_{2\,(air)} \times \exp\left(\frac{4\,F\,E}{R\,T}\right) \text{ (bar)} \qquad (19)$$

$$V_{O_2} = x_2 \times Argon\ flux \ (mm^3/s) \qquad (20)$$

With argon flow rate = 6 L/h (Figure 43 (b)):

$$V_{O_2} = x_2 \times \frac{6 \times 10^6}{3600} \ (mm^3/s) \qquad (21)$$

Figure 43 (b) shows the variation of the oxygen volume obtained with the equation (21) as a function of time. To facilitate the comparison of different parameters on the oxygen volume, the data were integrated over one hour time (Figure 43 (c)) according to equation: $V'_{O_2} = \int_{t_1}^{t_2} V_{O_2}\, dt$ with $t_2 - t_1 = 1$ hour.

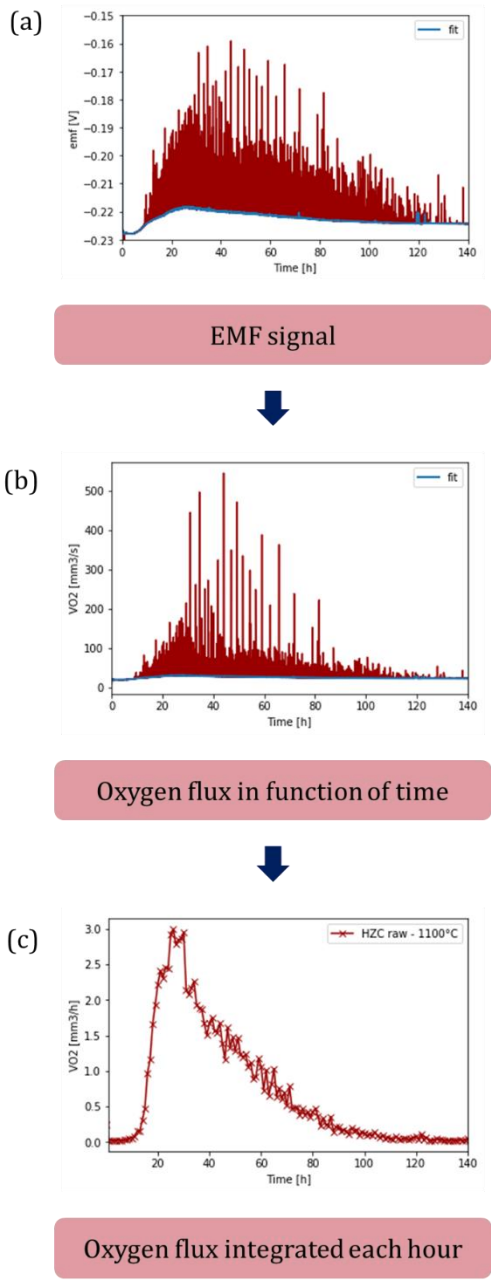

Figure 43: Steps of the data treatment leading to the interpretation of the results (a) emf as a function of time, (b) oxygen flux per second and (c) oxygen flux integrated on each hour.

The baseline is always lower than 10 ppm, showing the good airtightness of the set-up. Apart from that, the measurement can be given with a precision of 1 ppm. By using the oxygen flux, results are easier to interpret. The higher the peak, the bigger the bubble (or several bubbles exploding at the same time). By integrating the curves, it is possible to calculate the blistering dispersion in order to determine the beginning, the end and the blistering peak.

II.2.3 XANES analysis

X-ray Absorption Near Edge Structure part

XANES is a characterization technique measuring the X-Ray absorption of a material close to its absorption edge (+/- 50 eV on each side of the absorption edge). The absorption edge corresponds to the excitation of an electron from core level towards the unoccupied electronic levels by absorption of a photon. A peak is observed because of the sudden increase in the absorption coefficient due to the movement of a core-level electron to an unoccupied orbital or unbound state. The absorption edge is often much more complex than simply an abrupt increase in absorption. Indeed, XANES observation includes:

- the edge position (a primary indicator of the oxidation state of the element),
- the presence and the shape of small features just before the main edge ("pre-edge" features),
- the intensity, the number, the position and the shape of peaks at the top of the main edge.

Before the edge, the intensity of pre-edge features is greatly affected by weak transitions of the coordination geometry of the central atom (Figure 44). At the edge, formal oxidation state may be qualitatively assigned as the energy of the edge position. However, it is not an invariant quantity for a given element, but rather shifts in accordance with electron density. Finally, coordination shells are interrogated just beyond the edge as the emitted photoelectron scatters off neighbouring atoms [102].

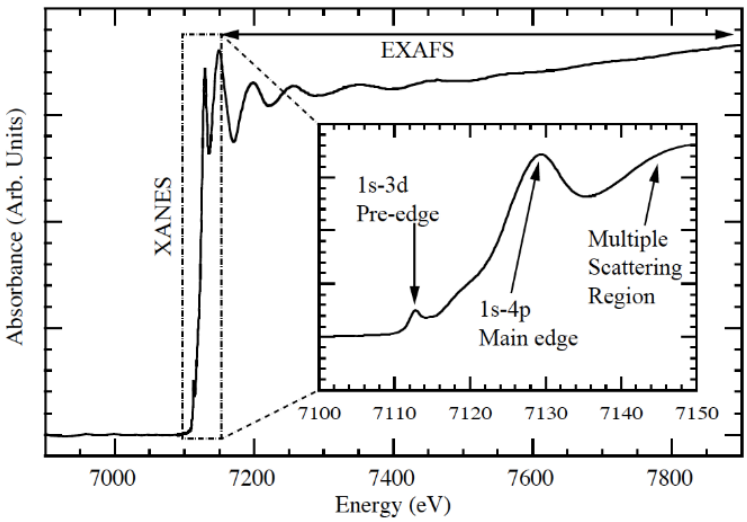

Figure 44: XAS example at Fe K-edge. XANES region of the spectrum with prominent features are named. The initial oscillations after the edge arise from multiple-scattering processes and are not typically included in EXAFS analysis [103].

The X-ray absorption spectrum can be measured in two ways. The most direct measurement of the absorption is performed in transmission mode. To do so, the sample is illuminated with X-rays and the incident and transmitted photon intensities are recorded. After that, the ratio between the incident and transmitted photon intensity is related to the absorbance of the sample. However, transmission measurements require samples thin enough so that the incident beam is not fully absorbed by the sample. For thicker samples (much thicker than the X-ray absorption length at the energy of the edge of interest), the absorption may be measured by monitoring the fluorescence that accompanies the X-ray absorption process (Figure 45).

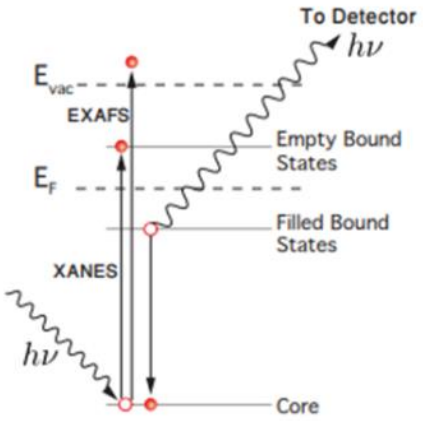

Figure 45: Physical description of absorption edge processes in Partial Fluorescence Yield schema [103].

An energy-discriminating detector is then used to separate the X-ray emission of the element of interest from the X-ray background of the other elements in the sample. This measure is called Partial Fluorescence Yield (PFY). It reduces efficiently the XAS background because only the fluorescence of the element of interest is contributing to the signal, thanks to the detector used. The detector is typically oriented perpendicular to the incident beam polarization to selectively distinguish background radiation from signal of interest [103].

Redox state in refractories measured by XANES

The oxidation state of refractory is an important parameter which plays a role in the blistering phenomenon of refractories in contact with glass. Oxidation state specifically refers to the redox of the low quantities of iron and/or titanium which are present as impurities mostly in the vitreous phase of the fused-cast materials. The concentration of iron is in the range of 0-1 wt.% for HZFC. In 2016, J. Gillot [104] has initiated XANES measurements with Synchrotron radiation on refractories and demonstrated that it was possible to get a fine insight of the iron oxidation state.

As the oxidation-state of the absorption site increases, the absorption edge energy increases correspondingly. Moreover, XANES is a direct measurement of valence state since each element has its own edge energy (Figure 46). An element's valence can be measured even in a heterogeneous sample, which is the case for our samples [105].

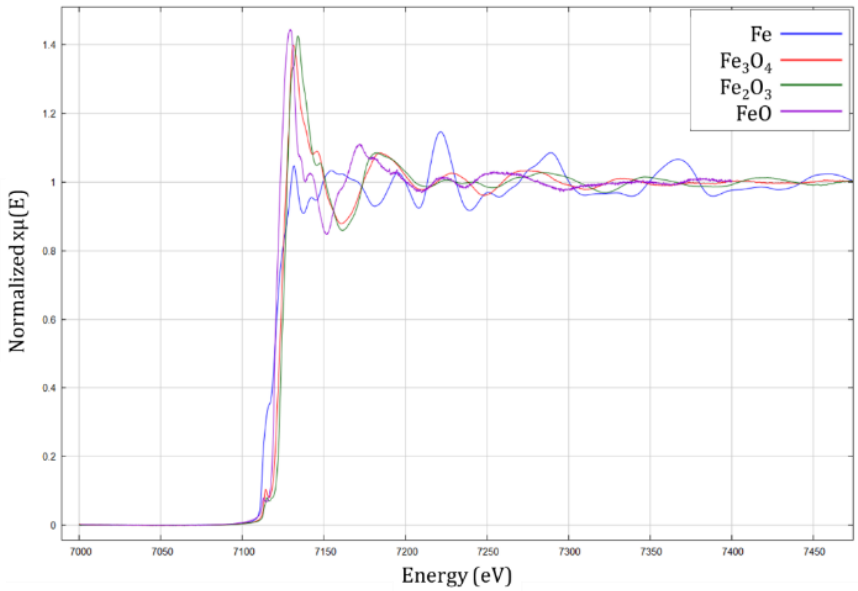

Figure 46: Shift of the edge position to higher energy as the valence increases [106].

It was shown that the electro-fused AZS and HZFC refractories have a redox ratio R = (Fe(II)/Fe(II)+Fe(III)) between 0.63 and 0.85, which is much higher than that of a soda-lime glass for glazing (R = 0.18). This analysis also highlighted the fact that some metallic iron could be present in raw refractories.

New measurements were made in 2018 using Synchrotron X-ray absorption spectroscopy at the European Synchrotron Radiation Facility (ESRF) in Grenoble - beamline BM30B, performing a systematic study of the iron and titanium oxidation states on refractories which have been subjected to controlled heat-treatments in which temperature, atmosphere and duration were varied. These heat-treatments mimicked the conditions encountered during a self-crucible test (proof test for the blistering susceptibility). XANES measurements were performed over many samples: more than 30 different samples were characterized (Figure 47). A novel analysis approach was also used in order to have, as an output, the ratio of $Fe/FeO/Fe_2O_3$ species present in the materials.

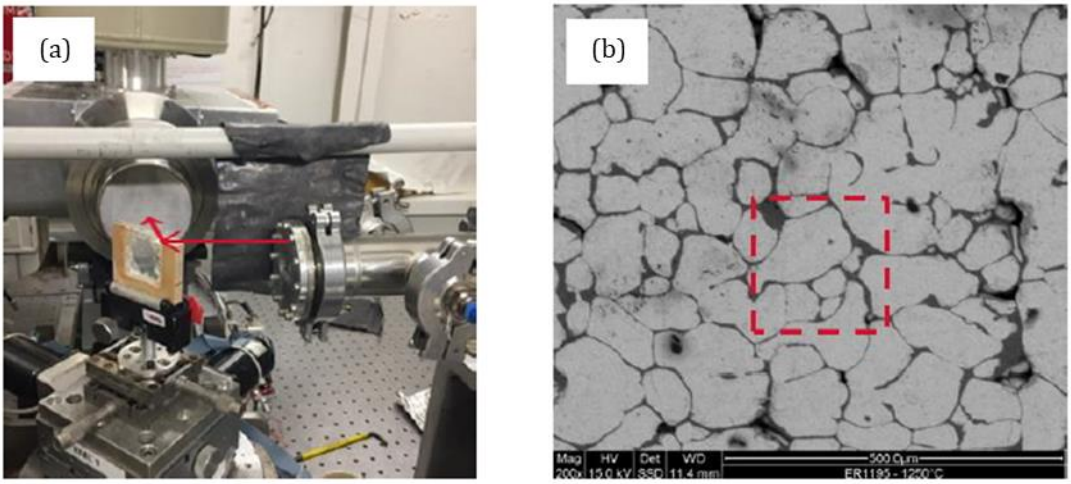

Figure 47: (a) Set-up for XANES measurement at the ESRF, Grenoble,
(b) Analysis spot: 200 x 200 µm^2 area.

Tests were performed ex-situ at ambient temperature in fluorescence mode. The measurements were performed at the Fe K$^-$ (7112 eV) and the Ti K$^-$ (4966 eV) edges. The analysis spot was a 200 x 200 µm^2 area, it means that it encompasses vitreous phase zones as well as ZrO_2 grains (Figure 47). The signal measured here is therefore an averaged value over a large area. Moreover, the impurity content in ZrO_2 grains is lower than in the vitreous phase as shown in Table 5.

Table 5: Microprobe measurements of Fe_2O_3 (in wt.%) in glassy phase and zirconia grain.

Measure	**1**	**2**	**3**	**4**	**5**	**6**	**7**	**8**	**9**
Glassy phase	0.6	0.6	0.6	0.5	0.5	0.6	0.6	0.5	0.6
ZrO_2 grain	0.04	0.03	-	-	-	0.04	-	0.04	0.04

Therefore, we can guarantee that the measured XANES signal at the Ti and Fe edges is coming mostly from the vitreous phase. In order to consider that metallic iron might also be present in these materials, we chose in this study the "linear combination fitting" tool available in the software ATHENA. J. Durst performed a fit of the entire XANES pattern (including the pre-peak, from 7100 to 7160 eV) and by using a set of 12 different references provided by ESRF [107, 108]. These references are ranked from metallic iron to Fe^{3+} based compounds, and were recorded on pure minerals at this ERSF beamline.

Other XANES measurements were performed during the 2019 and 2020 shifts at the SOLEIL synchrotron on the Samba beamline at Fe and Zr edges. Modelling was also done with ATHENA software by S. Brossard [109]. The goal of the measurements done at the Fe edge was to measure the oxidation state of iron depending on the nature of the refractory and the applied heat treatment. For measurements performed at the Fe K edge, spectra were acquired from 7 000 eV to 7 400 eV every 0.2 eV. The pre-peak absorption transition at the Fe K edge was analysed and used to estimate the fraction of Fe^{2+} and Fe^{3+} as well as the coordination of iron (4-fold to 6-fold). The analysis was based on the work published by Wilke et al. [110], but finds its limit when metallic Fe is present in the sample.

II.2.4 Microstructural characterization

X-Ray Diffraction

X-ray diffraction (XRD) characterizations were carried out on the diffractometer PANalytical X'PERT Pro MPD in Consortium des Moyens Technologiques Communs (CMTC of Grenoble-INP) by T. Encinas, with the following parameters:

- Measurement: reflexion mode (Bragg-Brentano geometry)
- Anode: Copper
- Wavelength (Cu K_α): 0.15419 nm

Scanning Electron Microscopy

The microstructure of the refractory materials was observed by Scanning Electron Microscopy (SEM) images realized with the SEM FEG JEOL IT500HR LV with EDS (energy dispersive spectroscopy, an energy-selective X-ray microanalysis system) in Consortium des Moyens Technologiques Communs (CMTC of Grenoble-INP).

X-Ray Tomography

Geometric percolation provides information about the phase connectivity. A 2D description of the microstructure does not allow a satisfactory estimation of the percolation rates of the refractories, especially for fused cast products. The SEM images are therefore not sufficient to obtain this information. A 3D description obtained with X-ray absorption tomography is needed. X-ray absorption tomography is a non-destructive imaging technique allowing the volume reconstruction of a 3-dimensional object from a series of sectional image measurements. The principle is based on a multidirectional analysis of the interaction of a X-ray beam with the studied matter, by recording the radiation transmitted after crossing the sample. "Cross-section" images of the three-dimensional sample are then mathematically reconstructed in grey levels, expressing the local attenuation coefficient of the incident beam, voxel by voxel. X-ray tomography therefore provides access to the core material to analyze the variations in absorption and the differences in composition. It makes possible to locate any heterogeneity, singularity, void or inclusion present in an object [111]. Samples from 2 mm and 1 mm in diameter were characterized with the EASYTOM XL Nanofoyer by S. Coindeau and P. Lhuissier in SIMAP, Grenoble. The measurements were respectively performed with 2 µm and 1 µm voxel size.

Geometric percolation is a concept of morphology [112] used to reconstruct the related parts of a phase in a heterogeneous environment [113, 114]. A phase X is connected if, at any pair of points x_1 and x_2 belonging to X, at least one path connecting them can be found. The percolation rate (T_p) of a phase X can be defined as the ratio of the measurement of the percolated phase and the measurement of the starting phase:

$$T_p = \frac{Mes(X_p)}{Mes(X)} \qquad (22)$$

A phase is percolating if a marker on one edge of the image reaches the other edge of the image. To calculate the percolation rate of a 3D image (made up of several layers of 2D images), the calculation is performed on an increasing number of layers. Percolation naturally increases with the number of layers. When the percolation rate reaches 100 %, all the X markers find a path to reach the other edge of the image and that every point of the sample is connected to all the edges of the picture. The percolation rate can be related to the volume fraction of the material: the higher the

volume fraction, the easier for a marker to find its way within the structure, therefore the more percolating.

Chapter III: **Electrical characterization and transport properties**

III.1 IMPEDANCE DIAGRAMS

First of all, it should be pointed out that this work was performed on heterogeneous materials. The samples are derived from industrial materials and the composition of the same reference can change from one sample to another. Especially for fused-cast refractories because of non-isotherm cooling, solidification interval or phase density differences in the blocks (see Appendix B). That being said, the resistivity results, measured on three different samples of the same reference, showed an overall dispersion of less than 10%. The electrical properties of the materials were characterized by impedance spectroscopy and the first step of the analysis was the separation of the material response from the electrode response.

Platinum was used as electrode material since the measurements were carried out at high temperatures (see Chapter 2). However, in order to help the separation between the sample electrical response and the electrode response, some characterizations were performed with silver as electrode material (on raw materials) because the electrode reactions depend on the electrode material. In fact, for ionic conductors (O^{2-} vacancies conductors) or eventually mixed ionic/electronic conductors, the global electrochemical electrode reaction (23) occurs at both ceramic/metal interfaces and can be influenced by the nature of the electrode material (Pt or Ag for example). The electrode reaction can also be modified by the partial pressure of oxygen, near to the interface, according to the following equation:

$$1/2\, O_2 + 2e^- + V_O^{\bullet\bullet} \leftrightarrow O_O^{\times} \qquad (23)$$

where O_2 is the oxygen in the gas at the interface, e^- the electrons from the metal and $V_O^{\bullet\bullet}$ the charge carrier in the ceramic electrolyte.

Two series of measurements were made, at the same temperature and atmosphere (air at pO_2 = 0.2 bar). The first one was done with silver electrode (silver paste). Then, the same samples were cleaned before applying platinum paste. Figure 48 compares the

impedance diagrams obtained with Ag and Pt electrode material for different refractories. We can observe that the low frequency part of the diagram (10^2 Hz < f < 10^{-2} Hz) was modified by changing the electrode material. Thus, this part of the diagram characterizes the electrode reaction. In addition, the estimated capacitance values for the response in this low frequency region are close to 10^{-6} F. This capacitance value is characteristic of the electrode reaction [115], indicating that the low frequency regions of the impedance diagrams are the response of the ceramic/electrode interface. It means that only the high frequency response is characteristic of the studied material. Thanks to this method, the total resistance (R_{tot}) of the sample can be identified and separated from the electrode response (Figure 48).

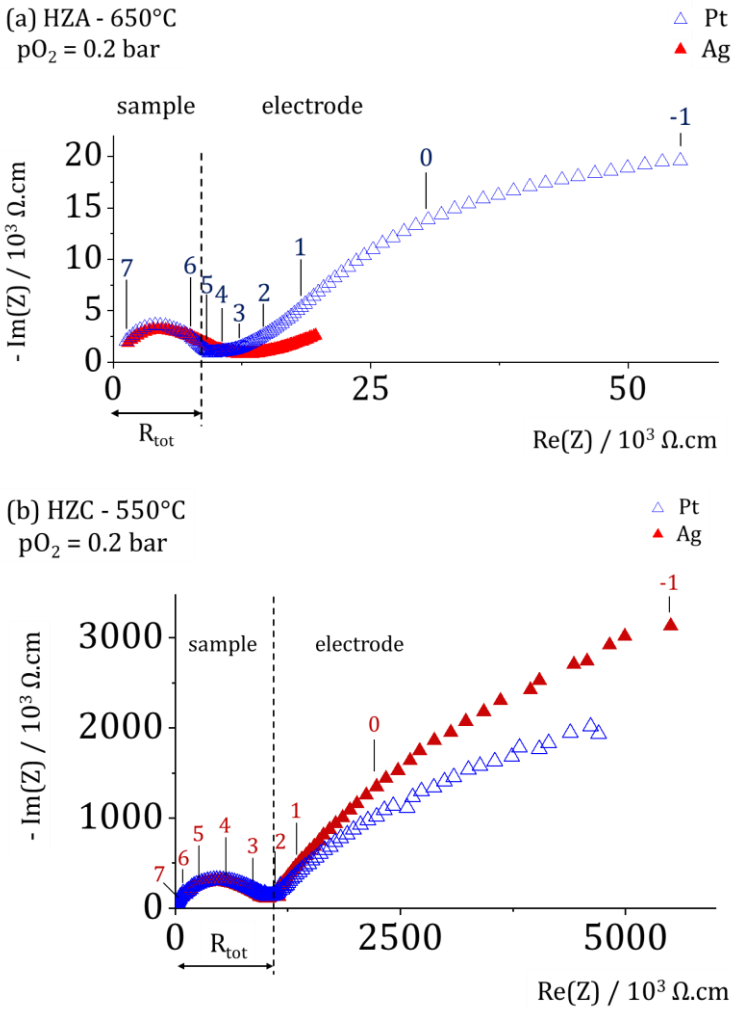

Figure 48: Normalized impedance diagrams samples with silver or platinum as electrode material under air atmosphere (pO_2 = 0.2 bar): (a) HZA at 650 °C and (b) HZC at 550°C. R_{tot} is determined with an error of 5%. (The numbers 1, 2, etc. indicate the logarithms of the measuring frequencies in Hz).

Figure 49 shows the evolution of the impedance diagrams as a function of the measuring temperature obtained for two reference materials (HZA and HZC). An evolution of the shape of the impedance diagrams with a shift towards the high frequencies of the observed responses can be observed when temperature increases. For HZA at 850°C, the overall sample response is observed at frequencies higher than 5×10^4 Hz (and define $R_{tot} = 2.1\times10^3$ Ω.cm), the global electrode response is observed at frequencies below 10^4 Hz (Figure 49 (a)). At 1200°C, the high frequency region of the diagram is completely modified by the self (inductive effects) of the set-up. In this case, the frequencies above 5×10^5 Hz characterize the sample response (R_{tot} = 180 Ω.cm) and frequencies below 10^5 Hz the electrode response (Figure 49 (e)). The same behaviour is observed for HZC, with $R_{tot} = 1.1\times10^4$ Ω.cm. at 850°C (Figure 49 (b)) and R_{tot} = 400 Ω.cm at 1200 °C (Figure 49 (f)).

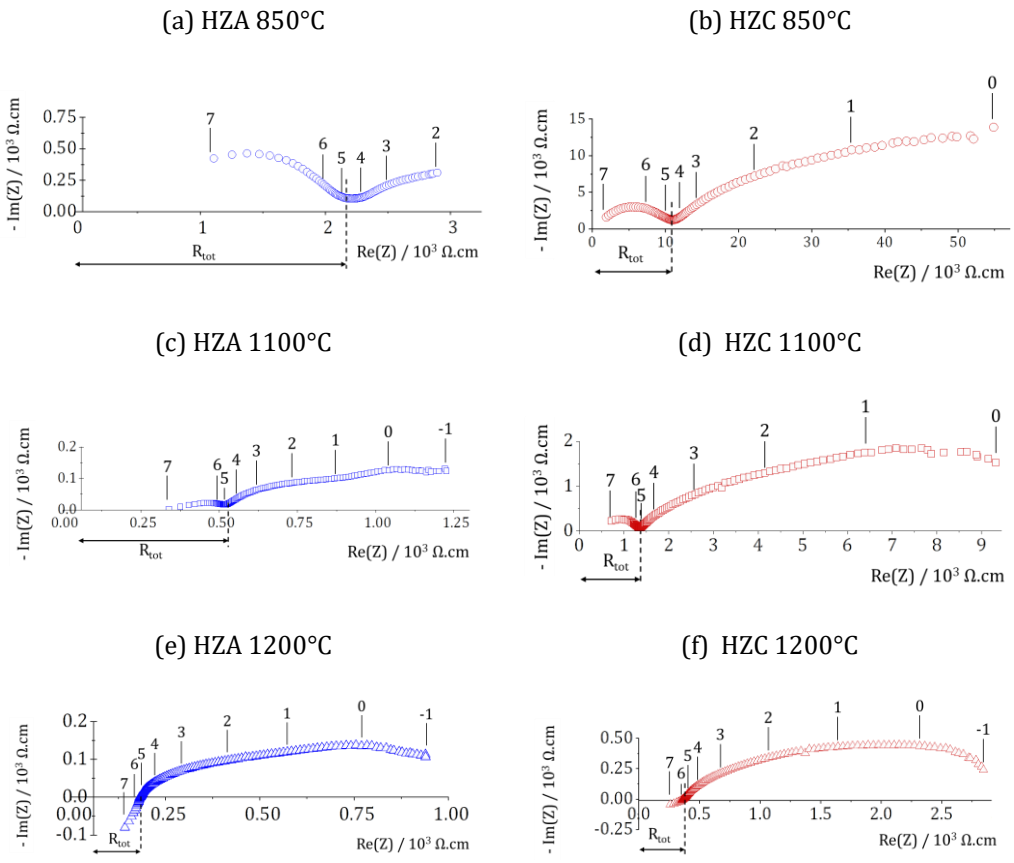

Figure 49: Normalized impedance diagrams of HZA and HZC with platinum electrode material, under air atmosphere (pO_2 = 0.2 bar) at (a) HZA 850 °C, (b) HZC 850°C, (c) HZA 1100°C, (d) HZC 1100°C, (e) HZA 1200°C and (f) HZC 1200°C. R_{tot} is estimated with an error of 5%. (The numbers 1, 2, etc. indicate the logarithms of the measuring frequencies in Hz).

It is important to note that the overall response of the high-temperature electrode is in agreement with the Schouler's diagram (Figure 50) [116]. This diagram shows the evolution of the specific frequency of each contribution (f^0) as a function of temperature. It is constructed from the experimental observations that each contribution is formed by one or more arcs of circle. For each semi-circle, the equation of relaxation is noted as: $R\ C\ 2\ \pi\ f^0 = 1$.

Each phenomenon is characterized by a capacitance (C) that does not depend on the temperature. For all processes, the resistance (R) decreases with temperature and the relaxation frequency f^0 is thermally activated. If we deduce the value of f^0 from the diagram, we can see that at 1200°C the contributions of the electrode $f^{0)t}$ and $f^{0)e}$, can be observed at frequencies of up to 10^5 Hz which corresponds to the ones observed in Figure 49 (e) and Figure 49 (f). It has to be noticed that in previous study, the low frequency part was considered as characteristic of the vitreous phase [117], which is not confirmed by our results.

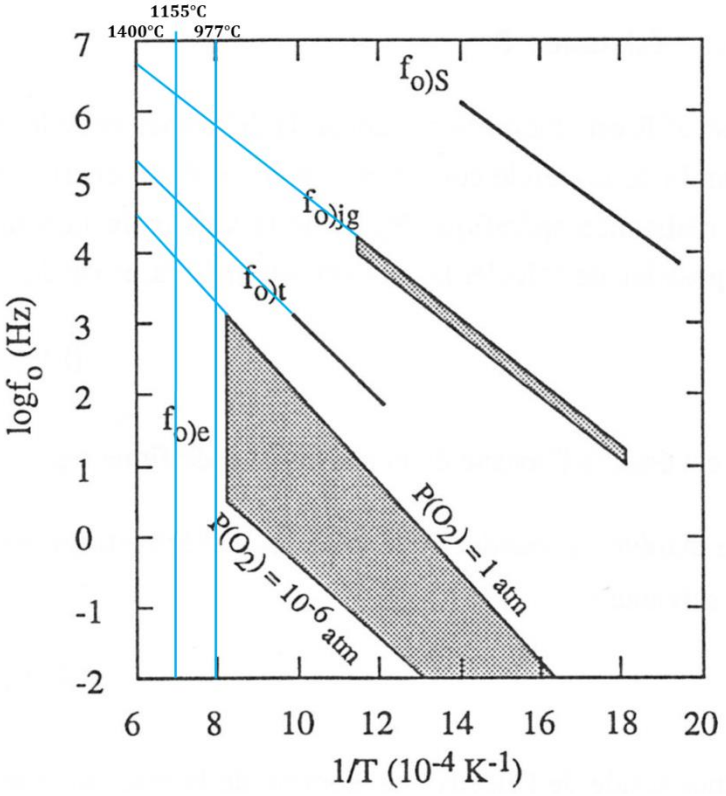

Figure 50: Schouler's diagram for YSZ [116].

For the presentation of the impedance diagrams only the ones obtained with platinum as electrode material are presented in the following sections and the electrode response is partially suppressed in the Nyquist diagrams to make the comparisons easier.

Figure 51 shows impedance diagrams of samples of different HZFC refractories references measured at 850°C. For all samples, the separation between material and electrode response is clearly identified and the total sample resistance can be determined. The shape of the high frequency region of the diagram is similar for all samples and its amplitude and frequency distribution is composition-dependent. HZS material doped with Y_2O_3 (Figure 51 (a)), is the less resistive one with $R_{tot} = 2.6\times10^3$ Ω.cm. The sample response is observed between 10^7 and 10^5 Hz. HZB and HZX references show their sample response between 10^7 and 10^4 Hz. HZB is the reference material without dopant Figure 51 (b) and $R_{tot} = 1.3\times10^4$ Ω.cm. HZX doped with Ta_2O_5 Figure 51 (c) is the most resistive with $R_{tot} = 5\times10^4$ Ω.cm.

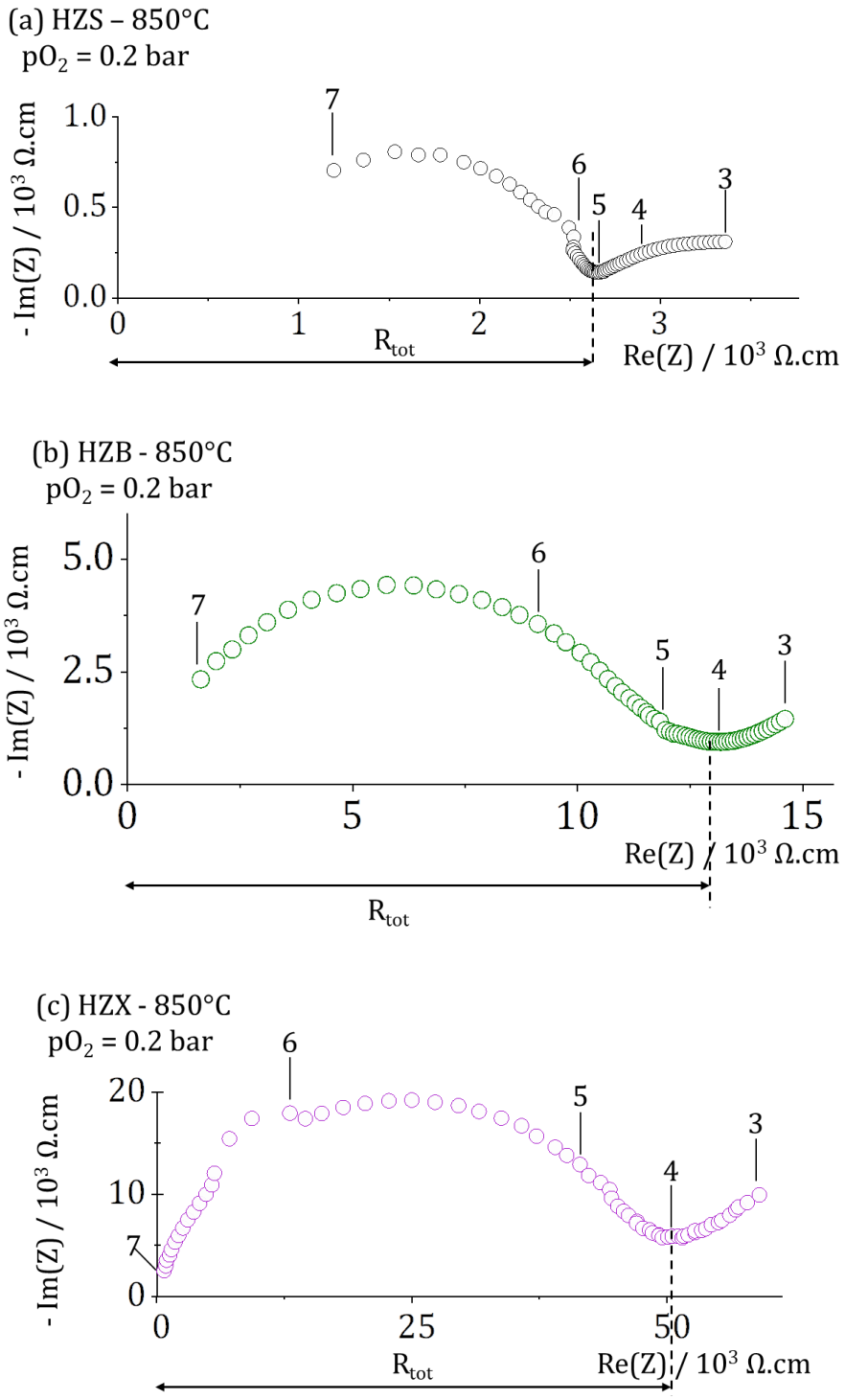

Figure 51: Normalized impedance diagrams of (a) HZX and (b) HZS with platinum electrode material, under air atmosphere (pO_2 = 0.2 bar) at 850°C. R_{tot} is estimated with an error of 5%. (The numbers 1, 2, etc. indicate the logarithms of the measuring frequencies in Hz).

To identify the different components of the sample response (bulk and blocking effects), an analysis of the impedance diagrams was performed at sufficiently low temperatures to ensure that the diagrams were complete and not distorted by setup

effects. The impedance diagrams were resolved with the Z-view software (Scribner Associates Incorporated), by fitting the data using an equivalent electrical circuit consisting of two or three R//CPE elements in series, respectively attributed to the bulk, the blocking contribution and the electrodes response (Figure 59). CPE is a constant phase element with an impedance Z_{CPE} defined as [118]:

$$Z_{CPE} = \frac{1}{Q(j\omega)^n} \qquad (24)$$

where Q is the pseudo-capacitance, ω the angular frequency and n the CPE exponent. This impedance was used to represent the non-ideal behaviour of an RC circuit. The capacitance (C(F)) of each contribution were calculated from the CPE parameters and the resistance R using the following expression [119]:

$$C = (Q\,R^{1-n})^{1/n} \qquad (25)$$

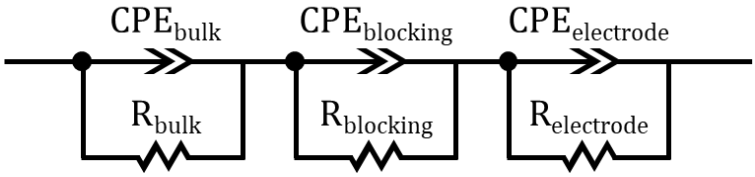

Figure 52: Equivalent circuit used to resolve the impedance diagrams.

The impedance spectra of HZC sample recorded at 600°C and 700°C with the respective fitting results are given in Figure 53. The spectra are composed of three depressed semicircles. The high frequency one, called "bulk semicircle", is the characteristic response of the matrix. In the case of homogenous and dense ceramics, it is quasi-identical to that of a single crystal of the same composition and the medium frequency semicircle (blocking) describes the grain boundary contribution. However, in our case of heterogeneous materials constituted by zirconia grains and vitreous phase, the high frequency contribution corresponds to the electrical response of the matrix (zirconia) modified by the presence of the second phase. The medium frequency semicircle could be related to the zirconia/vitreous phase interface, zirconia/zirconia grains contacts and to other microstructure defects properties (blocking effects). In addition, the low frequency semicircle corresponds to the electrode response. The separation of the sample response into two contributions, bulk and blocking, were easy at low temperature (Figure 53 (a)). However, for diagrams

obtained at 700°C (Figure 53 (b)) or higher, the blocking semicircle became small, and separating both contributions became rather difficult, or even impossible.

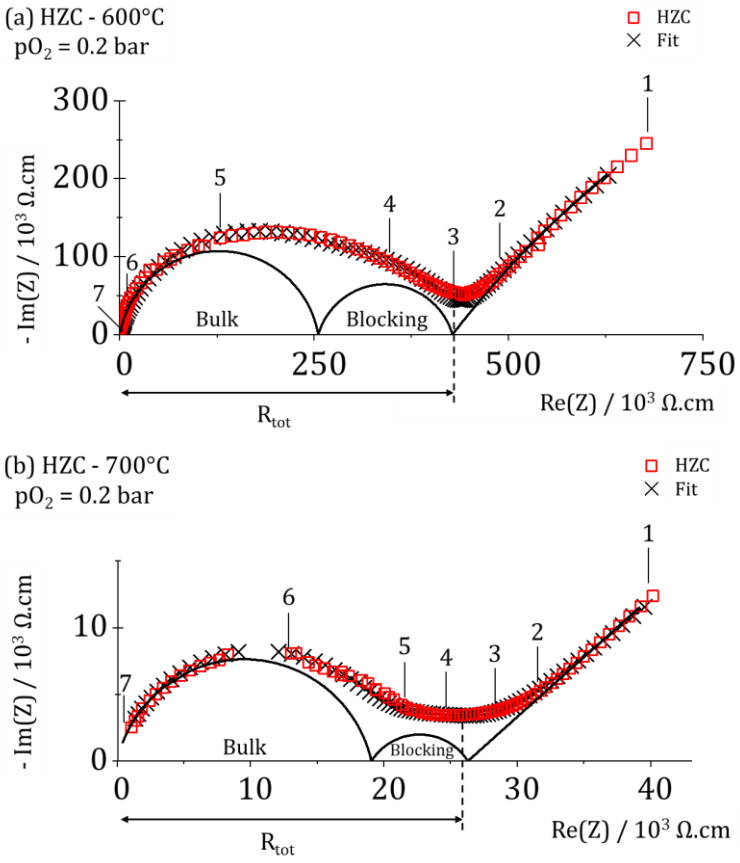

Figure 53: Impedance diagram of HZC sample measured at 600°C (a) and 700 °C (b). The logarithms of the measuring frequencies are indicated by numerals. Bulk and Blocking represent the low and medium frequency electrical responses, respectively. The fitting result with the equivalent circuit with (R//CPE) elements in series is shown as a solid black line.

The resistance, capacitance and relaxation frequency (f^0) calculated from fitting the impedance data are reported in Table 6. This table gives the bulk and blocking contributions, represented by the bulk semicircle and the blocking semicircle, respectively. The normalized capacitances C_{bulk} close to $4x10^{-12}$ $F.cm^{-1}$ and $C_{blocking}$ between 10^{-9} and 10^{-10} $F.cm^{-1}$ are in agreement with the values obtained for the electrical response, respectively of the bulk materials and of the blocking phenomena [115]. The values of f^0_{Bulk} and $f^0_{blocking}$ are thermally activated as indicated on the Figure 50.

Table 6: Impedance parameters obtained for HZC sample at two temperatures.

Temperature (°C)	Bulk semicircle			Blocking semicircle			α_R (%)
	R_{Bulk} ($10^3\Omega$.cm)	C_{Bulk} (10^{-12}F.cm^{-1})	f^0_{Bulk} (Hz)	$R_{blocking}$ ($10^3\Omega$.cm)	$C_{blocking}$ (10^{-10}F.cm^{-1})	$f^0_{blocking}$ (Hz)	
600	255	4.4	$1.4x10^5$	172	0.77	$1.2x10^4$	40,3
700	19	4.0	$2.1x10^6$	7.2	4.1	$5.3x10^5$	27,7

In solid ionic conductors, a fraction of mobile charge carriers can be blocked at internal interfaces [88]. This phenomenon is described as a blocking process at the internal interface and it depends on the microstructure defects and on the conductive phase/isolating interfaces. For our materials, the internal blocking interfaces may be the zirconia/zirconia grains contact or the zirconia/vitreous phase contact. It must be pointed out that in this case, the semicircle observed at medium frequencies (blocking) does not characterize the electrical response related to the movement of charge carriers through the vitreous phase but the effect of the presence of this phase. This phenomenon can be characterized by an adimensional parameter called the "blocking factor, α_R". This parameter is defined as the ratio of the blocking resistance $R_{blocking}$ to the total resistance R_{tot} [88, 90]:

$$\alpha_R = \frac{R_{blocking}}{R_{bulk}+R_{blocking}} \quad (26)$$

The value of α_R decreases when temperature increases (Table 6). This behaviour is in agreement with systematic measurements made on porous zirconia and YSZ/Alumina composites over broad temperature ranges [87, 88]. Generally, two temperature domains have to be distinguished. In the low temperature domain, this parameter α_R is fairly constant.

In the case of composite materials, models based on the effective medium theory (EMT) were used to describe the electrical properties [120]. EMT is a consistent modelling approach that uses the intrinsic electrical property of each phase to calculate the electrical properties of a composite [89]. One of the oldest and most popular EMTs is the Maxwell–Garnett model, which is used to calculate the effective conductivity of a mixture of two phases [121]. The Maxwell–Garnett model derives an expression for the effective conductivity of spherical particle inclusions of conductivity σ^i, embedded

in a matrix of conductivity σ^m, where the interactions between particles are neglected. The Maxwell–Garnett approach is only valid for diluted composite media, whereas the Bruggeman approximation has broader applicability [122, 123]. The Bruggeman approximation equation can be expressed as:

$$v^m \frac{\sigma^m - \sigma^{ef}}{\sigma^m + 2\sigma^{ef}} + v^i \frac{\sigma^i - \sigma^{ef}}{\sigma^i + 2\sigma^{ef}} = 0 \qquad (27)$$

where σ^{ef} is the effective conductivity of the composite, v^m is the volume fraction of the matrix and v^i is the volume fraction of the inclusions (second phase).

In this case, the bulk response result from a combination of the electrical properties of the two phases contained in the material. Steil et al. [89] have demonstrated that the existence of blocking semicircles cannot be explained by these theories. Comparisons of the theoretical predictions to the corresponding experimental diagrams of YSZ/Al_2O_3 composites have clearly shown that these theories correctly predict the observed variations of the bulk semicircle (which in this case is highly variable with the alumina content) and that the blocking semicircle is an additional feature specific to rather low conductivity materials (Figure 61) [84, 90, 124].

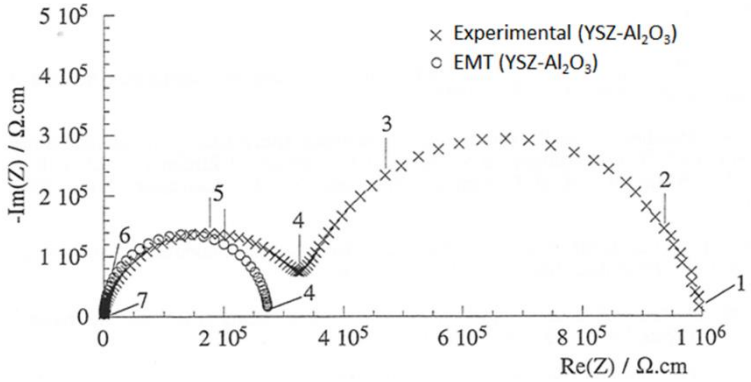

Figure 54: Comparison between the experimental diagram of an YSZ/ Al_2O_3 composite (30 vol.% of alumina) and the corresponding diagram deduced from (EMT) with σ^m, = 10^{-6} S.cm^{-1}, σ^i = 6×10^{-10} S.cm^{-1} and v^i = 0.3 [89].

It is interesting to compare HZA (Figure 55 (a)) and HZB (Figure 55 (b)) because they contain the same ZrO_2 mass fraction (94 wt.%). However, HZA contains 6 wt.% of vitreous phase VPh_A and HZB contains 6 wt.% of vitreous phase VPh_B. For both cases, the part of the diagram corresponding to the sample consists of two semicircles. The

sample total impedance is higher for HZB than for HZA. Table 7 presents the impedance parameters calculated for these two samples. The contribution of the HZB bulk is almost 10 times greater than for HZA (Figure 62). On the other hand, the relaxation frequency of the bulk response (f^0_{Bulk}) of HZB is 10 times lower than that for HZA. From the bulk semicircle relaxation equation (12), this behavior leads to a similar capacitance values for both materials (Table 7). It is due to the fact that the capacitance of the composite is the result of a combination of the dielectric constants of each phase composing the material. As both materials contain 94 wt.% zirconia, the dielectric properties will be mainly fixed by the zirconia phase. As both samples contain the same fraction of zirconia phase (therefore the same matrix conductivity), the difference in conductivity of the composite can only be related to the difference in conductivity between VPh_A and VPh_B. Moreover, the vitreous phase VPh_A must be more electrically conductive than VPh_B. In fact, HZA is composed of a vitreous phase containing Na_2O and HZB is composed of a vitreous phase containing B_2O_3 (without Na_2O). The difference observed on the impedance diagrams can be attributed to the fact that the Na_2O-containing glassy phase is more conductive than the B_2O_3-containing glassy phase [117]. In order to support this hypothesis, a new material (F2590-5) with a lower zirconia content (76 wt.%) and 24 wt.% of vitreous phase (VPh_A) was manufactured.

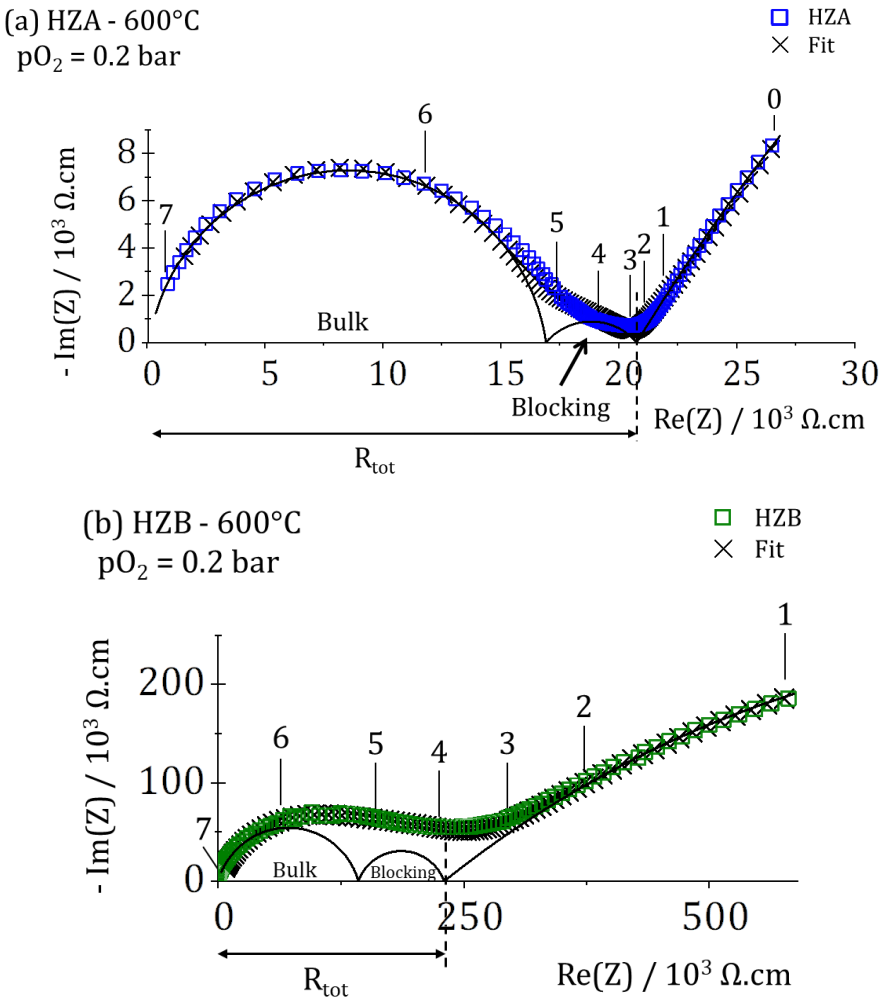

Figure 55: Impedance diagram at 600°C of two materials: (a) HZA and (b) HZB. The logarithms of the measuring frequencies are indicated by numerals. Bulk and Blocking represent the low and medium frequency electrical responses, respectively. The fitting result with the equivalent circuit with (R//CPE) elements in series is shown as a solid black line.

Table 7: Impedance parameters obtained for HZA and HZB samples at 600°C.

Sample (600 °C)	**Bulk semicircle**			**Blocking semicircle**			α_R **(%)**
	R_{Bulk} ($10^3\Omega$.cm)	C_{Bulk} (10^{-12}F.cm^{-1})	f^0_{Bulk} (Hz)	$R_{blocking}$ ($10^3\Omega$.cm)	$C_{blocking}$ (10^{-10}F.cm^{-1})	$f^0_{blocking}$ (Hz)	
HZA	16.8	5.5	1.8×10^6	3.84	15	2.4×10^4	18.6
HZB	144	3.0	4.6×10^5	3.7×10^5	1.6	1.3×10^4	37.6

Figure 56 shows the impedance diagram obtained at 600°C, for F2590-5 material. It is observed that this material, containing more vitreous phase than HZA, is 20 times less resistive than HZA at the same temperature (Figure 55 (a)). This result indicates that

the Na_2O-rich vitreous phase VPh_A is more conductive than VPh_B. Another important element that can be drawn from this comparison is that Na_2O-rich vitreous phase is more conductive than zirconia phase. Therefore, in materials containing VPh_A, the conductive matrix is the vitreous phase and the zirconia grains appear to be the insulating phase. In this case, it is impossible to characterize the transport properties of the zirconia phase by impedance spectroscopy.

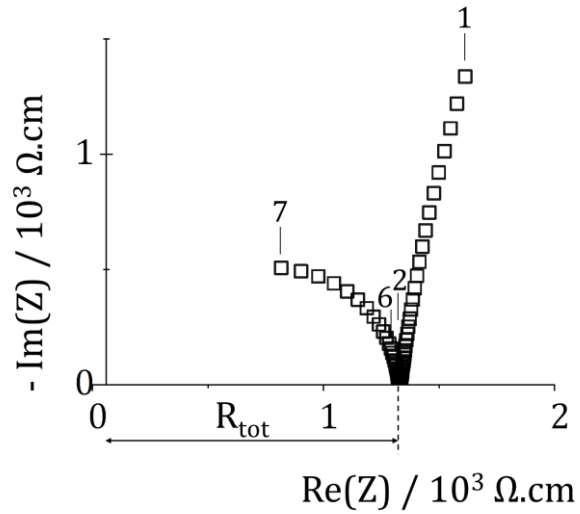

Figure 56: Impedance diagram at 600°C of F2590-5 material. The logarithms of the measuring frequencies are indicated by numerals.

On the other side, HZC material contains a vitreous phase of similar composition to that of HZB material (thus the same conductivity) but its concentration is higher. The comparison between Figure 53 (a) and Figure 55 (b), and Table 6 and Table 7, shows that the bulk impedance of HZC (Figure 53 (a)) is higher than that of HZB (Figure 55 (b) indicating that in these materials the vitreous phase is less conductive than zirconia phase. The same observation can be made for the blocking factor α_R (Table 6 and Table 7). HZC presents a higher α_R than HZB, which corresponds to more blocking zirconia/vitreous phase interfaces.

As a conclusion:

- It should be pointed out that the intrinsic electrical parameters, such as conductivity, of the zirconia matrix and the second phase cannot be determined from impedance diagrams (Figure 56).
- For the studied materials, the measured total conductivity depends on the composition of the vitreous phase: in the case of HZA, the vitreous phase is rich in Na_2O without B_2O_3. Consequently, the total conductivity is mainly modulated by the vitreous phase and not by the ZrO_2 matrix.

III.2 TEMPERATURE DEPENDENCE OF THE TOTAL CONDUCTIVITY

Figure 57 shows Arrhenius plots of the total electrical conductivities of the studied samples. The conductivity measurements are influenced by the zirconia phase since three domains are evidenced that can be related to the crystalline phase changes of zirconia: monoclinic, phase transition and tetragonal ranges. Tetragonal zirconia is indeed more conductive than monoclinic zirconia [125] because of a higher oxygen vacancy mobility. The phase transition is clearly observed around 1150°C. Only for F2590-5, where the zirconia phase transition is not clearly observed because of the high content in sodium vitreous phase masking the response of the zirconia phase of the refractory.

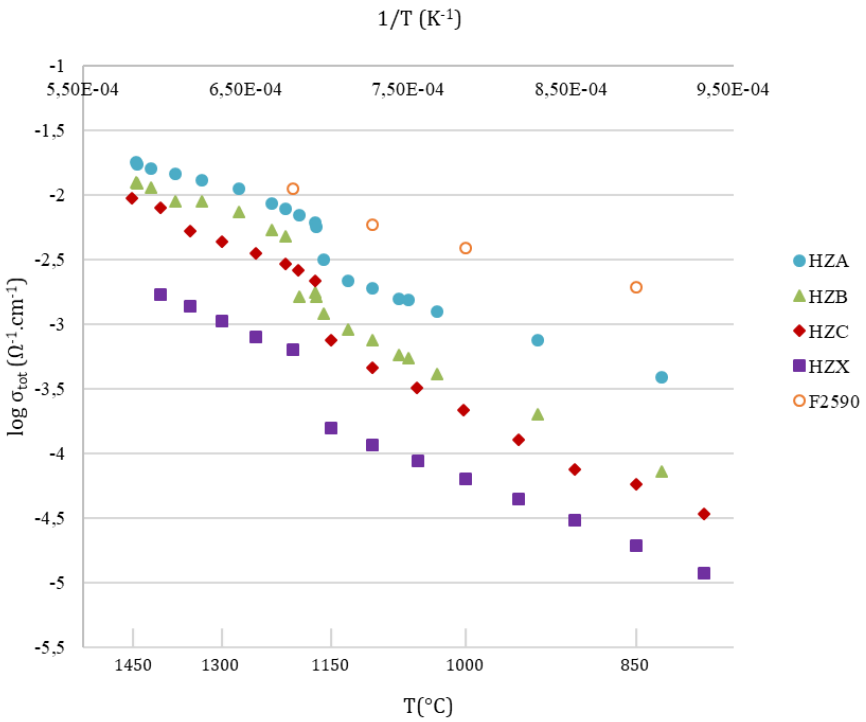

Figure 57: Arrhenius plot of HZA, HZB, HZC, HZS, HZX and F2590-5 refractories, between 550°C and 1450°C (heating), under air atmosphere, with platinum electrodes [126].

The Arrhenius law obeys equation (28), and equation (29) is used to have an access to the activation energy, Ea. The value of the slope of the linear regression of the plot log(σ) = f(1/T) gives the activation energy of the process.

$$\sigma = \sigma_o \,.\, \exp\left(-\frac{Ea}{k.T}\right) \quad (28)$$

$$\log(\sigma) = \log(\sigma_o) - \frac{Ea}{2{,}3.k.T} \quad (29)$$

where:

- σ: conductivity ($\Omega^{-1}.cm^{-1}$)
- S: surface of the pellet (cm^2)
- L: thickness of the pellet (cm)
- Ea: activation energy (eV)
- k: Boltzmann constant ($eV.K^{-1}$)
- σ_o: pre-exponential factor ($\Omega^{-1}.cm^{-1}$) in our case σ_{tot}

The calculated activation energy values are shown in Table 8. According to these results, two groups of materials can be considered. The first one (HZB, HZC and HZX) is characterized by an activation energy close to 1 eV which is similar below and above the zirconia phase transition (1150°C). This value is close to the activation energy of zirconia [127], and so the total electrical conductivity is modulated by the zirconia matrix. The second one (HZA and F2590-5) is characterized by a decrease of the activation energy from 0.8 eV down to 0.5 eV below the zirconia phase transition. The lower the activation energy, the higher the vitreous phase content in the refractory. These values are close to the activation energy of ionic conductivity of an alkali-silica glass below the glassy phase transformation [128, 129]. These results confirm that in case of a highly conducting vitreous phase, the total electrical conductivity is mainly modulated by the percolating vitreous phase.

Table 8: Activation energy based on Arrhenius heating slopes.

Reference	Ea below 1150°C (eV)	Ea above 1150°C (eV)
HZB	1.1	0.9
HZC	1.1	1.1
HZX	1.1	0.9
HZA	0.8	0.5
F2590-5	0.5	

III.3 TRANSPORT PROPERTIES IN THE HZFC REFRACTORIES

III.3.1 Electrical transport

Figure 58 gives examples of impedance diagrams of the HZC refractory, at 1100°C, under three oxygen partial pressures (pO_2), i.e., 1 bar, 0.2 bar, and 10^{-5} bar. The separation between the sample response and the electrode impedance is clear and it can be observed that the total sample resistance (R_{tot}) decreases as pO_2 increases.

The total conductivity of the material (σ_{tot}) can be calculated from the R_{tot} values and the geometrical factor of the sample.

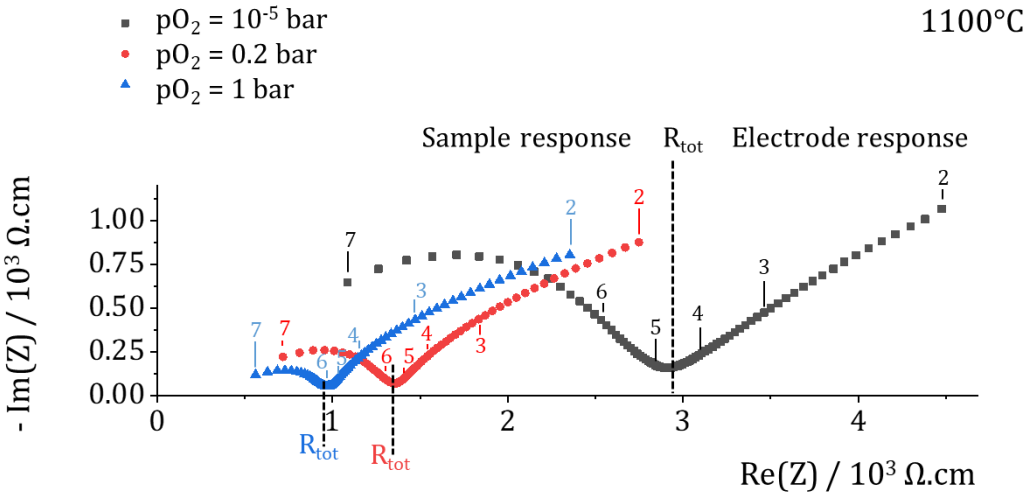

Figure 58: Impedance diagram of the HZC refractory, at 1100°C under three oxygen partial pressures. The numbers 1, 2, etc. indicate the $\log_{10}$ of the measuring frequency.

Figure 59 shows the variation of the total electrical conductivity of HZFC refractory as a function of the oxygen partial pressure, at 1100°C, referred to as a Patterson diagram [130-132]. The plot is characteristic of mixed ionic-electronic conductors: under oxygen partial pressures lower than 10^{-5} bar, the conductivity plateau indicates that the material can be considered as a purely ionic conductor, whereas, at high oxygen pressure an additional p-type electronic conductivity is observed [101, 133]. According to previous published results, the additional electronic conductivity can be ascribed to monoclinic zirconia [134].

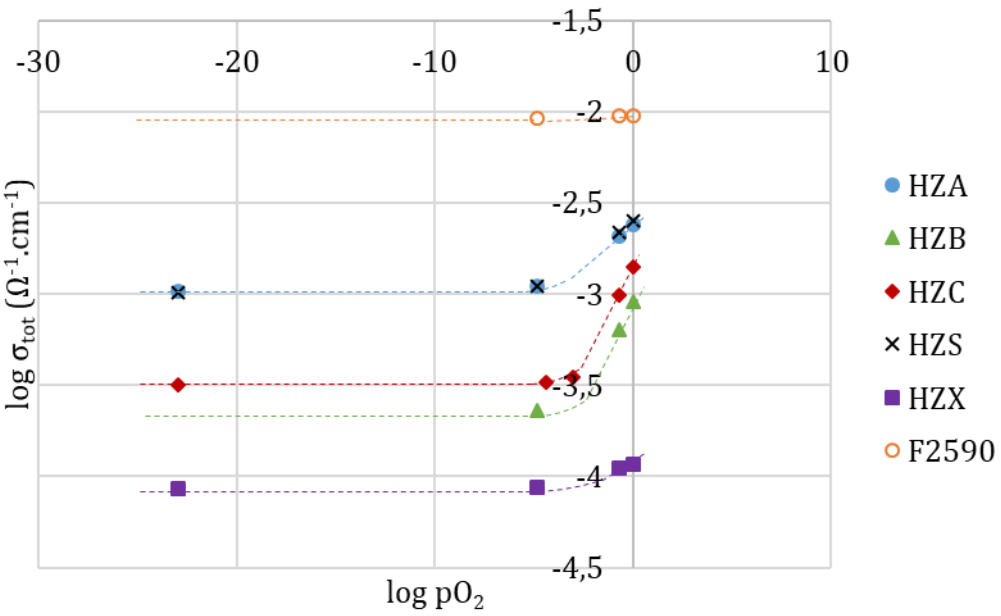

Figure 59: Patterson diagram at 1100°C for several refractory references under different pO_2. (The lines are only a guide for the eye).

Indeed, as explained before, HZFC refractories exhibit a p-type electronic conductivity at 1100°C, under high oxygen partial pressures, characterizing monoclinic zirconia. It means that under pO_2 lower than 10^{-5} bar the conductivity is purely ionic, whereas between $pO_2 = 10^{-5}$ bar and $pO_2 = 1$ bar the conductivity is mixed, ionic and electronic (MIEC).

The same behaviour was observed at 1200°C, above the monoclinic/tetragonal transformation of zirconia (Figure 60) for the first group of materials (HZB, HZC and HZX). However, for the second group (HZA, HZS and F2590-5), only a very small increase of the total electrical conductivity is observed at high oxygen partial pressure. According to our previous conclusions, this result confirms that, in these materials, the high conductivity of the vitreous phase impedes the identification of the p-type conductivity of the zirconia phase under high pO_2. The values from F2590-5 in Figure 59 also confirms that the glassy phase (rich in Na_2O) is purely ionic because no electronic contribution is observed. Therefore, there is no transport of matter through the vitreous phase.

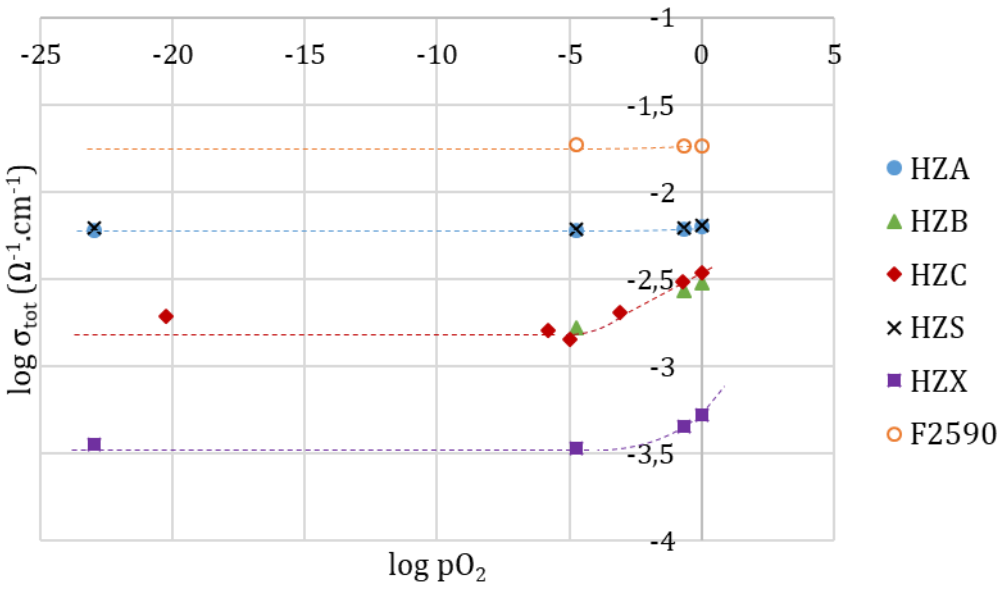

Figure 60: Patterson diagram at 1200°C for several refractory references under different pO_2. (The lines are only a guide for the eye).

Generally, it is possible to separate the ionic conductivity σ_i from the electronic σ_e one as the total conductivity σ_{tot} is expressed by:

$$\sigma_{tot} = \sigma_i + \sigma_e \qquad (30)$$

From these parameters, it is possible to calculate the electronic and ionic transport numbers:

$$t_e = \frac{\sigma_{tot} - \sigma_i}{\sigma_{tot}} \qquad (31)$$

$$t_i = 1 - t_e \qquad (32)$$

It should be pointed out that the pressure independent plateau, ascribed to ionic conductivity, is a contribution of both the zirconia and the vitreous phase. Consequently, the actual electronic transport number of zirconia cannot be evaluated precisely. However, owing to the mixed ionic-electronic conductivity of the material, an electronic ($t_e a$) and ionic ($t_i a$) apparent transport numbers can be calculated from the measurements. It should be pointed out that according to our previous remarks, the transport numbers can only be evaluated for the first group of refractories (HZB, HZC and HZX). Indeed, the properties of zirconia of references containing vitreous phase rich in sodium (HZA, HZS, F2590-5) cannot be interpreted since the vitreous phase hide the zirconia phase contribution.

Table 9 presents the apparent transport numbers calculated for 3 materials at 1100°C and 1200 °C. Normally the same transport numbers, for references containing undoped monoclinic zirconia, should be observed. It is the case for HZB and HZC references. However, for HZX the variation in electronic conductivity is observed to be smaller because monoclinic zirconia is doped by tantalum.

Table 9: Electronic and ionic apparent transport numbers at 1100°C and 1200°C for several refractory references.

1100°C	**HZB**	**HZC**	**HZX**
$t_e a$	0.75	0.8	0.24
$t_i a$	0.25	0.2	0.76
1200°C	**HZB**	**HZC**	**HZX**
$t_e a$	0.45	0.58	0.37
$t_i a$	0.55	0.42	0.63

It is observed while heating HZB and HZC refractory samples, that the ionic contribution becomes higher, indicating that the ionic conductivity increases faster with temperature than the electronic one. As already shown in the Arrhenius plots in a previous section, a gap in conductivity is observed at the zirconia phase transition. In the case of HZX, the total conductivity is very low but stay mainly ionic ($t_i a > 0.6$).

III.3.2 Mass transport through a conductive membrane

During the past two decades, intensive studies have been devoted to the development of ceramic membranes with the aim of maximizing the oxygen permeability. On the contrary, the objective of this thesis is to suggest a scenario for the blistering phenomenon involving refractories synthesized with the aim of minimizing or even eliminating the oxygen flux across the ceramic walls of the glass furnaces. However, it is essential to consider all the works published on semipermeable membranes. The concepts proposed in these previous works will be very useful for the analysis of the results obtained during this thesis. They are briefly reported in the following part.

If a macroscopic electric field is applied to an oxide ionic conductor, the ions can move in one direction, resulting in a net ionic flux through the conductor, corresponding to a "pumping mode". When a pressure gradient of the gas of the mobile species in the conductor is imposed, the ions can also move across the membrane in one direction. However, the electroneutrality within the material must be obeyed, and movement of the mobile ionic species, such as oxygen vacancies, must be compensated by a second type of defect, which is generally, in oxide conductors, an electronic defect, either electrons or electron holes. The permeation process is illustrated in Figure 61.

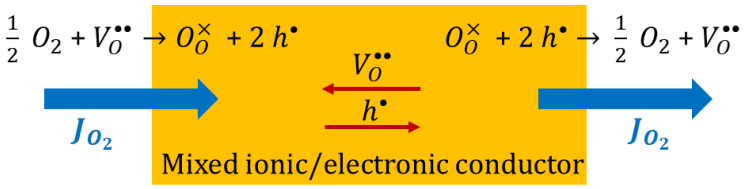

Figure 61: Illustration of the permeation process through a mixed ionic-electronic conductor, where O_2 is oxygen in the gas at the interface, O_O^X is oxygen in the material, $h^{\bullet}$ the holes and $V_O^{\bullet\bullet}$ the vacancy in the ceramic electrolyte.

Consequently, there is a correlation between the movement of ionic and electronic species within the oxide and the "Slowness Rule" can be applied. The "Slowness" is defined as the inverse of the rate of a process. The rule of the slowness is: "In a mixed kinetic regime, the slowness of the overall process is the sum of the slowness of each limiting step considered alone", i.e., if J is the oxygen flux and σ_V and σ_p are the conductivity of the oxygen vacancies and of the electron holes, respectively, then:

$$1/J = a/\sigma_V + b/\sigma_p.$$

If the oxide is a solid electrolyte ($\sigma_V >> \sigma_p$), then the oxygen permeation is governed by the transport of electron holes. On the contrary, in a semi-conductor ($\sigma_V << \sigma_p$), the oxygen permeation is governed by the oxygen vacancies. In both cases the oxygen permeation limiting step is ascribed to the minority carriers.

Various attempts have been proposed to improve the oxygen permeation flux across a membrane. Many works have been devoted to improve the oxide composition in order to improve either the ionic or the electronic conductivity [93]. Another concept proposed is referred to as "dual phase membrane". As an example, composites involving an ionic conductor and a metal, such as palladium [135, 136], or another

ceramic phase exhibiting a higher electronic conductivity, have been proposed [137, 138]. Figure 62 (a) shows a schematic cross-section of the composite and Figure 62 (b) gives an illustration of the permeation process.

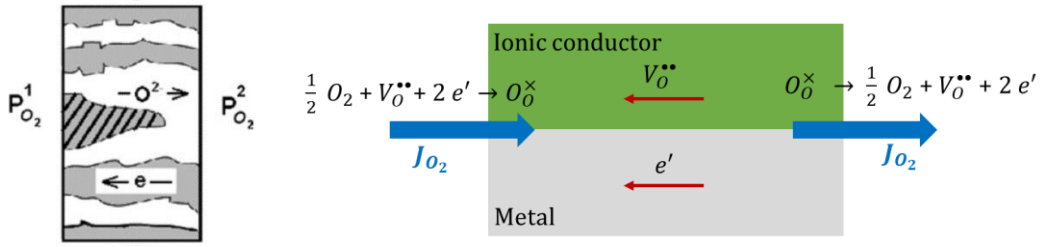

(a) (b)

Figure 62: (a) Schematized cross-section of a dual phase system, from [139], (b) Illustration of the permeation process through the composite.

Provided the dual phase system is percolating, it has been proved that the membrane is permeable to oxygen with oxygen vacancies, which are balanced by simultaneous transport of electrons in the metallic phase. However, the composites suffer often small compositional changes due to interaction between constituents, lowering the performance of the permeating membranes [140].

Composite electrolytes including an oxide-ion conductor and molten mixtures of alkaline carbonates have been recently suggested as CO_2 separation membranes. As illustrated in Figure 63, in these membranes, it is assumed that motion of carbonate ions is electrically balanced by a flow of oxide ions, yielding a net flow of CO_2 [141-143].

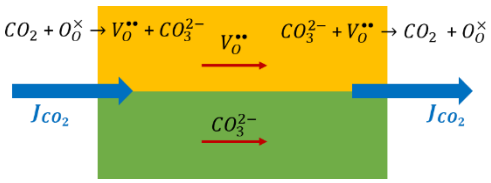

Figure 63: Illustration of CO_2 transfer through a pure oxide ion conductor/molten carbonate dual phase membrane, from [144].

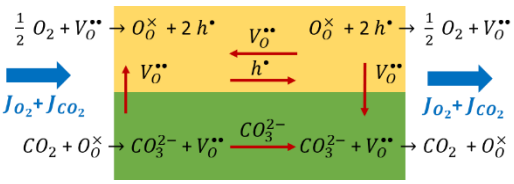

Figure 64: Illustration of CO_2/O_2 permeation through a mixed ionic-electronic/molten carbonate dual phase membrane, from [144].

As shown in Figure 64, if the solid oxide is a mixed ionic-electronic conductor, as an example by oxygen vacancies and electron holes, a simultaneous transport of CO_2 and O_2 is allowed, provided CO_2 and O_2 are flowing at the feed side.

The refractories studied in this work are composite materials involving a zirconia phase and a vitreous phase, as an example, conducting by sodium ions. Following the same approach, assuming that, at the feed side the vitreous phase is blocking for sodium ions, an oxygen transfer is possible through the membrane, provided zirconia is a mixed ionic/electronic conductor. Obviously, in case of a purely oxide ionic conductor, oxygen permeation is impossible, owing to the absence of charge compensation (Figure 65).

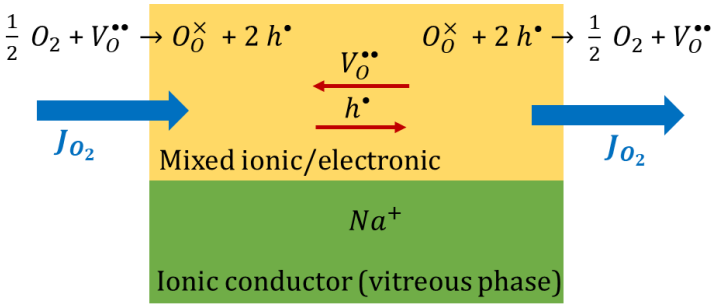

Figure 65: Illustration of an oxygen transfer through a composite membrane involving a mixed oxide ion conductor and a vitreous phase.

It should be noted that in the description of these permeation processes only diffusion processes were considered. Obviously, many steps have to be taken into account in the permeation process, i.e., gas transfer to and from the gas/solid interface, oxygen exchange at both interfaces of the membrane, etc. [145]. Various theories have been proposed for modelling the oxygen permeation process through a MIEC membrane [146].

Schematically, as shown in Figure 66, a simplified representation of the permeation process can be divided in seven steps [147, 148]:

- oxygen diffusion in the gas phase on the oxygen rich side (step 1)

- surface exchange reactions in the adsorbed layers on the rich side of the membrane, including adsorption and incorporation of oxygen into the crystal lattice (steps 2 and 3)
- bulk diffusion within the membrane (step 4)
- surface exchange reactions in the adsorbed layers on the oxygen lean side of the membrane, including extraction of oxygen from the crystal lattice, recombination into oxygen molecules, and desorption of oxygen (steps 5 to 7)
- oxygen diffusion in the gas phase on the oxygen lean side (step 7)

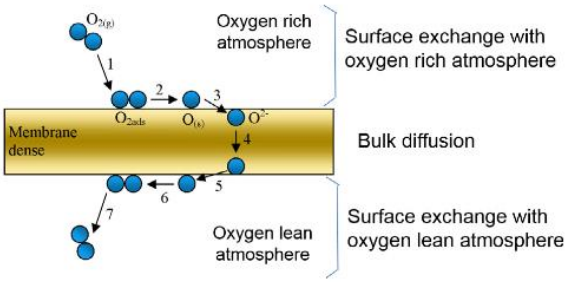

Figure 66: Steps for oxygen transport through the MIEC [148].

Macroscopically, as illustrated in Figure 67, in addition to transport by electrochemical diffusion through the membrane, surface exchanges processes have to be considered. The main consequence is that one or both surfaces of the membrane are not in equilibrium with their environment, either a gas or a molten glass, leading to a polarization phenomenon [67, 100, 149, 150]. As it will be shown in Chapter 4, a polarization phenomenon is observed at the gas/refractory interface and, in a few cases, at the molten glass/refractory interface.

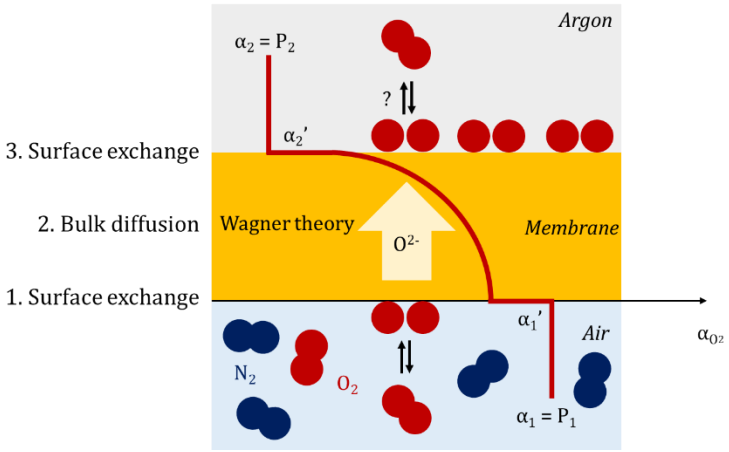

α 1: activity of the gas rich in oxygen

α 2: activity of the gas poor in oxygen

α'1: activity of the interface oxygen rich side/refractory

α'2: activity of the interface oxygen lean side/refractory

P_1: oxygen partial pressure in the rich side (air)

P_2: oxygen partial pressure in the lean side (argon)

Figure 67: Illustration of the polarization phenomena at both interfaces of a permeation membrane: the oxygen activity at the surface is not in equilibrium with its environment, from [148]. The gradient of oxygen activity between both surfaces can be not sufficient anymore to allow the transport.

When the membrane thickness is large and/or the surface exchange reactions proceed very rapidly, the bulk diffusion is the rate limiting step. The bulk diffusion process can be controlled by either oxygen ionic or electronic conduction, or both of them [95, 150-153]. Assuming that the permeation process is a one-dimensional volume diffusion rate-limited process, according to Wagner, the steady state oxygen permeation flux density in a mixed conductor is given by [146, 152, 154]:

$$j_{O_2} = \frac{RT}{16\,F^2\,L}\int_{P_{O_2}^{lean}}^{P_{O_2}^{rich}} \frac{\sigma_i \,.\, \sigma_e}{\sigma_i + \sigma_e}\; d\,ln\,p_{O_2}$$

where all the symbols have their original meaning, σ_i. σ_e and $\sigma_{tot.}$ are respectively the ionic, electronic and total conductivities and L is the membrane thickness. The term $\frac{\sigma_i \,.\, \sigma_e}{\sigma_i + \sigma_e}$ is defined as the *ambipolar conductivity*, which can be also written as:

$$\sigma_{amb} = \frac{\sigma_i\,\sigma_e}{\sigma_{tot}} = \frac{\sigma_i\,\sigma_e}{\sigma_i + \sigma_e} = t_i\,\sigma_e = t_e\,\sigma_i = t_i\,t_e\,\sigma_{tot}$$

In case of composite materials, for considering all the microstructural aspects a tortuosity factor τ (with $\tau \geq 1$), is sometimes, introduced as a global parameter [143]:

$$j_{O_2} = \frac{RT\,\sigma_i}{16\,F^2\,L\,\tau}\int_{P_{O_2}^{lean}}^{P_{O_2}^{rich}} \sigma_{amb}\; d\,ln\,p_{O_2}$$

In the case of mixed conductors in which the electronic conduction predominates, i.e., $\sigma_e \gg \sigma_i$, the integral in the Wagner relation involves only σ_i over the oxygen partial pressure gradient, in agreement with the slowness rule:

$$j_{O_2} = \frac{RT}{16\,F^2\,L} \int_{P_{O_2}^{lean}}^{P_{O_2}^{rich}} \sigma_i \; d\; lnP_{O_2}$$

Considering an average value for σ_i, or assuming σ_i to be constant, simplifies the equation so that j_{O_2} is directly proportional to σ_i and $ln\frac{P_{O_2}^{rich}}{P_{O_2}^{lean}}$:

$$j_{O_2} = \frac{RT\,\sigma_i}{16\,F^2\,L}\, ln\frac{P_{O_2}^{rich}}{P_{O_2}^{lean}}$$

In case of a solid electrolyte, in which the ionic conduction predominates, i.e., $\sigma_i \gg \sigma_e$, the integral in the Wagner relation involves only σ_e:

$$j_{O_2} = \frac{RT}{16\,F^2\,L} \int_{P_{O_2}^{lean}}^{P_{O_2}^{rich}} \sigma_e \; d\; lnP_{O_2}$$

Assuming, as an example, that the electron holes are the electronic defects, we can write, using the law of mass action (K is the equilibrium constant):

$$\frac{1}{2}\, O_2 + V_O^{\bullet\bullet} \;\leftrightarrow\; O_O^{\times} + \; 2\, h^{\bullet}$$

and $$[h^{\bullet}] = K^{1/2}\, P_{O_2}^{1/4}\, [V_O^{\bullet\bullet}]^{1/2}$$

The electron hole concentration is then proportional to $p_{O_2}^{1/4}$, if the concentration of oxygen vacancies is considered as constant, the electronic conductivity σ_h can be written:

$$\sigma_h = \sigma_h^o\, P_{O_2}^{1/4}$$

Then, the oxygen permeation flux becomes:

$$j_{O_2} = \frac{RT\,\sigma_h^o}{16\,F^2\,L} \left[P_{O_2}^{(rich)1/4} - P_{O_2}^{(lean)1/4}\right]$$

Obviously, as shown in Section III.3.1, in the studied refractories neither the ionic conductivity nor the electronic one can be neglected and ambipolar conductivity has to be used. As shown previously, the actual partial conductivity cannot be precisely determined; consequently, the calculated ambipolar conductivities are apparent values. The apparent ambipolar conductivity for several refractories, calculated from the ionic and electronic conductivities calculated previously, is given in Table 10. As explained

before, ambipolar conductivity can only be estimated when the material does not have an overly conductive glass phase. The transport numbers and the ambipolar conductivities of HZB and HZC are equivalent. In the case of HZX the ambipolar conductivity is about 10 times lower at 1100°C because of the zirconia doping by tantalum.

Table 10: Apparent electronic, ionic and ambivalent conductivities at 1100°C and 1200°C in Ω^{-1}. cm^{-1} (or $S.cm^{-1}$) for several references, calculated with the electronic and ionic apparent transport numbers.

1100°C	**HZB**	**HZC**	**HZX**
σ_e	$6.8x10^{-4}$	$1.1x10^{-3}$	$2.9x10^{-5}$
σ_i	$2.3x10^{-4}$	$3.3x10^{-4}$	$6.7x10^{-5}$
σ_{amb}	$1.7x10^{-4}$	$2.5x10^{-4}$	$2.2x10^{-5}$
1200°C	**HZB**	**HZC**	**HZX**
σ_e	$1.4x10^{-3}$	$2x10^{-3}$	$1.9x10^{-4}$
σ_i	$1.7x10^{-3}$	$1.4x10^{-3}$	$3.4x10^{-4}$
σ_{amb}	$7.4x10^{-4}$	$8.4x10^{-4}$	$1.2x10^{-4}$

These values will be used in chapter 4 for analysing the semipermeability results on various molten glass/refractory systems.

III.4 CONCLUSION

One of the main results of this study was to demonstrate that the vitreous phase modulates the impedance diagram. Therefore, it is not possible to determine independently the conductivity of both zirconia and vitreous phases. The behavior of the conductivity as a function of temperature depends on the vitreous phase content and nature. It leads to separate the studied materials in two groups, according to the conductance of the vitreous phase. All the materials were characterized by a mixed ionic and electronic conductivity. However, it should be pointed out that the intrinsic mixed properties of the refractories can be experimentally hidden by the vitreous phase.

Chapter IV: Key parameters of the blistering at the glass/refractory interface

IV.1 INTRODUCTION

The blistering of a glass in contact with refractory materials is a phenomenon that is difficult to study *in situ*. Few cases in real conditions of use are precisely documented and it is generally difficult to estimate the implication of refractories in the creation of bubbles. This is why several laboratory tests described in Chapter 2, complementary to those already existing in Saint-Gobain research centers, were carried out during this thesis in order to study the influence of the different parameters. The aim of these experiments is to study refractory materials and recreate the contact between glass and refractories at high temperature, in order to build the blistering scenario of a molten glass in contact with a refractory material inside a glass furnace. It has been observed in previous studies that the external atmosphere had to be rich in oxygen to start the permanent intense blistering of glass. According to the literature (see Appendix D), zirconia is a mixed ionic and electronic material; consequently, it was assumed at the beginning of the thesis that the blistering phenomenon could be ascribed to a semipermeability flux through the refractory. If transport phenomenon occurs in the material, the semipermeability is, indeed, a major parameter to study. It is essential to distinguish physical permeability and electrochemical oxygen permeability also called semipermeability, since the impact of the physical permeability in the blistering mechanism should be limited, due to the low open porosity rate (< 6%) of the refractories. Moreover, if bubbles result from physical permeability, they are composed of air and not only of oxygen. In the case of an oxygen electrochemical permeability through a dense material, two charged species (see chapter 2) ensure the transport and only oxygen bubbles into the molten glass are formed (Figure 68).

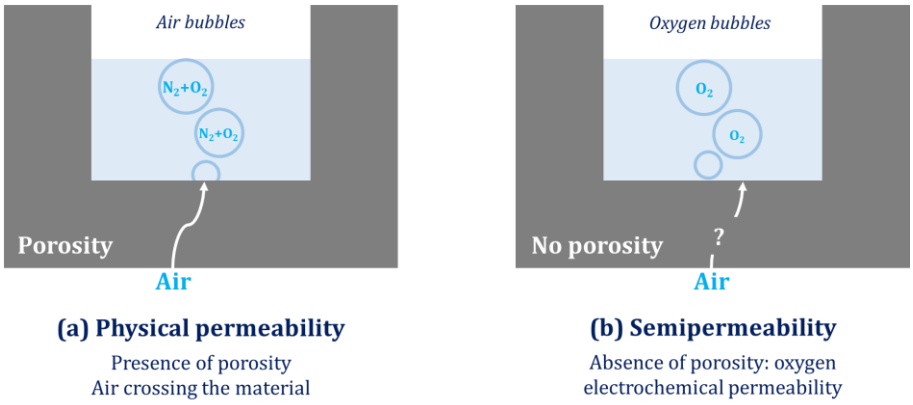

Figure 68: Differences between physical permeability and electrochemical permeability.

In this chapter the oxidation state of the refractory is studied first. The role of the semipermeability flux is also demonstrated in the following section to build a coherent blistering scenario including various parameters. After that, tomography results are presented in order to characterize the biphasic material and the distribution of the zirconia phase. Complementary experiments were also performed, either to confirm the obtained results (external electrochemical polarization, see Section IV.2.3), or to understand the variation with time of the blistering intensity (microstructural modification of the glass/refractory interface, see Section IV.2.5). From the new information obtained through all these experiments, a lot of previous results could be interpreted and form an integral part of the proposed scenario described in chapter 5.

IV.2 KEY PARAMETERS OF THE BLISTERING IN CONTACT WITH THE FUSED-CAST REFRACTORIES

IV.2.1 Redox state of the refractory

Prior to XANES measurements carried out during the thesis, it was admitted that an orange colour of the material after a thermal treatment under air, led to an oxidized state of the HZFC refractory. Titanium and iron impurities were suspected to play a role in the oxidation mechanism. According to the XANES results performed in 2018 at ESRF in Grenoble with J. Durst (SGR Paris), there is no influence of titanium because it shows no change of its oxidation state whatever the conditions of thermal

treatment. Titanium always remains to a Ti(IV) oxidation state for a raw (without any heat treatment) and for an oxidized material (with heat treatment under air atmosphere). These XANES characterizations demonstrated for the first time that the colour taken by a high zirconia fused cast refractory (dark grey, light grey, yellow/orange) is indicative of the iron oxidation state.

It is observed that all the raw refractories tested have their impurities at a significant fraction of metallic iron. Since the materials are heterogeneous, some spatial heterogeneities can be found where concentrations can even reach almost 100% metallic Fe in the pristine materials (raw materials). Otherwise, the metallic state represents 60-70%, the other redox states, Fe(II) and Fe(III), represent respectively 15-30% and 5-10% (Figure 69). When comparing the three materials and their behaviour with respect to thermal oxidation, a differentiation between bulk and surface oxidation behaviours is made in case of an incomplete oxidation.

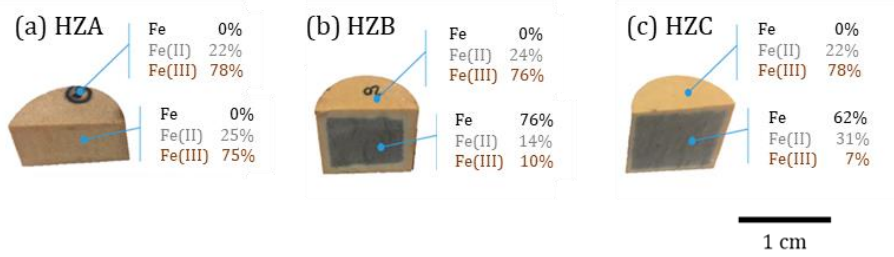

Figure 69: Redox states of iron in fused-cast refractories after heat treatment (10 hours at 1100°C under air) measured by XANES at ESRF, Grenoble [155].

At the surface, all the materials reach the same oxidation state, with no more metallic iron. After 10 hours at 1100°C in air, the metallic iron content is oxidized into Fe(II) at around 20% and Fe(III) at around 80%. As shown in Figure 69, different iron oxidation states within the refractory are achieved, for this test duration, depending on its composition. There is always a good agreement between the colour of the refractory and the oxidation state of its iron impurities. When metallic iron is mostly present, the refractory is grey and even turns into dark grey with 100% metal iron. With Fe(II)-rich phases, the refractory takes a low grey/blue colour and, with Fe(III)-rich phases, the refractory is turning yellow/orange. In raw refractories, Fe impurities in a highly reduced state are mostly in the glassy phase of the refractory in contact with the

zirconia grains. It is for example possible to observe iron nodules in the glassy phase in contact with zirconia grains with SEM observations (Figure 70).

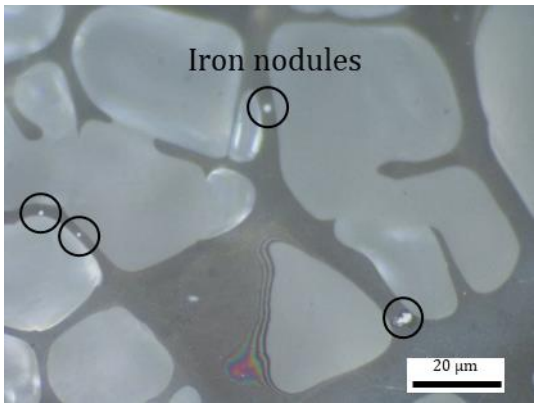

Figure 70: SEM observation of iron nodules in the glassy phase of a HZFC refractory (P. Vespa, SGR Provence).

Iron impurities are out of equilibrium and so oxidize rapidly when the material is heated in presence of a source of O_2, whether this source comes from the glass or from the external atmosphere. Oxygen oxidizes the surface Fe species but it is also able to diffuse inside the refractories. The global reactions of iron oxidation are the following:

$$\tfrac{1}{2}\ O_2 + Fe \rightarrow FeO \qquad (33)$$

$$\tfrac{1}{2}\ O_2 + 2\ FeO \rightarrow Fe_2O_3 \qquad (34)$$

For both reactions, the free Gibbs energy is negative, consequently, the reactions are spontaneous. The oxidation of iron particles within the refractory can be explained by the high temperature metallic corrosion concept [156]. Let us consider a sample of iron oxidizing in presence of air to form a layer of a non-stoichiometric oxide, such as $Fe_{1-x}O$. Using Kröger-Vink notation, the structure of this oxide can be written as following:

$$(1-x)\ Fe_{Fe}^{\times} + x\ V_{Fe}'' + O_O^{\times} + x\ h^{\bullet} \qquad (35)$$

Consequently, $Fe_{1-x}O$ is a mixed ionic-electronic conductor (through iron vacancies and electron holes). The particularity of this phenomenon is that corrosion takes place at two different places of the material. At the external interface, the one in contact with the air atmosphere, the reduction of oxygen takes place. At the same time, at the

internal interface of the refractory, the oxidation of iron takes place (Figure 71). A simplified oxidation mechanism can be described in three steps:

1. at the external interface (refractory/air interface): oxygen reduction, referred to as "external half-reaction":

$$\frac{1}{2}\,O_2 \rightarrow O_O^{\times} + V_{Fe}'' + 2\,h^{\bullet} \quad (36)$$

2. at the internal interface (refractory/iron particle interface): iron oxidation, referred to as "internal half-reaction":

$$\mathrm{Fe} + V_{Fe}'' + 2\,h^{\bullet} \rightarrow Fe_{Fe}^{\times} \quad (37)$$

3. diffusion of the iron vacancies and electron holes through the oxide.

Leading to the following global reaction:

$$\tfrac{1}{2}\,O_2 + \mathrm{Fe} \rightarrow \mathrm{FeO} \quad (38)$$

Obviously, the corrosion reaction proceeds provided that the iron oxide is a mixed ionic-electronic conductor.

The limiting step of the oxidation can be either the transport in the oxide or the interface reactions. As shown in Figure 71, FeO being a p-type semi-conductor, the defects are generated at the external interface layer, and the FeO lattice is also built at the external interface (cationic diffusion) of the particle.

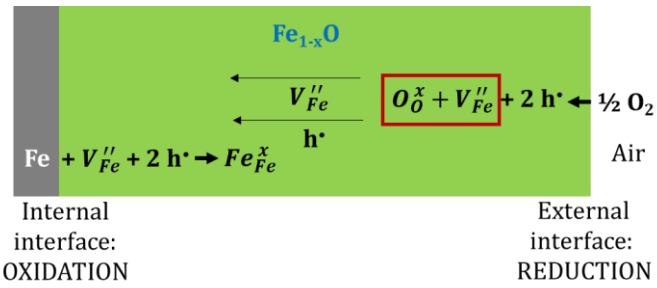

Figure 71: Simplified mechanism of dry corrosion phenomenon of iron at high temperature.

The same explanation can be referred in case of an iron particle precipitated in the zirconia phase (ZrO_{2-x}), even if the iron content in zirconia is very low, considering that zirconia is a mixed ionic-electronic conductor at high temperature (through

oxygen vacancies and electrons). The simplified oxidation mechanism of an iron particle is schematized in Figure 72.

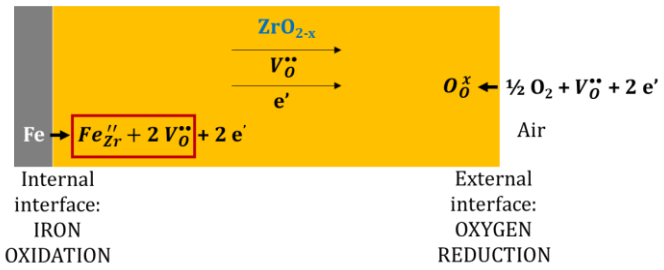

Figure 72: Simplified mechanism of the oxidation of an iron particle precipitated in zirconia.

According to this mechanism, iron particles are capturing the oxygen, that impedes oxygen to diffuse across the refractory as long as the entire refractory is not oxidized (see Figure 73). This mechanism explains both the oxidation of iron particles and the absence of permeation flux as it will be demonstrated in Section 4.2.2.

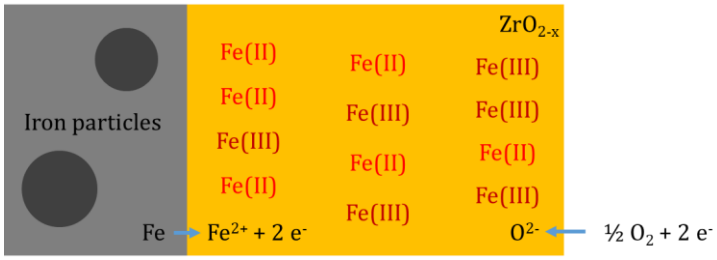

Figure 73: Illustration of the oxidation of the iron particles.

It should be recalled that the iron particles are mostly located within the glassy phase. The glassy phase is a pure ionic conductor and an oxygen permeation flux within this phase cannot be referred. It can be assumed that the proposed oxidation mechanism of iron particles, schematized in Figure 71 and Figure 72 can be applied: the iron particles within the glassy phase will be, first, oxidized at the interface between the vitreous phase and the zirconia grains (Figure 72), then the size of the iron particles decreases by a corrosion reaction schematized in Figure 71. The iron particle could remain in the glassy phase and oxidize via the mechanism shown in Figure 72, without FeO formation since Fe(II) "dissolves" in the zirconia phase.

XANES measurements were also performed on slices machined from self-crucible blistering tests, after 30 hours at 1100°C under air atmosphere tests. For a HZC slice, as an example, Position 4 (Figure 74) shows that the extrados has the lowest metallic iron proportion and the highest oxidized iron proportion of the slice cross-section. When going towards the bulk of the crucible, the proportion of metallic iron increases and decreases again near the glass interface. On the contrary, the proportion of Fe(II) and Fe(III) decreases in the bulk of the material and increases again at the glass interface. As explained before, the raw part of the material is characterized by the presence of metallic iron and the oxidized parts are characterized by the presence of Fe(II) and Fe(III) (glass and air interface).

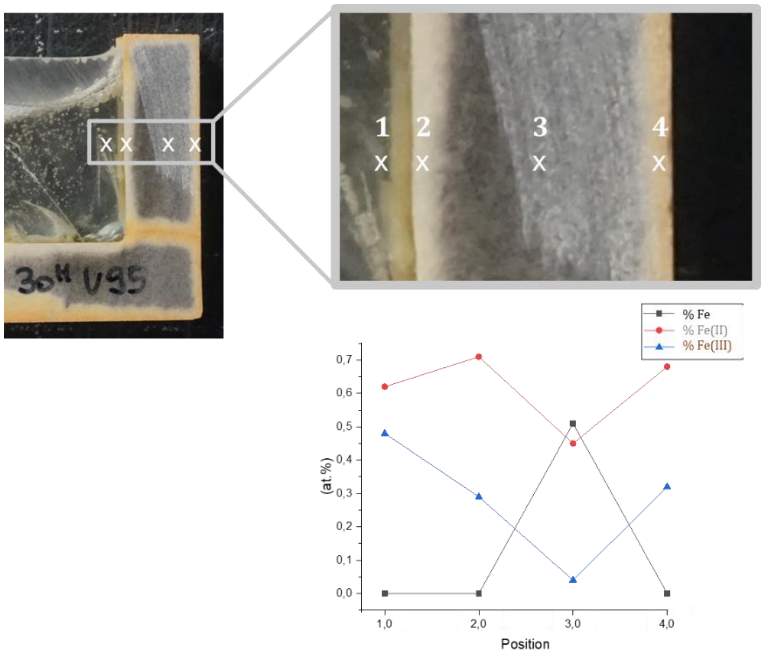

Figure 74: Redox states of iron measured by using XANES at ESRF, Grenoble.
Profile from the extrados to the glass interface of a HZC self-crucible slice (tested during 30 hours at 1100°C under air in contact with glass AKM).
Bulk (raw) part: 50% Fe metal with Fe(II),
Oxidized part: no more Fe metal, replaced by Fe(II) and Fe(III).

More recent XANES measurements (performed in 2019 and 2020 at SOLEIL in Saclay with S. Brossard, SGR Paris) confirmed the conclusions of the previous study. Before oxidation, for the raw sample, mostly metallic Fe with some FeO is observed, whereas after heat treatment no metallic Fe remains in the oxidized parts of the refractory.

The oxidation of the material has an important role in the blistering phenomenon. As illustrated in Figure 75, as long as the whole thickness of the material is not oxidized, blistering cannot begin.

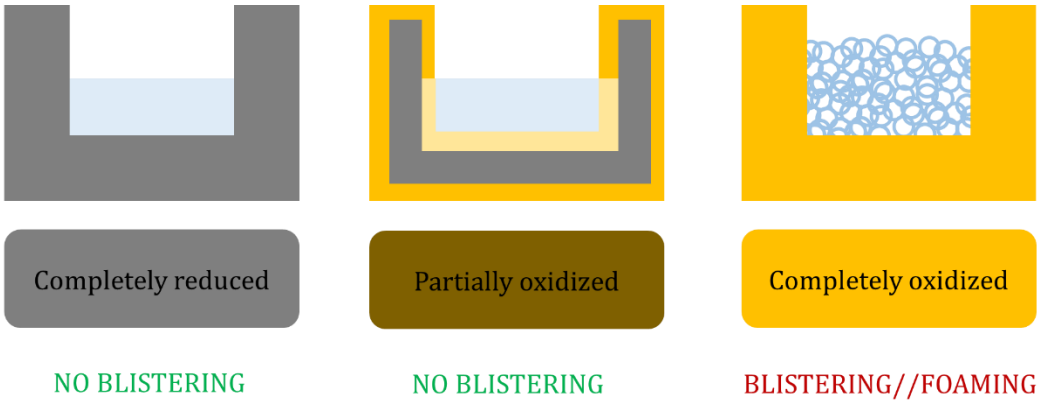

Figure 75: Illustration of the conditions necessary to observe blistering phenomenon. Glass in contact with refractory cannot generate bubbles as long as the whole thickness of the crucible is not oxidized.

Consequently, as it will be demonstrated experimentally later on, the necessary complete oxidation of the refractory explains the delay of the blistering phenomenon observed when starting with raw refractories [63].

IV.2.2 Electrochemical permeability

By using the set-up developed at LEPMI (see chapter 2), the semipermeability phenomenon through the refractories has been characterized. An oxygen partial pressure difference is created between the surfaces of the refractory material, i.e., an atmosphere rich in O_2 (0.2 bar) on one side and an argon atmosphere (10^{-5} bar) on the other side. The gas | refractory | gas configuration was first studied (Figure 76) and the oxygen sensor P_2 characterises the semipermeability flux (P_2 - P_1) passing through the refractory pellet as explained in Chapter 2.

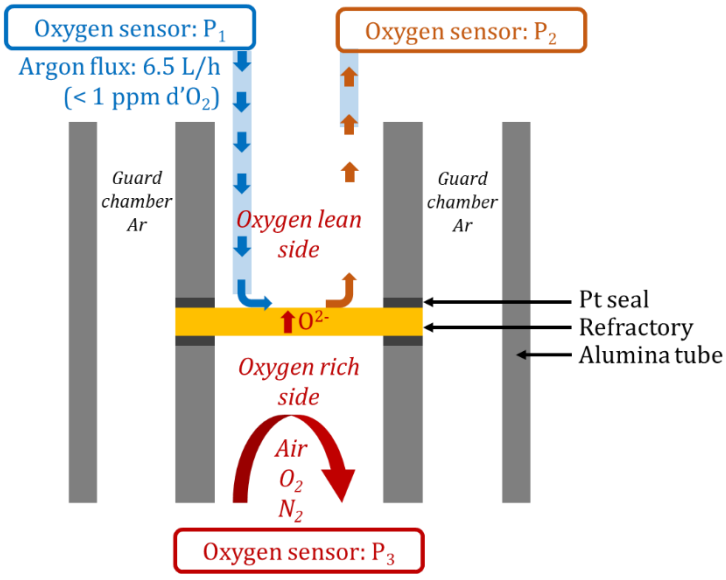

Figure 76: Semipermeability set-up in gas | refractory | gas configuration as presented in Chapter 2.

However, in this configuration the oxygen flux is too low to explain the intense blistering occurring when it is in contact with glass, even at high temperature. As it will be shown hereafter, in case of blistering through the glass melt, the oxygen content downstream the cell was, generally, of a few hundred ppm or even more. In comparison, less than 10 ppm with a gas/refractory/gas configuration were obtained (Table 11).

Table 11: Results of semipermeability flux measurement (in 10^{-6} bar) of HZA pellet without glass contact, as a function of temperature (gas | refractory | gas configuration).

T_{pellet} (°C) HZA	$P_2 - P_1$ (10^{-6} bar)
1127	5.4
1227	7.2
1328	10.8

This observation is explained by a polarization phenomenon as detailed in Chapter 3. While a semipermeation is present, if the oxygen diffused at the upper interface of the refractory (oxygen lean side) does not evacuate, the activity on the surface increases and progressively reaches the same activity of oxygen as at the rich side. The gradient of oxygen activity between both surfaces, which is the driving force of the

semipermeability process, disappears and the semipermeability phenomenon is stopped. Consequently, as described in Chapter 2 (Figure 39), the semipermeability set-up was modified to study *in situ* the refractory/glass interface by adding molten glass. Glass in contact with the refractory is essential for studying the electrochemical permeability to mimic the situation in glass industry. It was observed that in this case, oxygen does not accumulate on the upper surface of the refractory, erasing the polarization phenomenon. The oxygen flux crossing the glass/refractory interface induces the nucleation of bubbles in the glass and the observation of the blistering phenomenon through the oxygen sensor each time a bubble bursts on the glass/gas interface. An example is shown in Figure 77, where the variation of the oxygen content in flowing argon downstream the cell, is given as a function of time at 1100°C; using a raw refractory crucible. The emf (electromotive force) was recorded continuously and a calculation of the oxygen pressure was made every second (Figure 77). Each peak observed in the graph Figure 77 (a) (emf response) or Figure 77 (b) (instantaneous O_2 volume), corresponds to the oxygen release of a bubble or several bubbles when they (it) burst(s). Figure 77 (c) was obtained by integration of the oxygen evolving from the molten glass.

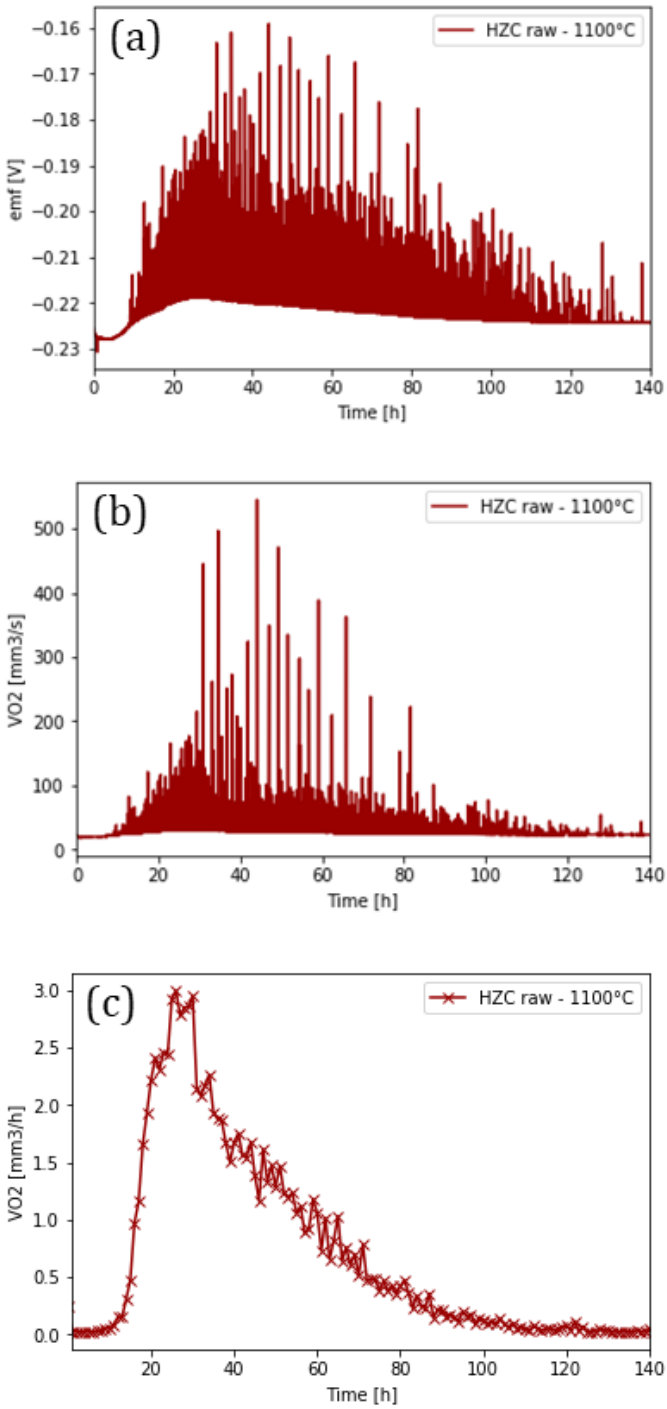

Figure 77: Semipermeability experiment to study the blistering of a AKM glass in contact with a raw HZC (1100°C – pO2=0.2 bar), (a) emf in function of time, (b) oxygen flux (in mm^3/s) and (c) oxygen flux per hour.

As the semipermeability measurements are characterized by an oxygen sensor, only the oxygen mole fraction within the bubbles is measured and it is not possible to ensure that the gas contained in bubbles is only oxygen. For analysing the various components of the permeating gas, a mass spectrometer was added downstream the oxygen sensor.

The blistering of pure oxygen bubbles is clearly observed with the mass spectrometer even if the blistering is low in intensity. No nitrogen is detected in the bubbles produced. As the acquisition of the mass spectrometer lasts 5 seconds, no peaks can be clearly identified as with the oxygen sensor which measures in real time the burst of bubble(s).

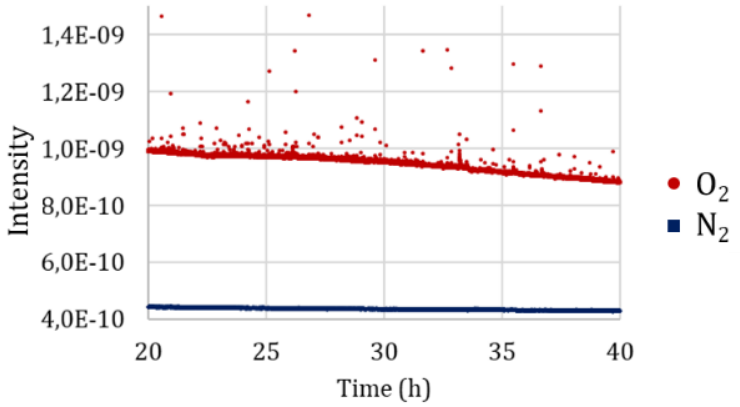

Figure 78: Mass spectrometer analysis of the gases released by the bubble burst of HZC tested at 1100°C under pO_2 = 0.2 bar in the semipermeability set-up.

To summarize:

- Refractory | gas configuration: no oxygen detected with the semipermeability set-up because of the polarisation phenomenon.
- Refractory | glass configuration: oxygen flux detected each time a bubble bursts in the semipermeability set-up.

Influence of oxygen partial pressure (pO_2)

As already observed in previous studies, the outside atmosphere must be rich in oxygen to be an oxygen source for the blistering mechanism. Under inert atmosphere (argon) below or above 1150°C (zirconia phase transition during heat-up), no blistering phenomenon is measured with the oxygen sensor in the semipermeability set-up. Indeed, no oxygen bubbles should be observed since no oxygen is feeding the blistering mechanism. We made experiments to demonstrate that it is possible to

switch off an existing blistering, by removing oxygen from the extrados interface of the self-crucible (P_3 in Figure 79).

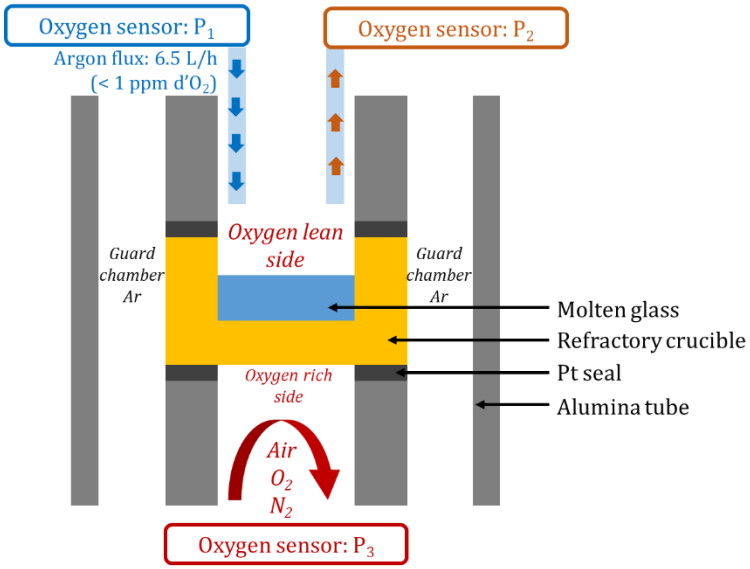

Figure 79: Semipermeability set-up to study the influence of the glass in contact with the refractory at high temperature.

To demonstrate the stop of the blistering phenomenon by lowering the partial pressure of oxygen at the rich side (extrados P_3), the oxygen partial pressure was changed from $pO_2 = 0.2$ bar down to $pO_2 = 1\times10^{-5}$ bar (argon) at t = 12.5 h (see Figure 80).

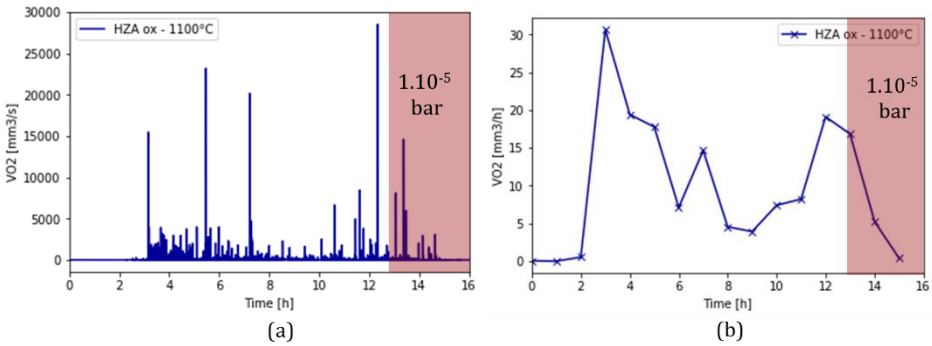

Figure 80: Semipermeability experiments to demonstrate the blistering switch off of a AKM glass in contact with a HZA pre-oxidized refractory at 1100°C: $pO_2 = 0.2$ bar till 12.5 h and $pO_2 = 10^{-5}$ bar after 12,5 h. (a) Oxygen peaks during blistering and (b) integration of the oxygen flux (in mm^3/h) as a function of time.

However, the blistering switch-off is not instantaneous after lowering the pO_2 since bubbles already formed in the glass are still growing and rising up in the glass until they burst. As explained before, this time is dependent on the viscosity of the glass studied. Once the blistering phenomenon is completely stopped it can start again while changing the oxygen partial pressure at the rich side of the semipermeability set-up.

Influence of the refractory redox state on the incubation time

As demonstrated in Section 4.2.1, the refractory must be completely oxidized before blistering can take place. Refractory material is "oxidized" when metallic iron impurities are at their higher oxidation level. Indeed, as long as Fe(0) or Fe(II) capture oxygen, oxygen is not available to reach the glass/refractory interface and so participate in the blistering mechanism. Fe(II) is being oxidized as long as the Fe(II)/Fe(III) equilibrium is not reached. A material is considered to be completely oxidized when O^{2-} ions reach the glass/refractory interface. The influence of the redox state of the refractory results in differences of the incubation period before the first observation of the blistering. Indeed, a raw refractory has a higher incubation period before the blistering (13 hours) than the oxidized one (2 hours) as observed in Figure 81.

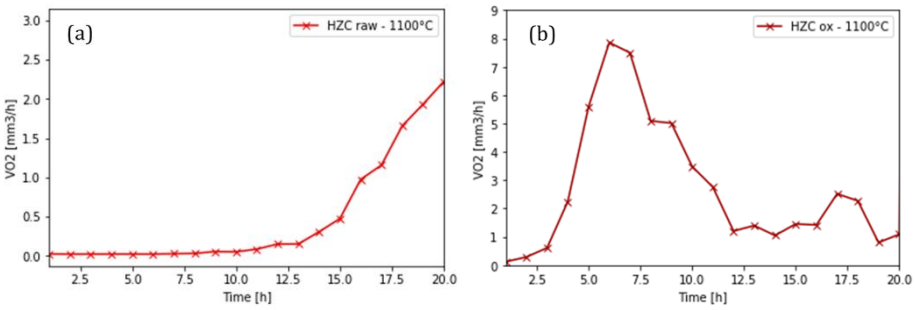

Figure 81: Blistering of AKM glass in contact with a raw (a) and oxidized (b) HZC – pO_2 = 0.2 bar at 1100°C.

According to these results obtained thanks to the semipermeability set-up, the oxidation of the material appears to be a major limiting step in the blistering phenomenon. For all the experimentations performed on the same preoxidized

reference, blistering started after almost 2 hours (Figure 82). This good repeatability allows us to compare the incubation time of the different experiments.

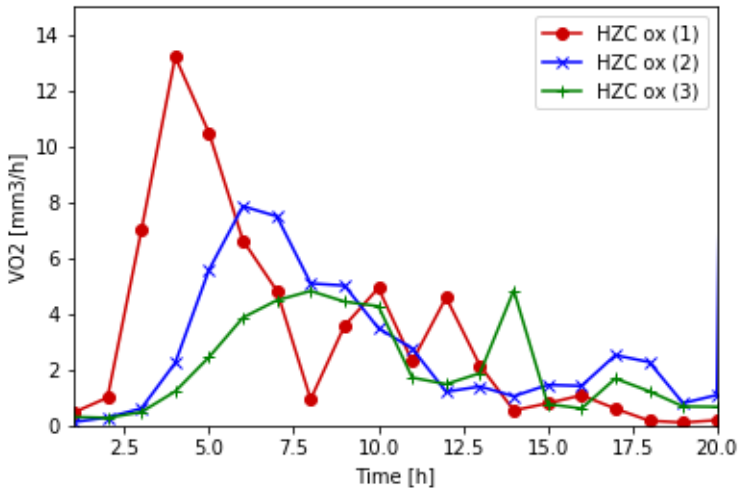

Figure 82: Volume of oxygen as a function of time obtained for AKM glass at 1100°C – pO2 = 0.2 bar in contact with preoxidized HZC for 3 different samples.

As the blistering phenomenon is only possible when the refractory is completely oxidized, the time before blistering is linked to the reduced iron content in the refractory composition and the iron redox influenced by the manufacturing process, leading to a variation in the oxidation time. This result is confirmed once again while testing oxidized materials (pretreatment before the semipermeability test during 30 hours at 1350°C under air atmosphere to completely oxidize the crucibles). As shown in Figure 83, the blistering starts with each reference after the same incubation duration, i.e., 2 hours. This feature indicates that for pre-oxidized refractories, the incubation time cannot be ascribed to the refractory reference, only to the glass properties.

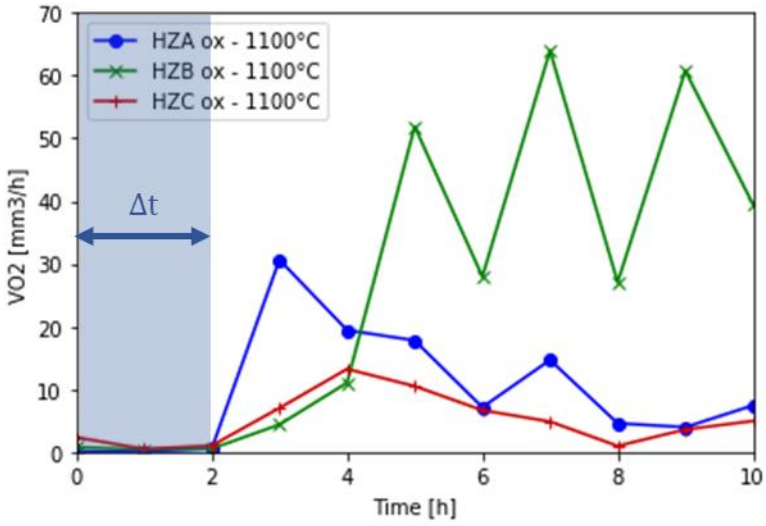

Figure 83: Comparison of the incubation time before blistering for the three references of pre-treated self-crucible in contact with AKM (1100°C – pO2 =0.2 bar).

Influence of the temperature

Figure 84 compares the blistering phenomenon with a raw HZC refractory, at 1050°C and 1100°C, respectively. The results show that the incubation time is lower at 1100°C than at 1050°C: 14 hours at 1100°C and more than 35 hours at 1050°C. First of all, the ambipolar conductivity, and so, the permeation flux increases exponentially with temperature. The oxygen flux being noticeably higher at 1100°C, iron impurities within the refractory are oxidized more rapidly than at 1050°C. Consequently, the blistering phenomenon starts more rapidly. Obviously, as shown in Figure 84, the blistering is also more intense at high temperature.

As observed previously in equation (5), the higher the bubble size, the higher the rising rate. However, the glass properties play an important role in the blistering process, especially the glass viscosity which decreases exponentially with temperature [27, 157]. Consequently, the rising velocity of the bubbles increases when temperature increases, and the oxidation time of a refractory decreases as the temperature increases. In conclusion, the incubation time decreases while increasing the temperature.

The semipermeability set-up is a powerful method to observe the blistering at any time of the phenomenon especially at the beginning to compare the incubation time before blistering as a function of temperature.

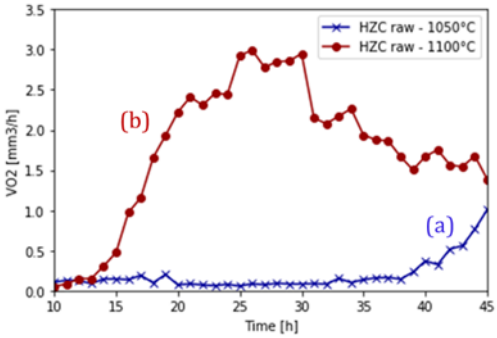

Figure 84: Semipermeability experiments to study the blistering of AKM glass in contact with a raw HZC in different temperature conditions: (a) blistering at 1050°C – pO_2 = 0.2 bar and (b) blistering at 1100°C – pO_2 = 0.2 bar.

As a reminder, the blistering is always triggered after a heating step under argon atmosphere, by changing the atmosphere in the lower part of the set-up from argon to air atmosphere (pO_2 = 0.2 bar). Indeed, the presence of O_2 atmosphere in the oxygen rich side of the set-up is activating the blistering mechanism. For this reason, the oxygen is put in contact with the refractory only when the temperature of the experiment is reached.

Another effect of the temperature is on the intensity of the blistering (Figure 84 and Figure 85). At 1200°C, the volume of O_2 calculated is hundred times higher than at 1100°C for HZC reference(Figure 85).

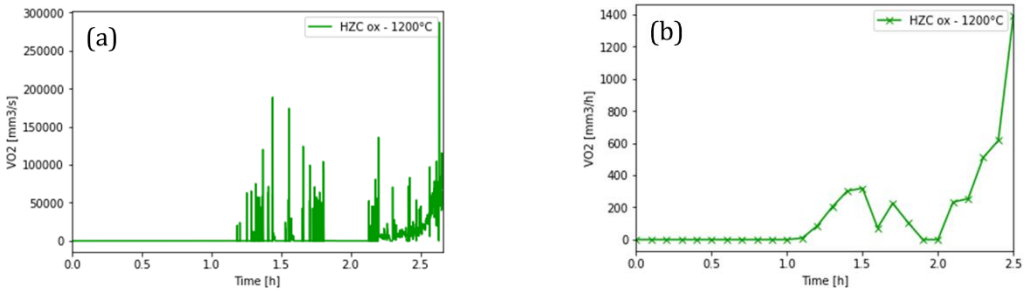

Figure 85: Semipermeability experiment to study, at 1200°C, the blistering of AKM glass in contact with an oxidized HZC-– pO_2 = 0.2 bar, (a) Oxygen peaks during blistering and (b) integration of the oxygen flux (in mm^3/h) as a function of time.

However, blistering projects glass on the walls of the crucible and of the alumina tubes due to the intense blistering phenomenon occurring under these conditions (Figure 86).

The blistering time at high temperature is then very short. Because of the high intensity of the blistering the glass quantity in contact with the refractory becomes very low and the interface composition could change very quickly, stopping the blistering phenomenon.

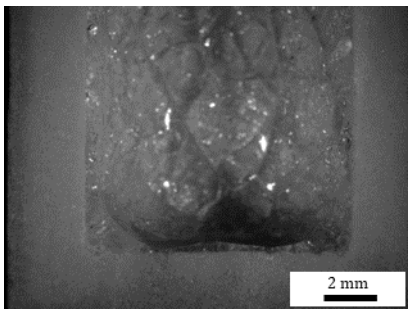

Figure 86: Post-mortem observation of self-crucible at the end of a semipermeability test (HZC oxidized tested at 1200°C under pO_2 = 0.2 bar) showing the low quantity of glass in contact with the bottom part of the self-crucible (Optical microscope x1).

Influence of the glass on the blistering

When the material is completely preoxidized, 2 hours are needed before the first bubble bursts at 1100°C. This incubation duration is the same for each reference since the oxidation step is completed, that is why it can be related to:

- the wetting time
- the bubble formation
- the bubble coalescence
- the time to rise to the surface
- the burst of the bubble releasing oxygen which is measured by the oxygen sensor

To visualize the blistering phenomenon, a sessile drop design was used [158]. A piece of glass on a refractory pellet is melted in a horizontal tubular resistance furnace. The vessel is a high-purity gas-tight alumina tube with water-cooled seals. An alumina holder, sliding inside the alumina tube, permits setting the sample in the centre of the furnace. The temperature of the sample is determined with a Pt-Pt (10 %) Rh thermocouple located under it. Two windows at each side of the tube allow the drop

to be illuminated and its shadow to be observed on a camera (monochrome camera BASLER CMOS 2/3 35i/s). An example of observation of bubble formation within a glass droplet at the interface with an oxidized refractory pellet is shown in Figure 87. Air was flowing inside the set-up around the glass drop. At the interface glass/refractory the oxygen activity is low. Consequently, an oxygen activity gradient is established between the centre of the drop and its periphery. The situation resembles the corrosion by differential aeration observed for a drop of water under air, placed on a steel plate: the oxidation occurs in the centre of the drop [159, 160]. The situation can also be compared to the semipermeability set-up shown in Figure 79. The photographs demonstrate that a bubble requires more than one hour to be formed at the glass/refractory interface and to rise till the height of glass in a semipermeability crucible refractory. This time can be compared to the incubation time observed with oxidized refractories.

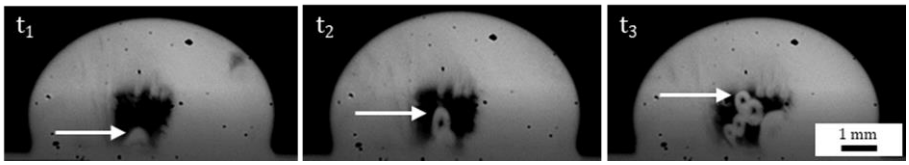

Figure 87: Bubble rise illustrating the incubation time at 1100°C under air atmosphere at a defined t_1 = 0 min, t_2 = 10 min, t_3 = 25 min.

The blistering tendency of a glass in contact with a refractory depends on the composition of the glass and of the refractory material. The first parameter used to compare the different references is the incubation time before blistering. It can be noticed that this time is different for two different glass references (Figure 88).

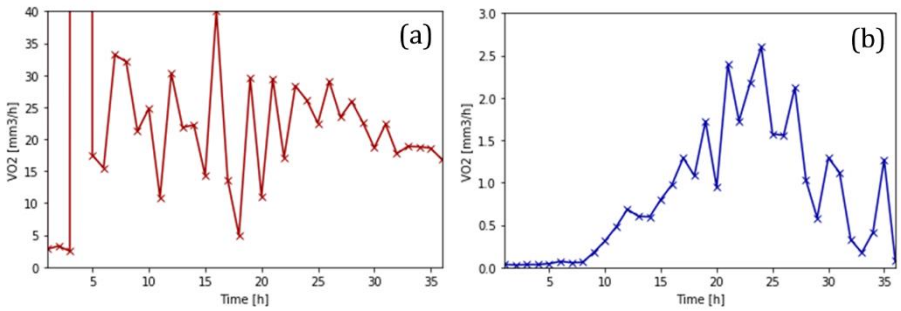

Figure 88: Comparison of the incubation time before blistering for an oxidized HZC refractory in contact with glasses with different iron contents (1100°C – pO_2 = 0.2 bar): (a) glass with low iron content, (b) glass with high iron content.

The glass viscosity decreases exponentially with temperature [157]. Consequently, the rising velocity of the bubbles increases when temperature increases, and the incubation time with an oxidized refractory decreases as the temperature increases. Obviously, the observed incubation time depends on the glass composition, especially on its redox state and iron content [20, 50, 56, 58]. The oxygen permeation flux is consumed by iron (Fe (II)) oxidation [31] till the Fe(II)/Fe(III) equilibrium is reached, delaying the blistering start, as shown in Figure 88. Blistering of the glass containing less iron oxides (Figure 88 (a)) is starting after 3 hours and for the one containing more iron oxides (Figure 88 (b)) it is only starting after 8 hours. The incubation time is longer in this case (Figure 88 (b)) than observed in Figure 81 (b), for the standard oxidized HZC refractory/glass combination, since a higher quantity of glass was put in contact with the refractory. *As the blistering intensity was increased it was necessary to maintain a continuously contact between the glass and the refractory interface.* Obviously, the incubation time before measuring the bubble burst also depends on the glass thickness which is three times higher than previous experiments.

Moreover, it should be noted that the blistering intensity is noticeably lower for a glass with the higher level of dissolved iron. An interpretation of this phenomenon could be given as schematized in Figure 89. The oxygen semipermeability flux is proportional to the oxygen activity gradient within the refractory. The oxygen solubility in the glass, $a_{O_2}(sat)$, depends on its iron content. As illustrated in Figure 89, the oxygen activity at saturation is higher with the glass containing the higher level of iron, reducing the oxygen activity gradient within the refractory. This variation of oxygen activity in the glass at saturation is probably insufficient to account for the noticeable lowering of the

blistering process. In case of a glass with a noticeable level of iron, a polarization phenomenon (leading to a lower pO_2 gradient) at the refractory/glass interface can, additionally, reduce the oxygen activity gradient within the refractory (see Figure 89), lowering the oxygen semipermeability flux and, consequently, the blistering will be less intense. This interpretation can be compared to that which was issued in the case of a gas/refractory/gas configuration.

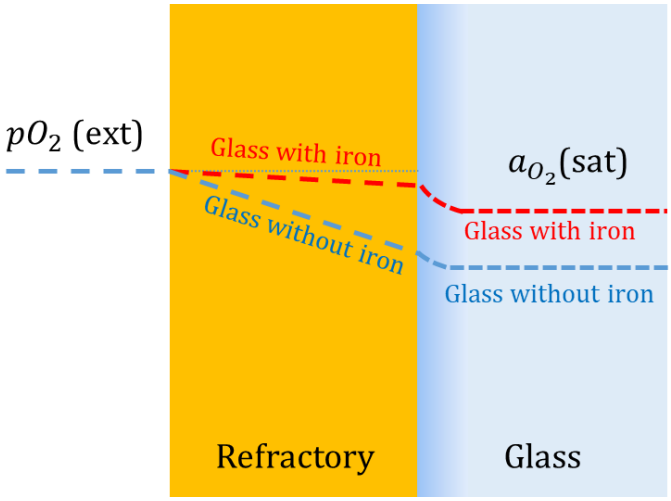

Figure 89: Illustration of the role of iron content in the glass melt on the blistering intensity.

Influence of the refractory composition on the blistering

By comparing several references of refractories under the same conditions (temperature, pO_2, glass viscosity), the influence of the oxidation regarding the reference studied is also observed. Indeed, the oxidation time is not the same for each raw refractory reference and it is well shown in Figure 90. As the blistering is due to a contact between the refractory and the glass, the refractory composition should also influence the blistering behaviour. Indeed, the incubation time is different for each reference when testing raw materials.

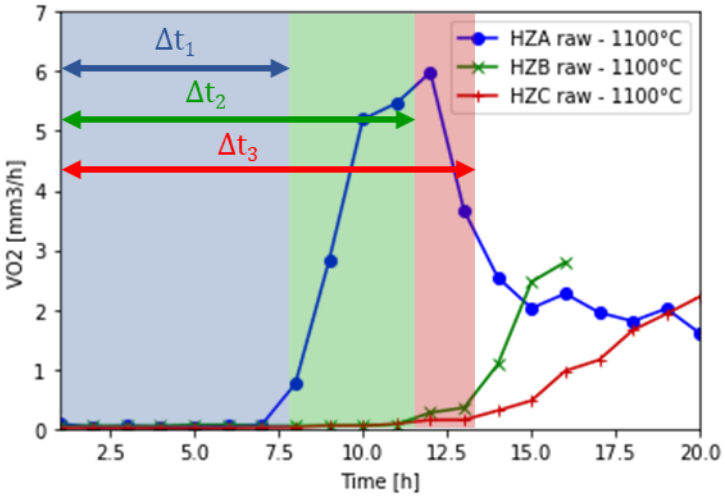

Figure 90: Comparison of the incubation time before blistering for the three references of raw self-crucible in contact with AKM (1100°C – pO_2 = 0.2 bar).

The blistering starts with HZA after 7 hours, with HZB after 11 hours and with HZC after 13 hours for raw references. The results are summarized in Table 12:

Table 12: Incubation duration for raw and oxidized materials before blistering (Uncertainty +/- 0.5 hour).

Incubation duration	**HZA**		**HZB**		**HZC**	
	Raw	Oxidized	Raw	Oxidized	Raw	Oxidized
1100°C – pO2 = 0.2	7h	2h	11h	2h	13h	2h

The duration before blistering depends on the oxidation time of each material. Indeed, each reference has different iron content at different redox levels, explaining why the blistering starts earlier with HZA than with HZB and HZC refractories. Regarding H_2 relaxed measurement after acid attack made in SGR Provence, the reduction degree is the highest for HZC, then HZB, and finally HZA (HZC > HZB > HZA). It is observed experimentally; the oxidation time is longer for HZC than HZA (HZC > HZB > HZA). Indeed, the flux for HZA is higher and the incubation period before blistering is shorter, because the macroscopic ambipolar conductivity of zirconia is clearly higher for HZA (transport in each grain + contacts) than for HZB and HZC. Unfortunately, it cannot be determined precisely.

Table 13 shows the relation between the zirconia content of the refractories (with more than 90 wt.% ZrO_2) and the blistering intensity. It should be noted that the higher the concentration of zirconia, the higher the blistering intensity (see Figure 90). The higher the temperature, the lower the incubation period and the higher the blistering intensity. For these undoped refractories, the minority carriers in the zirconia phase are oxygen vacancies, and the oxygen semipermeability flux is proportional to the oxygen vacancy conductivity. Consequently, it can be assumed that the higher the zirconia content, the higher the oxygen semipermeability flux (this is a general trend).

Table 13 : Blistering phenomenon vs. zirconia level of AKM in contact with various HZFC references tested below the zirconia phase transformation (1100°C – pO_2 = 0.2 bar). The plus signs are schematizing the foaming intensity, the more plus signs, the more intense.

Reference	ZrO_2	Foaming
HZA	94.1	+ + + +
HZB	93.9	+ + +
HZC	90.4	+ +

For various purposes, SEFPRO has developed refractories with doping zirconia either with Y_2O_3 or Ta_2O_5. Table 14 shows undoped HZFC, HZFC doped with Y_2O_3 and HZFC doped with Ta_2O_5. It should be noted that in contact with both doped materials, no blistering was observed at 1100°C, contrary to the undoped material.

Table 14: Role of doping on the blistering process of AKM in contact with various HZFC references tested below the zirconia phase transformation (1100°C – pO_2 = 0.2 bar).

Reference	ZrO_2	Ta_2O_5	Y_2O_3	Foaming
HZC	90.4			+ +
HZX	88.4	1.1		NO
HZS	86.9		0.51	NO

Various defect models have been proposed to explain the electrical properties of zirconia. The most recent experimental or theoretical works are using the anti-Frenkel structure initially proposed by Douglas and Wagner [161] expressed as (using Kröger-Vink notation):

$$O_O^{\times} = O_i^{"} + V_O^{\bullet\bullet} \qquad (39)$$

It has been demonstrated that the monoclinic phase of zirconia is a mixed ionic-electronic conductor, with predominant electronic conductivity [162, 163]. On the contrary, the tetragonal phase is an ionic conductor [164, 165]. A noticeable increase of the electrical conductivity is observed at the monoclinic-tetragonal transition. The transition is accomplished by a diffusionless mechanism in which some of the atoms move by distances less than one interatomic distance while other atoms nearly retain their original positions. The increase of the ionic conductivity can be ascribed to the high mobility of oxygen in the tetragonal structure [115, 166]. According to Weppner [125], the ionic mobility in tetragonal zirconia, under high oxygen partial pressure, is higher than one order of magnitude compared with calcia stabilized zirconia, and the electron hole conductivity is slightly higher. Although tetragonal zirconia is thermodynamically stable above the transition temperature, it can be stabilized at much lower temperatures by stresses, doping or reducing the crystallite size [167, 168].

The equilibrium with the oxygen partial pressure can be written:

$$\frac{1}{2} O_2 + V_O^{\bullet\bullet} = O_O^{\times} + h^{\bullet} \qquad (40)$$

or

$$\frac{1}{2} O_2 = O_i^{"} + h^{\bullet} \qquad (41)$$

For pure zirconia, the defects concentrations, both oxygen interstitials and electron holes increase with oxygen partial pressure. The ionic conductivity can be modulated by doping with oxides, either a dopant with a valence lower than 4 (such as CaO or Y_2O_3) or a dopant with a valence higher than 4 (such as Ta_2O_5) [169]. According to reaction (41), under high oxygen partial pressure, the majority ionic defects in pure zirconia are oxygen interstitials, $O_i^{"}$. The doping reaction with Y_2O_3 under high oxygen partial pressure can be written:

$$Y_2O_3 + O_i^{"} \rightarrow 2\,Y_{Zr}' + 4\,O_O^{\times} \qquad (42)$$

Consequently, with low yttria level (of the order of 0.2 wt.% as measured in HZFC products), the intrinsic oxygen interstitial can be consumed by the doping, inducing a

lowering of the ionic conductivity. This feature has been observed by Nashrallah and Douglass [134]: for 1 mol.% yttria, at 900°C, a decrease of the ionic conductivity has been observed.

Obviously, for noticeable doping, the reaction has to be written:

$$Y_2O_3 \;=\; 2\,Y'_{Zr} \;+\; 3\,O_O^{\times} \;+\; V_O^{\bullet\bullet} \qquad (43)$$

leading to an increase of the oxygen vacancy concentration and a noticeable increase of the ionic conductivity, owing to the higher mobility of oxygen vacancies compared with oxygen interstitials [130].

Doping zirconia with tantalum has the opposite effect. Doping compounds with a valence higher than 4 induces a reduction in oxygen vacancies, according to:

$$Ta_2O_5 + V_O^{\bullet\bullet} = 2\,Ta_{Zr}^{\bullet} \;+\; 5\,O_O^{X} \qquad (44)$$

Consequently, the ionic conductivity of the HZFC refractory decreases significantly. Because, the minority carriers are oxygen vacancies, doping with tantalum will reduce noticeably the oxygen semipermeability flux and as a result the blistering process, as shown in Table 14.

These results demonstrate that, by appropriate doping of the refractory, the blistering can be strongly reduced or even canceled.

A variation on the zirconia content was tested in different conditions during this project (oxidation state, atmosphere, temperature, glass in contact), to study the relation between the zirconia content in HZFC and the blistering abilities as summarized in Table 15 for references containing Na_2O and Table 16 for references containing B_2O_3 and some residual Na_2O.

Table 15: Summary of blistering phenomenon of AKM in contact with various HZFC references containing Na_2O in their composition in wt.% (1100°C – pO_2 = 0.2 bar).

Reference	ZrO_2	SiO_2	Al_2O_3	Na_2O	B_2O_3	Foaming 1100°C?
HZA	96	2.2	0.7	0.1		YES
F2590-2	91.3	5.1	2.1	0.3		YES
F2590-3	86.6	9.0	2.7	0.6		YES
F2590-4	83.2	11.3	3.4	0.7		NO
F2590-5	76.7	16.7	5.0	1.1		NO

Table 16: Summary of blistering phenomenon of AKM in contact with various HZFC references containing B_2O_3 in their composition in wt.% (1100°C – pO_2 = 0.2 bar).

Reference	ZrO_2	SiO_2	Al_2O_3	Na_2O	B_2O_3	Foaming 1100°C?
HZB	93.8	4.8	0.6		0.6	YES
HZC	90.4	8.0	0.6		0.7	YES
F2603-3	86	10.2	3.1	0.1	0.5	YES
F2603-1	82	13.1	4.4	0.1	0.5	NO

The main observation of blistering tests is: the higher the level of zirconia in a refractory, the more blistering abilities (Figure 91). There is a threshold between 80 wt.% and 84 wt.% ZrO_2 under which materials are not leading to blistering at 1100°C (or at 1250°C). This threshold depends on the nature of the vitreous phase.

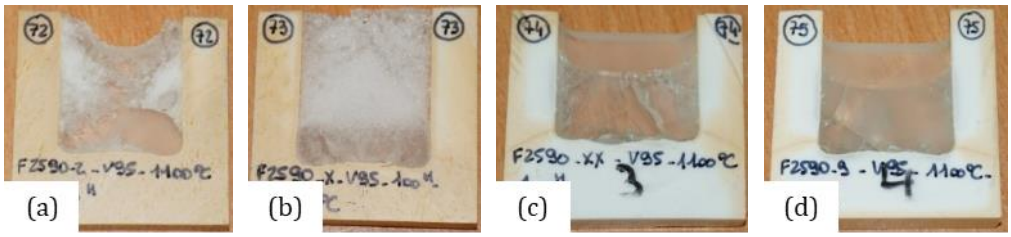

Figure 91: Post-mortem observation of self-crucible after semipermeability tests showing the aptitude for blistering for (a) 91.3 wt.%, (b) 86.6 wt.%, (c) 83.2 wt.% and (d) 76.7 wt.% ZrO_2.

Estimation of oxygen activity at the lean side

Following ambipolar conductivity values obtained in Chapter 3 and the oxygen flux measured in Chapter 4, it is possible to calculate theoretically the oxygen activity at the lean side interface using the following equation [170]:

$$J_{O_2} = \frac{RT\,\sigma_{amb}}{16\,F^2\,L} \ln \frac{P_{O_2}^{rich}}{P_{O_2}^{lean}} \qquad (45)$$

It must be reminded that this calculation only considers the transport phenomenon (Wagner's theory). The effect of the edges and of the glass, inducing fluctuations, in the results are here neglected. These results must therefore be seen in a semi-quantitative way.

At the oxygen lean side interface, in contact with glass, the formation of an oxygen bubble requires that the internal pressure is equal to 1 bar. That is why it can be expected from the lean side pO_2 values to be high. Pressure in the region of 0.2 bar is indeed observed in Table 17 which is presenting the values of pO_2 at the lean side according to equation (43), at the glass/refractory interface, at 1100°C.

Extra-clear glass in contact with HZC has the lowest calculated pO_2 leading to the most intense blistering as explained previously. The oxygen flux released during the blistering is indeed less consequent for AKM glass in contact with HZC and the pO_2 calculated is higher. Even if these results must be taken in a semi-quantitative manner because of the approximations made (see electrical part and Wagner's theory, Section III.3.2.), the trend is clearly in the right direction. The higher the pO_2 gradient, the more intense the blistering.

Table 17: Calculated pO_2 at the lean side at the glass/refractory interface at 1100°C ($pO_{2,rich}$ = 0.2 bar).

Reference	σ_{amb} (Ω^{-1}.cm^{-1})	J_{O_2} (mol/cm²/s)	pO_2 lean (bar)	Glass	Blistering intensity
HZC	2.5E-04	6.9E-12	0.197	AKM	+
HZC	2.5E-04	3.2E-10	0.110	Extra-clear	++++

IV.2.3 External polarization

It was demonstrated in the previous section that the blistering phenomenon is ascribed to oxygen transport through the zirconia phase of the refractory. To confirm this feature, the semipermeability set-up was modified for applying external polarization through the refractory. The objective was to demonstrated that, by transferring oxygen through the membrane by external polarisation ("pumping mode" of the cell as discussed in Section III.3.2), it is possible either to increase the blistering intensity or to switch off the phenomenon.

Two platinum grids were added as described in Figure 92. These platinum grids are directly in contact with the studied refractory crucible, at the air interface and at the glass interface. The bottom grid was fixed using the same platinum lacquer as used in the complex impedance sample preparation. Furthermore, two platinum wires are in contact with these platinum grids. They are connected to a generator in order to impose a voltage between these two electrodes.

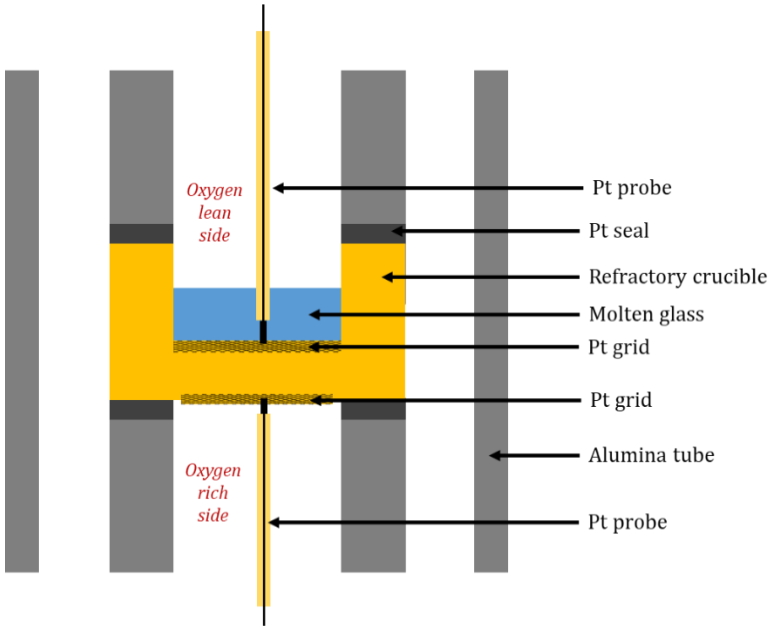

Figure 92: Semipermeability set-up containing platinum grids at the air contact and glass contact to perform a polarization through the refractory.

Using this set-up, it is therefore possible to polarize the refractory (anodic or cathodic polarization). At the cathodic side (either the refractory/air or the glass/refractory

interface), oxygen is reduced, lowering the oxygen activity at the interface, according to:

$$\frac{1}{2}O_2 + 2\,e^- \rightarrow O^{2-}_{zirconia} \qquad (46)$$

At the anodic side, the reverse reaction takes place, with production of gaseous oxygen:

$$O^{2-}_{zirconia} \rightarrow \frac{1}{2}O_2 + 2\,e^- \qquad (47)$$

The situation differs according to the electrochemical polarization mode: "galvanostatic" mode (monitored current intensity) or "potentiometric" mode (monitored cell voltage).

In case of a *galvanostatic mode*, on the cathodic part of the crucible, it is necessary to consider the maximum adsorption flux of oxygen, fixed by the gas or the oxygen activity in the glass. The adsorption flux corresponds to I_{lim}, a limiting cathodic current. Applying this current, the oxygen activity is null. The I_{lim} value depends on the oxygen activity or oxygen partial pressure at the cathodic side. According to the applied current intensity (absolute value), two situations are found [171]:

- If the absolute value of the cathodic current is lower than $|I_{lim}|$, no stoichiometry change of the electrolyte is observed and the same mechanism as an oxygen pump is encountered. There is only an oxide ions flux from the cathode to the anode following Faraday's law $J = \frac{I}{2F}$ as presented in Figure 93 (a).
- If the cathodic current is higher than $|I_{lim}|$, the current is defined as $I = I_{lim} + I_e$, where I_e corresponds to the injection of trapped electrons on the point defects or impurities (oxygen vacancies, iron impurity, etc.) as presented in Figure 93 (b).

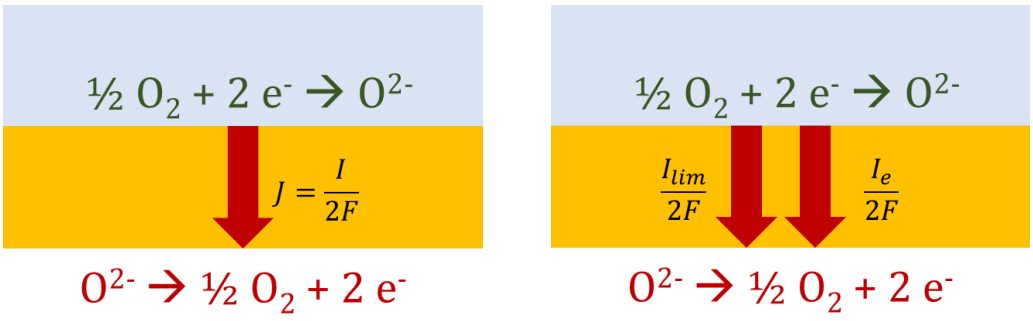

(a) (b)

Figure 93: Representation of a cathode polarization process (at the glass side).

In case of a *potentiostatic mode*, it is theoretically possible to control the cathodic reaction and to avoid electrochemical reduction of the electrolyte. If we consider a redox couple within zirconia, such as $V_O^{\bullet\bullet}/V_O^{\bullet}$ for which the thermodynamic potential is ca. -1.5 V/air [172], if the applied voltage is higher than -1.5 V/air, then the electrolyte cannot be reduced and the maximum of the current value will be $|I_{lim}|$. Consequently, to avoid zirconia reduction the applied voltage was higher than - 1.5 V/Air. However, iron impurities are present in the studied refractories, and it has been shown previously that for an applied potential of ca. -1 V/air iron species can be reduced into metallic iron [173]. Using a two-electrode cell, the applied voltage U is:

$$U = E_{th} + R\,I + \eta_{anod} - \eta_{cathod} \qquad (48)$$

Where R is the resistance of the cell, I the current, E_{th} the thermodynamic potential of the cell at zero current, η_{anod} and η_{cathod} are the anodic and cathodic polarizations.

Even at high temperature, the term ($R\,I + \eta_{anod} - \eta_{cathod}$) is noticeably higher than E_{th} (often a few tens volts), and it is experimentally very difficult to ascertain that the applied voltage avoids electrolyte reduction.

By polarization, it is possible to cause the start or the end of the blistering phenomenon. A polarization experiment was performed in order to stop the blistering of glass in contact with the refractory, after it was processed at 1100°C (pO_2 = 0.2 bar). The blistering was started following the same protocol as the other experiments described previously. The difference lies in the configuration of the set-up. In order to stop the blistering, a cathodic polarization is necessary (the “minus” on the glass side and the “plus” on the air side).

Owing to the difficulties presented before, the oxygen semipermeability flux in the experimental conditions was evaluated first and the corresponding current was calculated, to switch off the blistering phenomenon. Then, a cathodic current, higher than this value, was applied and the oxygen concentration in flowing argon was recorded continuously according to the procedure described previously. After interrupting the current, the open-circuit voltage was measured to verify that the zirconia phase was not reduced.

At 1100°C, with pO_2 = 0.2 bar at the extrados, the blistering started as a standard blistering test and oxygen semipermeability flux for HZC was estimated to 5 mm^3/h, or J = $1.4x10^{-3}$ mm^3/s of oxygen. According to the Faraday law, the current I corresponding to this oxygen flux is:

$$I = \frac{4\,F\,J}{t_i\,V_M} \qquad (49)$$

where t_i is the ionic transport number of the zirconia phase (t_i was estimated to 0.2, see Table 9), F the Faraday constant and V_M the molar volume of oxygen.

In these conditions, the current I was evaluated to 0.12 mA and a current of 2 mA was applied at t = 72 h during 2 hours. The experimental results are given in Figure 94. The blistering is temporarily increased because of the current flowing in the Pt grid causing the bubbles therein to detach. A decrease in the concentration of bubbles exploding on the glass surface after the first polarization can directly be observed. Bubbles detached by the polarization of the platinum grid collapsed together and the majority of the bubbles present in the thickness of the glass rose rapidly to the glass surface because of the size of the bubbles produced. As bubbles accumulate rapidly together, the size is larger and they rise at high velocity. For a standard blistering, emf values around -150 mV (140 O_2 ppm) are observed with the oxygen sensor, whereas the blistering induced by the polarization produce an intense blistering showing emf values till -50 mV (18 000 O_2 ppm). Once all the bubbles have risen, a sudden stop of the blistering is observed since all the bubbles present before polarization may have risen again and burst.

The ratio between standard blistering and blistering generated by polarization is about 130. Making the hypothesis that a single bubble bursts after the polarization, the bubble rises 25 times more rapidly when generated by polarization, it means in 4

minutes compared to 90 minutes in a standard blistering. That is why the blistering linked to the polarization is so intense and brief.

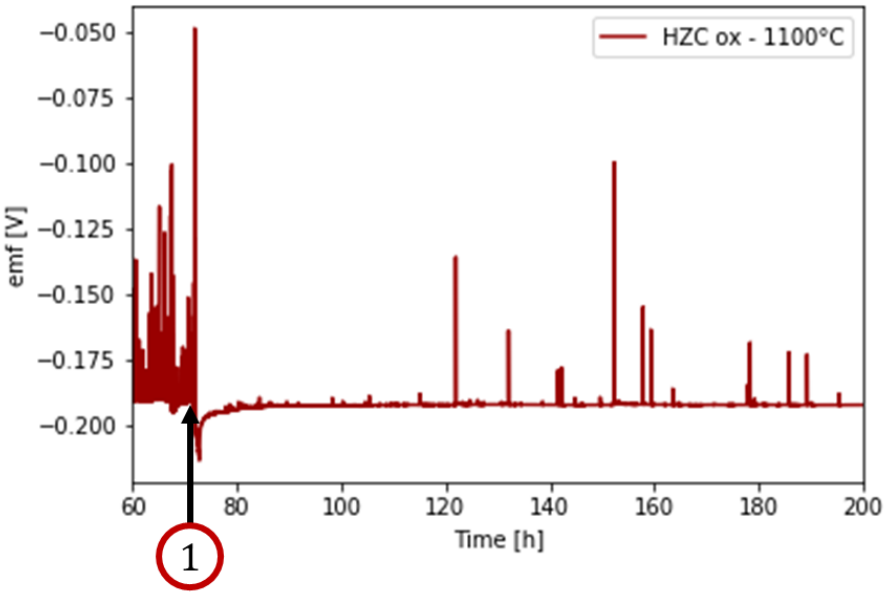

Figure 94: Semipermeability experiment (1100°C – pO_2 = 0.2) with cathodic polarization during 2 hours starting after a standard blistering at t = 72 h (1). End of the blistering is directly observed. The blistering is starting again at t = 122 h.

Blistering starts again after a certain time since the material was completely reduced at the cathodic interface following the polarization. It is therefore necessary to oxidize again the glass/refractory interface. The blistering, less intense than before the onset of polarization, was still able to resume around t = 120 h (Figure 94). As the potential applied is lower than 1.5 V, zirconia is not reduced during the experiment. Only iron oxide is reduced in the refractory and the flow of semipermeation must oxidize it again before the blistering could start again. The blistering observed after a long polarization is lower in intensity, as the material was reduced, the interface modification is responsible of this decrease in intensity.

IV.2.4 Microstructure of the zirconia

Zirconia microstructure is a critical parameter for the semipermeability phenomenon. Percolation and tortuosity of this crystallized phase should have an

impact in the blistering mechanism, enhancing or limiting the semipermeability paths from the oxygen rich side to the glass/refractory interface. However, looking at a HZC reference with 90 wt.% ZrO_2 and a F2590-5 refractory with 76 wt.% ZrO_2, it is very likely that the zirconia crystals are percolating in both cases. The global microstructure like the zirconia dispersion and so the tortuosity should therefore differ.

The zirconia microstructure was studied by tomography measurements (Figure 95). Visually speaking, it is observed that the HZC material (Figure 95 (a)) contains less vitreous phase in the global matrix that the F2590-5 material (Figure 95 (b)). Indeed, the zirconia grains are well distributed in the refractory containing 90 wt.% zirconia (HZC). However, accumulation of vitreous phase is observed in the refractory containing 76 wt.% zirconia (F2590-5), leading to zirconia dendrites through the whole thickness of the studied refractory.

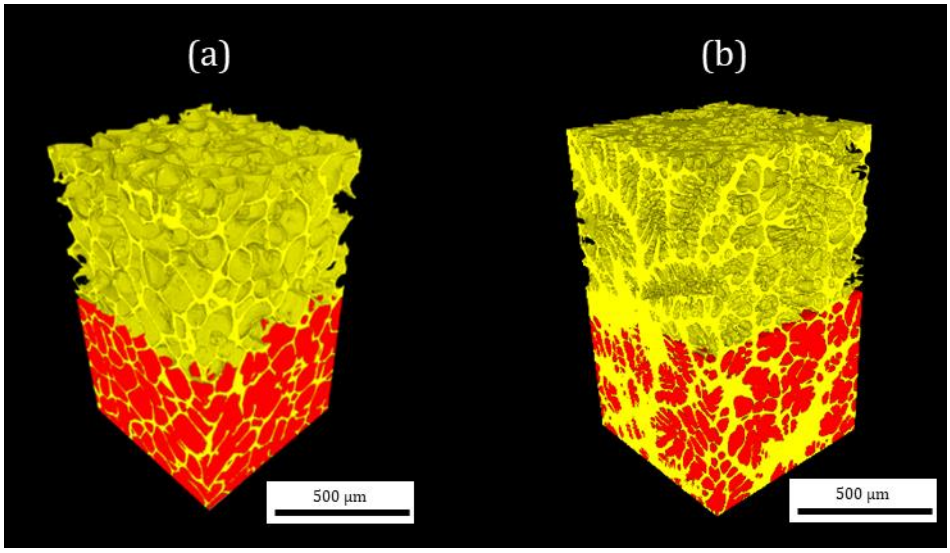

Figure 95: Influence of zirconia content on the percolation of a sample with 1 mm diameter: (a) 90 wt.% vs (b) 76 wt.% ZrO_2 right ZrO_2 (zirconia grains in red and glassy phase in yellow).

Two measurements were performed. One with a sample of 1 mm diameter with a 1 µm resolution as presented in Figure 95, one with a sample of 2 mm diameter with a 2 µm resolution. Indeed, while studying the sample of 1 mm diameter, percolation of the zirconia phase was observed through the whole thickness. By studying the influence of the resolution, the change in voxel size between 1 µm and 2 µm does not lead to a critical loss of information. Percolation of the zirconia phase was still observed. However, glassy phases are sometimes finer than 1 µm and so zirconia contacts could

still take place on a finer scale. The conclusions presented in this study are therefore dependent on the resolution used. The percolation study is indeed incomplete and should be studied at higher resolution. Nevertheless, by studying these materials at higher resolution the representative elementary volume (REV) is not reached anymore since the measured volume is too small.

The tortuosity of both references was studied since the percolation is observed in both cases. Difference in tortuosity value for HZC and F2590-5 are presented in Figure 96. A stable value from a certain REV is shown. This stable value is almost 1.5 times higher for F2590-5 than for HZC refractory. Even if both materials contain a percolating zirconia, zirconia microstructure and so its tortuosity value play a significant role in the blistering mechanism.

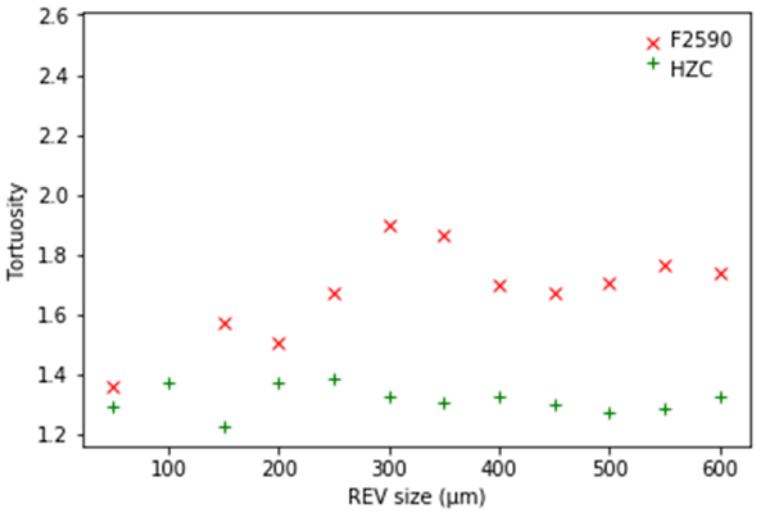

Figure 96: Tortuosity values from HZC and F2590-5 obtained after X-ray tomography measurements in SIMAP, Grenoble. The tortuosity values were obtained by L. Salvo.

According to the following observations, the vitreous phase blocks the zirconia path from the surrounding atmosphere to the refractory/glass interface leading to the blocking of the blistering phenomenon. In order for blistering to occur, oxygen ions must be able to be efficiently transported from the outside atmosphere to the interface with the glass. To do so, an important parameter must be satisfied: a high percolation and a low tortuosity of the zirconia grains. These parameters are obtained from a certain percentage of zirconia and can vary with the composition. As a conclusion, if the zirconia is undoped and highly percolating with a low tortuosity, the ambipolar

conductivity is managing the blistering/foaming, on the other hand if the zirconia is non-percolating or doped then no blistering can appear.

Furthermore, while observing the glass/refractory interfaces, blistering is always observed above the area where the zirconia grains are percolating. Whereas, no blistering is observed above the area where the vitreous phase is completely surrounding the zirconia structure. Figure 97 is an illustration of the link between zirconia percolation and blistering phenomenon.

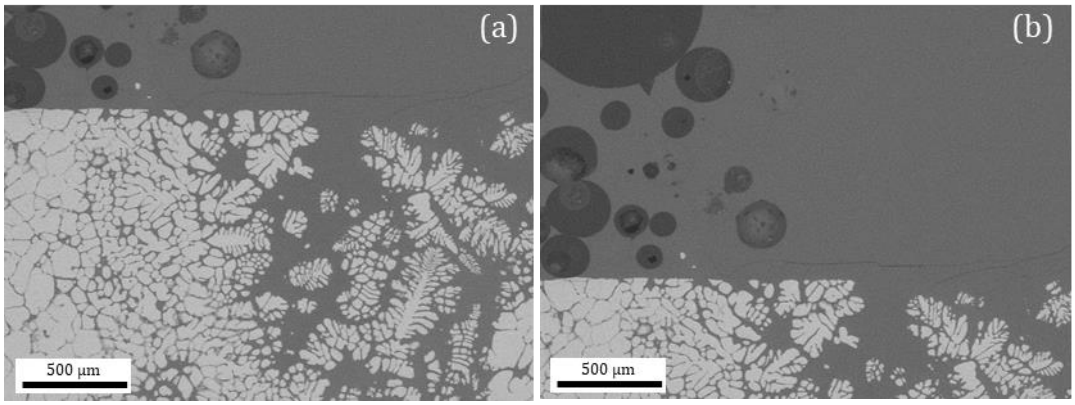

Figure 97: Post-mortem SEM observation for a HZC tested in semipermeability set-up at 1100°C under pO_2=0.2 bar showing two different behaviours, whether the zirconia is percolating (left) or not (right).

Another observation going in the direction of the importance of the zirconia percolation is showed Figure 98. Indeed, the zirconia grains in the case of HZC (Figure 98 (a)) are less surrounded by the vitreous phase than the zirconia grains in the case of F2590-5 (Figure 98 (b)).

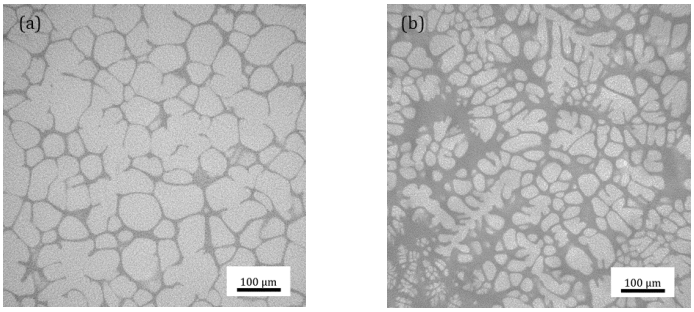

Figure 98: Microstructural observation for (a) raw HZC and (b) raw F2590-5.

As a reminder, F2590-5 does not lead to blistering whereas HZC does. It should mean that no path can be found from the surrounding atmosphere till the glass/refractory interface when the material is not blistering.

As already explained, the transport is not directly influenced by the vitreous phase. Only indirectly since it modifies the zirconia network and therefore will have an importance in the flow through the refractory. Indeed, a higher vitreous phase rate will decrease the percolation rate and increase the tortuosity of the zirconia phase. Moreover, the nature of the vitreous phase could increase the percolation rate and the tortuosity rate of the zirconia structure, enhancing the transport through the zirconia.

IV.2.5 Microstructural changes during blistering

Once the blistering parameters have been studied, the stop of the highlighted blistering should also be understood. As already observed in semipermeability tests presented previously, the blistering of HZFC materials has a start but also an end when the time of the experimentation is consequent. This feature has been observed for every reference tested in semipermeability set-up as shown in Figure 99.

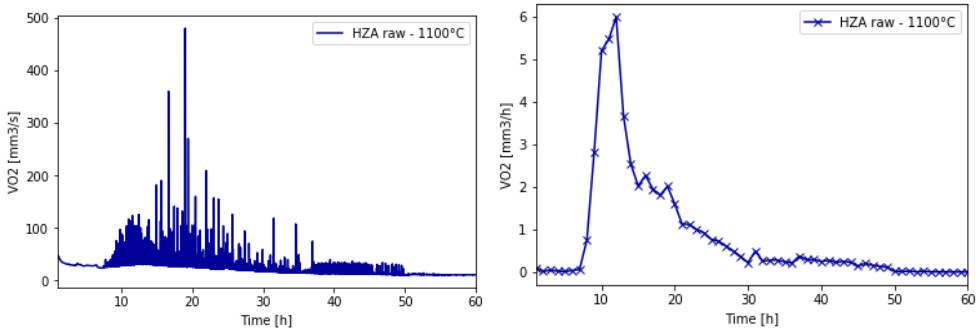

Figure 99: Beginning and end of the blistering phenomenon of raw HZA in contact with AKM at 1100°C – pO2=0.2 bar.

The shutdown of the phenomenon is complex and the modification of the glass/refractory interface is probably concerned. A characterization of the interface was initiated to find some of the main key parameters influencing the decrease of the blistering phenomenon.

This stop can be explained by changes in the chemistry of the glass or of the glass/refractory interface, which lead to a modification of the oxygen activity of the interface that may become equal to that in contact with the external atmosphere and the driving force of the semi-permeability being disrupted. Another reason for the shutdown is a blocking of the O^{2-} flux, which may be due to the formation of an insulating layer around the ZrO_2 grains or at the glass/refractory interface as presented in Figure 100, where zircon formation is observed around zirconia grains and predominantly at the glass/refractory interface.

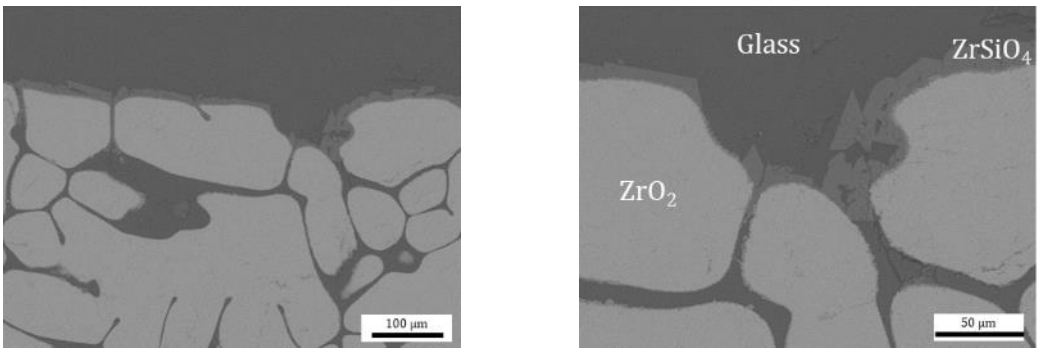

Figure 100: Post-mortem SEM observation for a HZC preoxidized 30h at 1350°C, tested in semipermeability set-up at 1100°C under pO_2=0.2 bar that stopped blistering.

Zircon blocks the blistering phenomenon like the vitreous phase (Figure 97) when no zirconia is in contact anymore with the glass at the interface, or when zirconia grains are not in contact anymore. Indeed, the zirconia grains end up surrounded by a layer of zircon preventing percolation and contact at the close interface with the glass and therefore the transport of oxygen. This phenomenon stops the blistering. According to these observations, it confirms the hypothesis detailed previously: if the zirconia path from the surrounding atmosphere to the glass/refractory interface is not complete the blistering should not occur. Indeed, no zircon formation is observed around zirconia grains when blistering is still occurring in glass in contact with the refractory (Figure 101). This phenomenon was observed after each experiment: sufficient zircon formation surrounding zirconia grains is only observed when the blistering stopped.

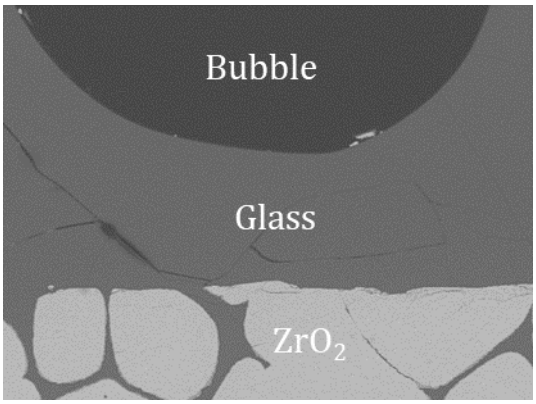

Figure 101: Post-mortem SEM observation for a HZC preoxidized 30h at 1350°C, tested in semipermeability set-up at 1100°C under pO_2=0.2 bar stopped before the end of the blistering.

The thermal treatment could lead to zircon formation as seen on Figure 102. By comparing the ratio of the peaks $ZrSiO_4/ZrO_2$, HZC oxidized 720h at 1350°C has 9 times more zircon than HZC oxidized 30h at 1350°C. Zircon formation in HZFC is dependent on time and temperature.

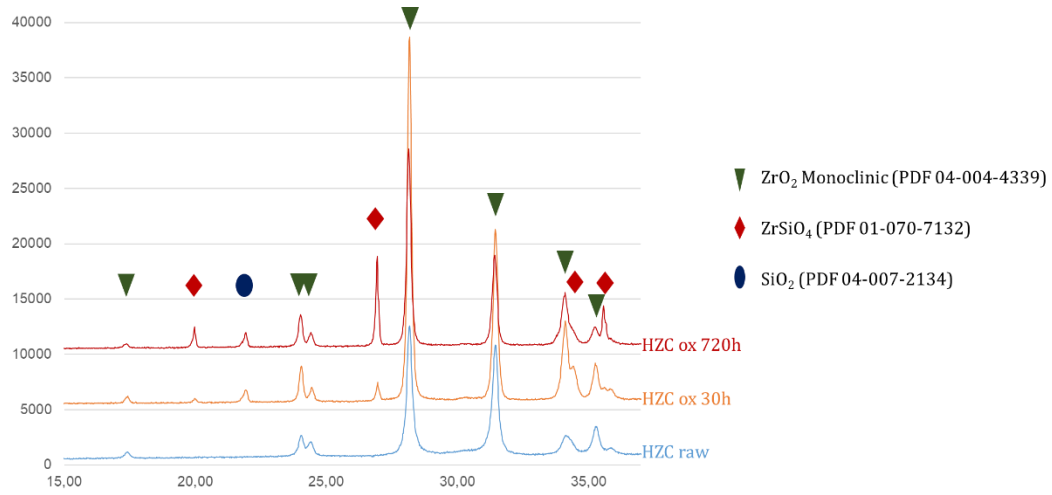

Figure 102: XRD measurements showing the formation of zircon for different time of oxidation.

Moreover, the zircon formation is enhanced at the glass interface, because it is the place where SiO_2 enhances the following reaction: $SiO_2 + ZrO_2 \rightarrow ZrSiO_4$.

It was also observed that the chemical reactivity between glass and refractory impedes the phenomenon of semipermeability and therefore blistering. Indeed, if the glass is in contact with the refractory during a long time under argon atmosphere, no blistering is observed while putting the self-crucible containing the glass under air atmosphere. It

means that the blistering is dependent on the thermal history of the refractory/glass combination since a modification of the interface is stopping the blistering. In the proposed scenario, a change in the composition of the glass phase in contact with the refractory was not considered, because this phenomenon only affects the end of the blistering process.

To understand better the influence of the glass/refractory interface, a preliminary study on the interface was made with microprobe measurements (WDS). Indeed, SEM observations were not sufficient to conclude about the influence of the glassy phase or glass composition on the phenomenon. Microprobe measurements were performed to obtain a chemical diffusion profile from the glass to the inner part of the vitreous phase of the refractory, with a special attention to the composition of the interface.

Microprobe profiles of the chemical variation of several elements present in glass and in the glassy phase of the refractory were studied and some of them are presented in the following graphs. The profile was starting in the glass (-200 µm to 0 µm) and is going into the refractory (0 µm to 2000 µm), with the composition measured at the interface at 0 µm. In the refractory, the measurements are performed in the vitreous phase. The aim was to understand the interdiffusion between the glass and the refractory, especially the vitreous phase.

The best tracer of the glass diffusion into the vitreous phase of the refractory material is MgO. Indeed, no MgO is present in the initial composition of the refractories studied. MgO diffusion is well observed in the case of both raw and oxidized HZC after a semipermeability test at 1100°C under $pO_2 = 0.2$ during 140 hours (Figure 103). However, no diffusion of glass component is highlighted in HZS and HZSY, which did not lead to glass blistering after 140 hours at 1100°C under $pO_2 = 0.2$ bar. It is interesting to note that MgO increases the viscosity of the glass. In the case of HZC, a continuous penetration is observed, showing a low gradient in concentration. However, for the references that are not leading to blistering, a sharp gradient in concentration is observed between the glass and the glassy phase, indicating neither chemical reaction nor exchange.

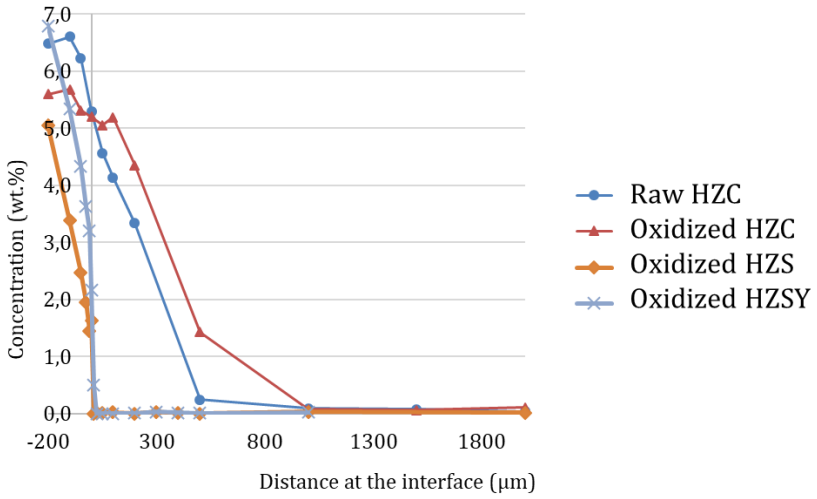

Figure 103: MgO diffusion profile from the glass to the refractory bulk performed on self-crucibles tested in the semipermeability set-up (1100°C under pO_2 = 0.2 bar during 140 hours). Glass from -200 µm to 0 µm, interface at 0 µm and refractory vitreous phase from 0 µm to 2000 µm. The initial vitreous phase composition is observed at 2000 µm.

For HZS and HZSY, a sharp decrease at the interface followed by an important increase of Al_2O_3 concentration in the vitreous phase at the near environment of the interface to reach the initial composition of the material is noticed in Figure 104. It shows no exchange between glass and refractory for these references. It should be noticed that an increase in Al_2O_3 content increases the viscosity and the surface tension at the glass/refractory interface.

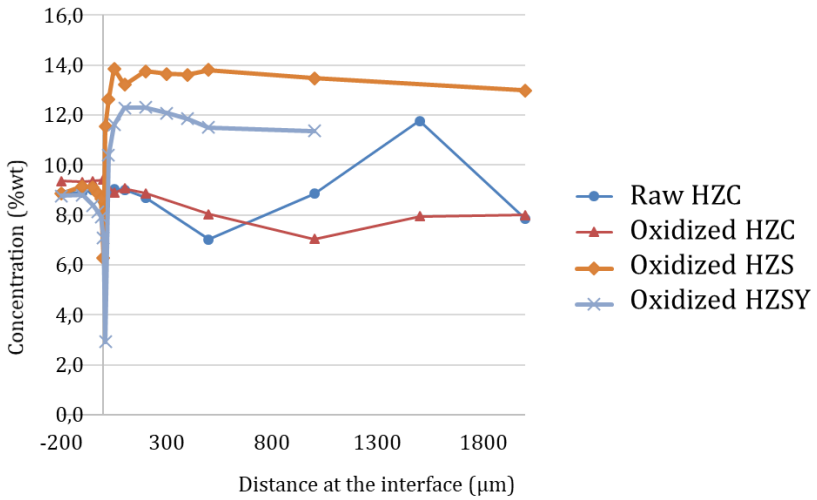

Figure 104: Al_2O_3 diffusion profile from the glass to the refractory bulk performed on self-crucibles tested in the semipermeability set-up (1100°C under pO_2 = 0.2 bar during 140 hours). Glass from -200 µm to 0 µm, interface at 0 µm and refractory vitreous phase from 0 µm to 2000 µm. The initial vitreous phase composition is observed at 2000 µm.

As highlighted in the microprobe measurements, diffusion process occurs between glass and refractory but only for references leading to blistering (raw HZC and oxidized HZC). These results confirm the influence of the interface in the blistering parameters either by zircon formation or by the presence or not of a diffusion phenomenon between the vitreous phase and the glass which could prevent or cut off the blistering. Interesting results were obtained with microprobe measurements but they are insufficient to fully describe the end of the blistering. The solubility of oxygen is another important point to study in the future, but mainly within the new interface layer created by the contact between zirconia/vitreous phase/glass and not throughout the whole thickness of the glass.

Chapter V: **Scenario**

The aim of the thesis was to build a scenario to explain the blistering phenomenon of silica-soda-lime glasses in contact with fused-cast high zirconia refractories. As recalled in Chapter 1, at the beginning of this work many experiments had been carried out in the Saint-Gobain Research Centres in Cavaillon, Paris and Northborough. However, a complete interpretation of the results was missing and the only consistent model available, i.e., the Baucke's interpretation, was not consistent with all these results. It should be pointed out that the Baucke's model, published in 1988, only concerns zircon refractories. However, it was demonstrated in Chapter 1 that the hypotheses, on which the Baucke's model is based, are questionable regarding our results.

As reported in Chapters 3 and 4, we carried out original experiments, in addition to the one previously reported in Saint-Gobain's reports. In this Chapter, a blistering scenario at the glass/dense fused-cast refractories interface is elaborated.

V.1 FUSED-CAST REFRACTORIES

The main results reported in Chapters 3 and 4 are the following:

- Bubbles generated at the glass/refractory interface are not caused by physical permeability since the materials studied are very dense with a negligible open porosity.
- In this work, bubbles created by the interaction between glass and refractory are only composed of oxygen.
- No intense and permanent oxygen blistering is observed if the outside atmosphere is neutral (argon, nitrogen).
- It has been demonstrated that the blistering occurs either below the phase transition temperature of zirconia or above (monoclinic → quadratic at about 1150°C).

- The refractory must be completely oxidized for the intense and permanent blistering to take place. A refractory material is "oxidized" when the iron impurities present are oxidized, i.e., all the metallic iron nodules have to be transformed either in Fe(II) or Fe(III) ions to reach the equilibrium Fe(II)/Fe(III) ratio. If no iron impurities are in presence, the blistering takes place immediately because no oxidation step is needed.
- A glass containing a high Fe(II)/Fe(III) level also have a buffering effect on the blistering. Oxygen solubility in the glass is increased, inducing both a delaying of the blistering start and a noticeable lowering of the blistering intensity. Increasing the amount of iron in the glass also increases the solubility of oxygen (i.e., the maximum amount of oxygen that can be absorbed). If the Fe(II)/Fe(III) equilibrium is not reached, a buffering effect is possible.
- The oxygen flux through the refractory is ascribed to a semipermeability flux. It should be recalled that in absence of glass, oxygen does not desorb at the lean side inducing a polarization phenomenon and, consequently no oxygen flux is observed.
- The occurrence of an oxygen semipermeability flux requires that the oxidized refractory is a mixed ionic-electronic conductor. The vitreous phase being an ionic conductor, the flux involves only the zirconia phase network.
- The preponderant role of zirconia was demonstrated: the higher the level of zirconia in a refractory, the more intense the blistering. The percolation of the zirconia grains to ensure the transport of oxygen through the refractory wall is necessary. As demonstrated by tomography analysis, zirconia microstructure depends on the zirconia content and vitreous phase composition.

The blistering phenomenon at high temperature has been ascribed in the literature to a “redox shock” between the refractory and the glass (48). This phenomenon would result from a significant difference in redox state between the glass and the vitreous phase of the refractory. Indeed, a raw refractory contains metallic iron so sodium sulphate may be reduced to form SO_2 bubbles, according to the following reaction:

$$Na_2SO_{4,glass} + Fe_{refractory} \rightarrow SO_{2,glass} + FeO_{refractory} + Na_2O_{glass} \quad (50)$$

The blistering phenomenon can also be ascribed to the "reboil" phenomenon. The fining process for the glasses tested was carried out using sodium sulfate (Na_2SO_4). Consequently, according to reaction (49), the fining reaction induces the formation of SO_2 bubbles, and no formation of oxygen bubbles:

$$Na_2SO_{4,glass} + 2FeO_{glass} \rightarrow SO_{2,glass} + Fe_2O_{3,glass} + Na_2O_{glass} \quad (51)$$

The redox shock phenomenon was quantified by coupling the semipermeability set-up with a mass-spectrometer for analysing simultaneously the O_2 and SO_2 content in the flowing argon. The results are given in Figure 105 for a raw HZC material in contact with AKM glass under argon atmosphere $pO_2 = 10^{-5}$ bar at 1250°C.

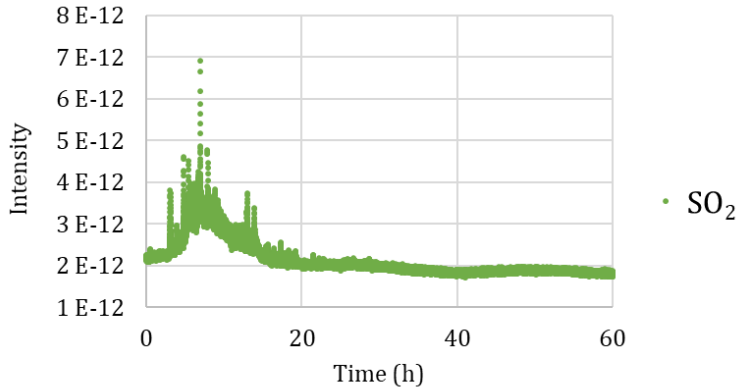

Figure 105: SO_2 blistering (redox shock) of AKM glass in contact with a raw HZC at 1250°C under argon atmosphere, analysed by mass spectroscopy.

The SO_2 level detected is the proof of the redox shock since no oxygen was detected as shown in Figure 106.

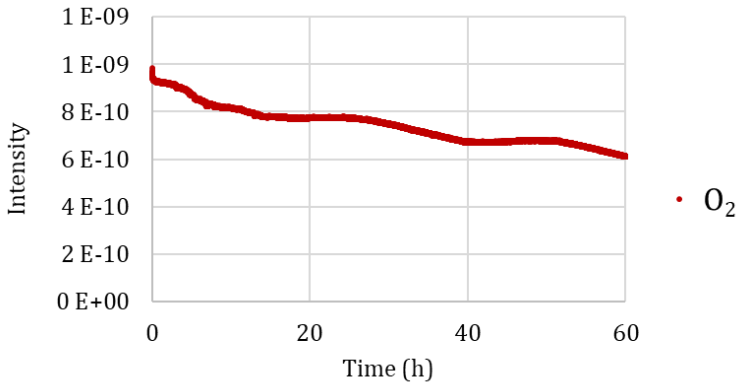

Figure 106: O_2 potential blistering of AKM glass in contact with a raw HZC at 1250°C under argon atmosphere, analysed by mass spectroscopy.

It should be noted that, in agreement with equation (48), this redox shock is observed only with raw refractories. With oxidized refractory no SO_2 blistering, and so no redox shock, is observed.

To compare the flow of SO_2 to the usual oxygen flow, data presented in Figure 78 in the previous chapter are compared with the SO_2 flow presented in Figure 107. About 20 peaks of SO_2 were observed during the 20 first hours, whereas continuous O_2 blistering is observed while testing a material under oxygen rich pO_2 (Figure 107).

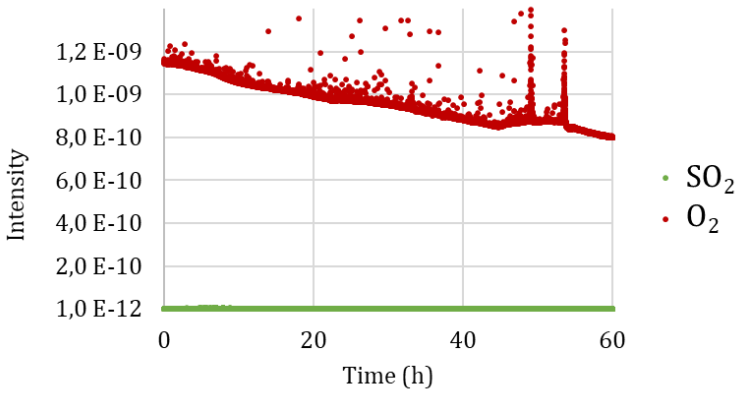

Figure 107: Comparison of O_2 flow vs SO_2 flow, using mass spectrometry, of AKM glass in contact with a raw HZC at 1250°C under argon atmosphere.

This fizzing phenomenon resulting from a redox shock is observed with glass in contact with raw refractories. However, the blistering intensity and duration are much lower compared to the intense and permanent oxygen blistering. Moreover, the fizzing is no more observed when glass is in contact with an oxidized refractory. This phenomenon cannot be excluded under certain conditions, however, redox shock and reboil process cannot be considered to explain our results. Consequently, the proposed scenario for blistering is schematized hereafter (Figure 108). Once all the refractory is oxidized, oxygen transport through the refractory is possible by semi-permeability phenomenon. This step requires the material to be a mixed ionic and electronic conductor. It turns out that all oxygen transport takes place only in the zirconia network. For blistering to occur, the zirconia network must be percolating to ensure the transport from the O_2-rich interface to the glass/refractory interface, where bubbles nucleate. If the zirconia is not percolating, the flux is not possible and no blistering can

occur. At the same level of vitreous phase, its nature could modify the zirconia grains distribution during the cooling step of the manufactured refractories.

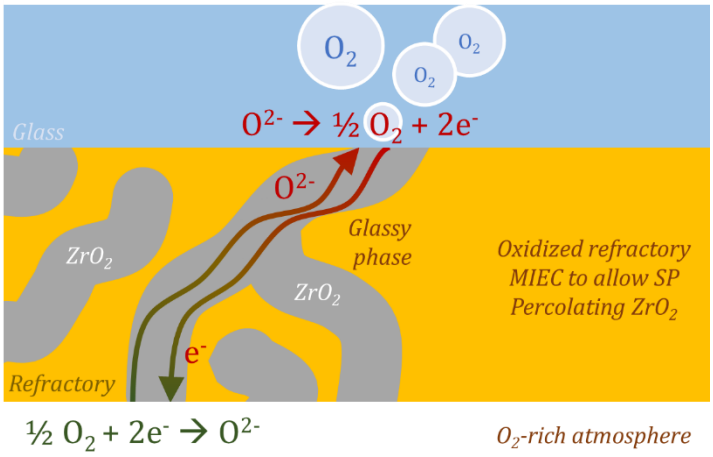

Figure 108: Scheme of the previous mentioned blistering scenario for glass in contact with fused-cast refractories.

Moreover, the following relations were determined according to the experiments detailed in chapters 3 and 4:

$$\sigma_{vph}^{HZA} > \sigma_{ZrO_2}^{HZA} \quad (52)$$

$$\sigma_{ZrO_2}^{HZB} > \sigma_{vph}^{HZB} \quad (53)$$

$$\sigma_{tot}^{HZA} > \sigma_{tot}^{HZB} or\ \sigma_{tot}^{HZC} \quad (54)$$

$$J_{O_2}^{HZA} > J_{O_2}^{HZB}\ or\ J_{O_2}^{HZC} \quad (55)$$

With σ_{vph}^{X} the conductivity of the vitreous phase of the studied reference, $\sigma_{ZrO_2}^{X}$ the conductivity of the zirconia phase of the studied reference, σ_{tot}^{X} the total conductivity of the reference and $J_{O_2}^{X}$ the oxygen flux.

As a conclusion, the flux depends on the distribution of the zirconia phase and not on the total conductivity of the refractory. For example, in the case of HZA, the flow is more intense because the vitreous phase should improve the percolation of the zirconia phase (grain/grain contacts) and not because the total conductivity of the HZA material is higher than other materials. The semipermeation cannot occur in the vitreous phase since it is only ionic conductive and blocking for oxygen vacancies.

General conclusions and perspectives

The contact between glass in fusion and refractories is sometimes leading to a blistering phenomenon within the molten glass. To date, the mechanisms of the blistering phenomenon proposed in the literature fail to win unanimous support. The purpose of this work was to propose one scenario to account for the blistering phenomenon of glass in contact fused-cast refractories. These refractories show specific electrical characteristics since fused-cast refractories are composites made of zirconia (mixed conductor) and a vitreous phase (ionic conductor).

Using original devices, the key blistering parameters for both fused-cast refractories and sintered materials were identified in chapter 4 and summarized in chapter 5. It could be noted that this study was not performed on model materials but on industrial ones. However, the results obtained are very reproducible, which made it possible to develop the blistering scenario. Although the materials tested are very different in terms of chemical composition, microstructure and electrical properties, the same key steps are proposed to understand the blistering mechanisms.

At the fundamental level, it was shown for the first time that the transport of oxygen only takes place by oxygen semipermeability through the zirconia network of the refractory. In the case of fused-cast refractories, the oxygen flux only depends on the distribution and on the electrical properties of the zirconia phase, and not on the total conductivity of the refractory.

At the industrial level, this work allows recommendations to reduce the blistering phenomenon. Doping zirconia is very effective in reducing blistering phenomenon. While doping zirconia with M^{2+} (for example CaO) or M^{3+} (for example Y_2O_3) increases considerably the oxygen vacancies concentration. Oxygen vacancies become the majority carriers, the electron concentration and consequently the electronic conductivity decrease and therefore the permeation flux decreases. Doping zirconia with a valence higher than 4, such as Ta_2O_5, has the opposite effect since it induces a reduction in oxygen vacancy concentration. Consequently, the ionic conductivity of the HZFC refractory decreases significantly and the material becomes more resistive.

Therefore, it also reduces noticeably the oxygen semipermeability flux and as a result the blistering process.

Even if the vitreous phase does not have a direct influence in the blistering mechanism it modifies the zirconia microstructure during the manufacture process and therefore it influences the blistering intensity. Indeed, blistering could also be prevented while changing the solidification process by modifying the vitreous phase composition, in order to avoid the zirconia percolation or to increase the zirconia tortuosity.

Within the framework of the proposed scenario, it was important to consider past results obtained by Saint-Gobain to reinforce the mechanism built during this thesis. To our knowledge, all the results obtained may be interpreted from our scenarios. It should be noted that Baucke's results, obtained in the Schott Laboratory and published in 1988, cannot be applicable to other glass/refractory couples than the one studied in the referred paper.

During this work, the conditions allowing the blistering start and enhancing the blistering intensity were detailed. It was also demonstrated that the glass/refractory interface plays an important role in the blistering intensity and stop.

According to all the results obtained during this project, additional experiments can be proposed to further improve our understanding of some parameters composing the blistering scenario. The electrochemical measurements performed during this thesis allowed to measure *in situ* the permeation flux and therefore the blistering phenomenon. These results could be supplemented by ^{18}O radio-tracer studies, to give another proof for the model proposed, especially on porous zircon. Indeed, by analyzing ^{18}O radio-tracers it could confirm that oxygen transport only occurs through the zirconia phase for HZFC products.

A specific work on oxygen solubility and interface phenomena has to be done to enhance the comprehension. Especially on the bubble nucleation and the formation of a boundary layer at the interface following diffusion between glass and refractory. Zircon formation, in case of fused-cast refractories could also be studied more in details to understand better the phenomenon and its influence on the blistering mechanism. Moreover, the contact between zirconia grains could also be sharply characterized to determine the role of the fine vitreous phase which was not measurable with X-ray tomography measurements since the resolution of the device used was only 1 µm. Furthermore, the glass wetting study on refractories was very

useful since it gives information on the interface and on the glass/refractory reactivity by *in situ* studies and not post mortem as it has been done till yet. Moreover, it would be possible to study the surface tension of the bubble during the nucleation and the detachment steps depending on the composition of the studied glass. The first results obtained during this work on the glass/refractory interface show that the study of this interface is complex and requires delicate characterizations to be done in future studies. Finally, this work could be completed on other glasses and refractories references.

References

1. Pustyl'Nikov, O. and A.Y. Guloyan, *Service and production conditions of electro-melted refractory articles.* Glass & Ceramics, 2009. **66**.
2. AFNOR, *Produits réfractaires.* Recueil des normes, 1987.
3. Vasil'eva, L., et al., *Zirconium refractory for optical glass melting.* Glass and Ceramics, 1981. **38**(6): p. 278-280.
4. Poirier, J., *Définition, classification et domaines d'application des céramiques réfractaires.* Techniques de l'ingénieur, 2014. **N4804 V1**.
5. Dubova, O. and L. Voloshinova, *Service of refractories during high-temperature glass melting.* Glass and Ceramics, 1962. **18**(10): p. 527-530.
6. Jacques, D., *Comportement des réfractaires au contact des verres industriels de Saint-Gobain.* http://www.idverre.net/veille/dostec/contact-refractaire-verre/contact-refractaire-verre.php consulted 25/03/2020.
7. Gottardi, V., *Refractories for the glass industry.* Journal of non-crystalline solids, 1986. **80**(1-3): p. 93-102.
8. Busby, T., *The contribution of refractories in glass making development.* Materials & Design, 1985. **6**(5): p. 210-217.
9. Busby, T., *Progress in refractory usage in the glass industry.* Transactions of the Indian Ceramic Society, 1987. **46**(5): p. 142-148.
10. Busby, T., *Progress of glass making refractories.* Journal of Non-Crystalline Solids, 1977. **26**(1-3): p. 264-306.
11. Hrma, P., J. Bartoň, and T. Tolt, *Interaction between solid, liquid and gas during glass batch melting.* Journal of Non-Crystalline Solids, 1986. **84**(1-3): p. 370-380.
12. Pigeonneau, F., *Coupled modelling of redox reactions and glass melt fining processes.* Glass Technology - European Journal of Glass Science and Technology Part A, Society of Glass Technology, 2007.
13. Vernerová, M., et al., *Gas release phenomena in soda-lime-silica glass.* Journal of Non-Crystalline Solids, 2018. **500**: p. 158-166.
14. Hrma, P., et al., *Effect of glass-batch makeup on the melting process.* Ceramics-Silikaty, 2010. **54**(3): p. 193-211.
15. Liger-Belair, G., G. Polidori, and P. Jeandet, *Recent advances in the science of champagne bubbles.* Chemical Society Reviews, 2008. **37**(11): p. 2490-2511.
16. Beerkens, R.G. and H. de Waal, *Mechanism of Oxygen Diffusion in Glassmelts Containing Variable-Valence Ions.* Journal of the American Ceramic Society, 1990. **73**(7): p. 1857-1861.
17. Beerkens, R., *Redox and sulphur reactions in glass melting processes.* Ceramics-Silikáty, 1999. **43**(3): p. 123-131.
18. Krämer, F.W., *Solubility of gases in glass melts.* Berichte der Bunsengesellschaft für physikalische Chemie, 1996. **100**(9): p. 1512-1514.
19. Brueckner, R., *Properties and structure of vitreous silica. I.* Journal of non-crystalline solids, 1970. **5**(2): p. 123-175.
20. de Best, A., *Redox behaviour and fining of molten glass.* Eindhoven: Technische Universiteit Eindhoven, 1994.
21. Vernerová, M., et al., *Method of examination of bubble nucleation in glass melts.* Journal of Non-Crystalline Solids, 2015. **411**: p. 59-67.
22. Liger-Belair, G., R. Marchal, and P. Jeandet, *Close-up on bubble nucleation in a glass of champagne.* American journal of enology and viticulture, 2002. **53**(2): p. 151-153.

23. Phalippou, J., *Verres – Aspects théoriques.* Techniques de l'ingénieur, 2017. **AF3600 V1**.
24. Wilcox, W.R. and V.H. Kuo, *Gas bubble nucleation during crystallization.* Journal of Crystal Growth, 1973. **19**(4): p. 221-228.
25. Yanagisawa, O., et al., *The change of gas composition in bubble.* Journal of Non-Crystalline Solids, 1980. **38**: p. 599-604.
26. Yoshikawa, H., H. Miura, and Y. Kawase, *Dissolution of bubbles in glassmelts with equilibrium redox reactions: approximations for a moving bubble boundary.* Journal of materials science, 1998. **33**(10): p. 2701-2707.
27. Kočárková, H., *Stability of glass foams: experiments at the bubble scale and on vertical film*. 2011, PhD Thesis, Paris Est.
28. Němec, L. and J. Kloužek, *Modelling of glass refining kinetics. Part 1. Single bubbles.* Ceramics-Silikáty, 2003. **47**(3): p. 81-87.
29. GREENE, C.H. and H.A. LEE JR, *Effect of As_2O_3 and $NaNO_3$ on the Solution of O_2 in Soda-Lime Glass.* Journal of the American Ceramic Society, 1965. **48**(10): p. 528-533.
30. Weinberg, M.C., *Dissolution of a stationary bubble in a glassmelt with a reversible chemical reaction: Rapid forward reaction rate constant.* Journal of the American Ceramic Society, 1982. **65**(10): p. 479-485.
31. Pigeonneau, F., D. Martin, and O. Mario, *Shrinkage of an oxygen bubble rising in a molten glass.* Chemical engineering science, 2010. **65**(10): p. 3158-3168.
32. Guloyan, Y. and O. Pustyl'nikov, *Physical-chemical interactions during contact between molten glass and refractories.* Glass & Ceramics, 2011. **67**.
33. Pavlovskii, V. and Y.S. Sobolev, *Dissolving of baddeleyite-corundum refractories in optical glass melts.* Glass and ceramics, 1993. **50**(2): p. 60-62.
34. Dunkl, M., *Glass melt-refractories interaction.* VERRE-PARIS THEN VERSAILLES-, 2003. **9**(2): p. 35-43.
35. Gramenitskii, E. and A. Batanova, *Regular features of the interaction between refractories and glass-forming melts in light of the theory of diffusion zones.* Glass and ceramics, 1996. **53**(8): p. 229-233.
36. Aksel, C., *The microstructural features of an alumina–mullite–zirconia refractory material corroded by molten glass.* Ceramics international, 2003. **29**(3): p. 305-309.
37. Heidrich, R. and A. Gupta, *Fused Cast AZS Glassy Phase Exudation: Intrinsic or Pathologic Property?* Refractories (Engl. Transl.);(United States), 1986. **(United States) 27**.
38. Plumat, E., F. Toussaint, and M. Boffe, *Formation of bubbles by electrochemical processes in glass.* Journal of the American Ceramic Society, 1966. **49**(10): p. 551-558.
39. van Dijk, F.A.G., *Glass defects originating from glass melt/fused cast AZS refractory interaction*. 1994, PhD Thesis, Technische Universiteit Eindhoven.
40. Astaf'eva, L., et al., *Formation of bubbles at the interface between fusion-cast refractories and molten glass.* Glass and Ceramics, 1979. **36**(4): p. 192-195.
41. Fleischmann, B., *Glassy phase segregation from AZS blocks.* Glass science and technology (Frankfurt), 2005. **78**(6): p. 295-300.
42. Krämer, F., *Analysis of gases evolved by AZS refractories and by refractory/glass melt reactions. Techniques and results. Contribution to the bubble-forming mechanism of AZS material.* Glastechnische Berichte, 1992. **65**(4): p. 93-98.
43. Dunkl, M. *Boundary layers Refractory/Glass melt and Glass defects*. in *Advanced Materials Research*. 2008. Trans Tech Publ.
44. Dunkl, M., *Investigation of the liberation of glassy phase from fused cast AZS materials.* Glastech. Ber. K, 1990. **63**: p. 370-380.
45. Kiryukhin, V., et al., *Formation of gaseous inclusions on the interface between refractory and glass.* Glass and Ceramics, 1988. **45**(11): p. 404-407.

46. Baucke, F. and G. Röth, *Electrochemical mechanism of the oxygen bubble formation at the interface between oxidic melts and zirconium silicate refractories.* Glastechnische Berichte, 1988. **61**(5): p. 109-118.
47. Bach, H., F.K. Baucke, and D. Krause, *Electrochemistry of glasses and glass melts, including glass electrodes*. 2013: Springer Science & Business Media.
48. Baucke, F.G., *Electrochromic mirrors with variable reflectance.* Solar energy materials, 1987. **16**(1-3): p. 67-77.
49. Pankova, N., *Diagnosis of causes of bubble formation in glass products.* Glass and Ceramics, 1989. **46**(8): p. 329-332.
50. Rüssel, C., *Redox behavior and electrochemical behavior of glass melts*, in *Properties of Glass-Forming Melts*. 2005, CRC Press. p. 38-66.
51. Rüssel, C., R. Kohl, and H.A. Schaeffer, *Interaction between oxygen activity of Fe_2O_3 doped soda-lime-silica glass melts and physically dissolved oxygen.* Glastech. Ber, 1988. **61**(8): p. 209-213.
52. BAUCKE, F.K. and J. Duffy, *The effect of basicity on redox equilibria in molten glasses.* Physics and chemistry of glasses, 1991. **32**(5): p. 211-218.
53. BAUCKE, F.K. and J. Duffy, *Oxidation states of metal ions in glass melts.* Physics and chemistry of glasses, 1994. **35**(1): p. 17-21.
54. Duffy, J. and M. Ingram, *An interpretation of glass chemistry in terms of the optical basicity concept.* Journal of Non-Crystalline Solids, 1976. **21**(3): p. 373-410.
55. Duffy, J. and M. Ingram, *Comments on the application of optical basicity to glass.* Journal of non-crystalline solids, 1992. **144**: p. 76-80.
56. BAUCKE, F. and J. Duffy, *Redox reactions between cations of different polyvalent elements in glass melts: an optical basicity study.* Physics and chemistry of glasses, 1993. **34**(4): p. 158-163.
57. Di Nardo, C., *Etude et contrôle des réactions d'oxydoréduction au cours de l'élaboration des matrices vitreuses de confinement des déchets nucléaires*. 2002, Montpellier 2.
58. Pinet, O. and C. Di Nardo, *Redox phenomena in glass melts; Les phenomènes d'oxydoréduction dans les verres d'oxyde.* 2000.
59. Pinet, O., J. Phalippou, and C. Di Nardo, *Modeling the redox equilibrium of the Ce^{4+}/Ce^{3+} couple in silicate glass by voltammetry.* Journal of non-crystalline solids, 2006. **352**(50-51): p. 5382-5390.
60. Chernina, L. and I. Suslova, *Tendency of refractories to liberate bubbles into molten glass.* Glass and Ceramics, 1973. **30**(1): p. 18-20.
61. Dzyuzer, V.Y., *Electrofused AZS refractories for high-capacity glass-founding furnaces.* Refractories and industrial ceramics, 2013. **54**(4): p. 304-306.
62. Sokolov, V., V. Kiryukhin, and L. Shvorneva, *Influence of melting conditions on the quality of baddeleyite-corundum refractories.* Refractories, 1986. **27**(9-10): p. 536-540.
63. Dalmazzo, V.A., *Study of the blistering phenomenon between fused-cast high zirconia refractories and cover glass or LCD glass.* Internal confidential report, Saint-Gobain Research Provence, 2015. **RR597**.
64. Du, N., *Étude des phénomènes de bullage à l'interface verre-réfractaire : recherche des voies d'optimisation de l'essai de bullage et d'amélioration de la cotation.* Internal confidential report, Saint-Gobain Research Provence, 2004. **RE1003**.
65. Auerbach, A., *Des essais de bullage sur les matériaux réfractaires électrofondus.* Internal report, SEPR, 1973.
66. Cabodi, I., *Blistering sodocalcique.* Internal confidential presentation, Saint-Gobain Research Provence, 2018.

67. Riffaud, A., *Oxygen semi-permeability and conductivity characterization of ceramics.* Internal confidential report, Saint-Gobain Research Provence, 2017. **RE2427**.
68. Y. Boussant-Roux, M.G., *Etude du phénomène de bullage basse température de l'ER1195.* Internal report, SEPR, 1999. **RR375**.
69. Boussant-Roux, Y., E. Schiavo, and A. Zanoli, *Fused cast refractory block with high zirconia content*. 2012, U.S. Patent No. 8,124,554. 28 Feb. 2012.
70. Sadik, C., I.-E. El Amrani, and A. Albizane, *Recent advances in silica-alumina refractory: A review.* Journal of Asian Ceramic Societies, 2014. **2**(2): p. 83-96.
71. Garzarolli, F., et al. *Effects of high neutron fluences on microstructure and growth of Zircaloy-4*. in *Zirconium in the Nuclear Industry: Eighth International Symposium*. 1989. ASTM International.
72. Subbarao, E., H. Maiti, and K. Srivastava, *Martensitic transformation in zirconia.* Physica status solidi (a), 1974. **21**(1): p. 9-40.
73. Teufer, G., *The crystal structure of tetragonal ZrO2.* Acta Crystallographica, 1962. **15**(11): p. 1187-1187.
74. Aldebert, P. and J.P. TRAVERSE, *Structure and ionic mobility of zirconia at high temperature.* Journal of the American Ceramic Society, 1985. **68**(1): p. 34-40.
75. Deville, S., G. Guénin, and J. Chevalier, *Martensitic transformation in zirconia: Part I. Nanometer scale prediction and measurement of transformation induced relief.* Acta materialia, 2004. **52**(19): p. 5697-5707.
76. Yeugo Fogaing, E., *Caractérisation à haute température des propriétés d'élasticité de réfractaires électrofondus et de bétons réfractaires*. 2006, PhD Thesis, Limoges.
77. Ratto, P., *Glass quality: what can we expect from fused cast refractory?* International glass journal (Testo stampato), 1994(80): p. 28-33.
78. Massard, L., *Étude du fluage de réfractaires électrofondus du système alumine-zircone-silice*. 2005, PhD Thesis, École Nationale Supérieure des Mines de Paris.
79. Boussuge, M., *Investigation of the thermomechanical properties of industrial refractories: the French programme PROMETHEREF.* Journal of materials science, 2008. **43**(12): p. 4069-4078.
80. Sibil, A., *Comportement thermomécanique et endommagement de nouveaux réfractaires verriers à très haute teneur en zircone: investigation des mécanismes de fissuration par EBSD et émission acoustique*. 2011, PhD Thesis, Institut National des Sciences Appliquées de Lyon.
81. Carbajal, G.V., et al., *Microstructure and mechanical behavior of alumina–zirconia–mullite refractory materials.* Ceramics International, 2012. **38**(2): p. 1617-1625.
82. Steil, M.C., *Synthèse, frittage et caractérisation électrique des oxydes céramiques, rôle de la microstructure.* HDR Report, Grenoble, 2018.
83. Schouler, E., G. Giroud, and M. Kleitz, *Applications selon Bauerle du tracé des diagrammes d'admittance complexe en électrochimie des solides-II.—Étude de la conductivité de la zircone stabilisée à l'yttrium.* Journal de chimie physique, 1973. **70**: p. 1309-1316.
84. Steil, M., F. Thevenot, and M. Kleitz, *Densification of yttria-stabilized zirconia: impedance spectroscopy analysis.* Journal of the Electrochemical Society, 1997. **144**(1): p. 390.
85. Irvine, J.T., D.C. Sinclair, and A.R. West, *Electroceramics: characterization by impedance spectroscopy.* Advanced materials, 1990. **2**(3): p. 132-138.
86. Badwal, S., *Electrical conductivity of single crystal and polycrystalline yttria-stabilized zirconia.* Journal of materials science, 1984. **19**(6): p. 1767-1776.
87. Dessemond, L., et al., *Electric conduction-blocking effects of voids and second phases in stabilized zirconia.* Applied Physics A, 1993. **57**(1): p. 57-60.

88. Kleitz, M., L. Dessemond, and M. Steil, *Model for ion-blocking at internal interfaces in zirconias.* Solid State Ionics, 1995. **75**: p. 107-115.
89. Kleitz, M. and M. Steil, *Microstructure blocking effects versus effective medium theories in YSZ.* Journal of the european ceramic society, 1997. **17**(6): p. 819-829.
90. Cordier, A., et al., *On the role of the pore morphology on the electrical conductivity of porous yttria-stabilized zirconia.* Journal of the European Ceramic Society, 2019. **39**(7): p. 2518-2525.
91. El Khal, H., *Relations frittage-microstructure-propriétés électriques des céramiques de type LAMOX*. 2017, PhD Thesis, Université Grenoble Alpes.
92. Tuller, H.L., *Mixed ionic-electronic conduction in a number of fluorite and pyrochlore compounds.* Solid State Ionics, 1992. **52**(1-3): p. 135-146.
93. Sunarso, J., et al., *Mixed ionic–electronic conducting (MIEC) ceramic-based membranes for oxygen separation.* Journal of membrane science, 2008. **320**(1-2): p. 13-41.
94. Balachandran, U., et al., *Dense ceramic membranes for partial oxidation of methane to syngas.* Applied Catalysis A: General, 1995. **133**(1): p. 19-29.
95. Bouwmeester, H.J., *Dense ceramic membranes for methane conversion.* Catalysis today, 2003. **82**(1-4): p. 141-150.
96. Wei, Y., et al., *Dense ceramic oxygen permeable membranes and catalytic membrane reactors.* Chemical Engineering Journal, 2013. **220**: p. 185-203.
97. Fouletier, J., P. Fabry, and M. Kleitz, *Electrochemical semipermeability and the electrode microsystem in solid oxide electrolyte cells.* Journal of The Electrochemical Society, 1976. **123**(2): p. 204-213.
98. Steele, B., *Oxygen ion conductors and their technological applications.* Materials Science and Engineering: B, 1992. **13**(2): p. 79-87.
99. Fabry, P., M. Kleitz, and C. Déportes, *Sur l'utilisation d'une electrode ponctuelle dans les cellules à oxyde electrolyte solide: I. Application aux mesures thermodynamiques et à la détermination du nombre de transport electronique de l'electrolyte.* Journal of Solid State Chemistry, 1972. **5**(1): p. 1-10.
100. Salles, C., et al., *Determining the rate-limiting step during oxygen semi-permeation of $CaTi_{0.9}Fe_{0.1}O_{3-\delta}$ oxygen transport membranes.* Journal of membrane science, 2017. **527**: p. 191-197.
101. Deportes, C., et al., *Electrochimie des Solides, Presses Universitaires de Grenoble*. 1994, France. p. 360.
102. *XANES: Application.* Chemistry LibreTexts, https://chem.libretexts.org/Bookshelves/Physical_and_Theoretical_Chemistry_Textbook_Maps/Supplemental_Modules_(Physical_and_Theoretical_Chemistry)/Spectroscopy/X-ray_Spectroscopy/XANES%3A_Application#Soft_X-ray_Instrumentation, consulted 22/04/2020.
103. Carpenter, M.H., *Helium Atmosphere Chamber for Soft X-ray Spectroscopy of Biomolecules*. 2010: Thesis, University of California, Davis.
104. Gillot, J., *Oxidation state of Fe in High Zirconia electrofused refractories.* Internal confidential report, SGR/EMC2 – JG/SR, 2016. **N° 1507/16**.
105. *XANES: Theory.* Chemistry LibreTexts, https://chem.libretexts.org/Bookshelves/Physical_and_Theoretical_Chemistry_Textbook_Maps/Supplemental_Modules_(Physical_and_Theoretical_Chemistry)/Spectroscopy/X-ray_Spectroscopy/XANES%3A_Theory/XANES%3A_Theory2, consulted 20/04/2020.
106. Newville, M., *https://www.lehigh.edu/imi/teched/GlassCSC/SuppReading/Tutorials.pdf*. Consortium for Advanced Radiation Sources University of Chicago, Chicago, IL, Revision 1.6 July 22, 2004

107. Ravel, B. and M. Newville, *ATHENA, ARTEMIS, HEPHAESTUS: data analysis for X-ray absorption spectroscopy using IFEFFIT.* Journal of synchrotron radiation, 2005. **12**(4): p. 537-541.
108. Durst, J., *Understanding of HZFC blistering: XANES study of the oxidation state of Fe and Ti impurities.* Internal confidential report, SGR Paris, 2018. **C15069, 4703**.
109. Brossard, S., *XANES measurements at the Fe and Zr edge of refractories materials.* Note Flash SGR/EMC2-SB/PP N°1660/19, 2019.
110. Wilke, M., et al., *Oxidation state and coordination of Fe in minerals: An Fe K-XANES spectroscopic study.* American Mineralogist, 2001. **86**(5-6): p. 714-730.
111. Thiery, C., *Tomographie à rayons X.* Techniques de l'ingénieur, 2013.
112. Hammersley, J.M., *Percolation processes: Lower bounds for the critical probability.* The Annals of Mathematical Statistics, 1957. **28**(3): p. 790-795.
113. Madi, K., *Influence de la morphologie tridimensionnelle des phases sur le comportement mécanique de réfractaires électrofondus*. 2006, PhD Thesis, Paris, ENMP.
114. Ding, Y., *Analyse morphologique de la microstructure 3D de réfractaires électrofondus à très haute teneur en zircone: relations avec les propriétés mécaniques, chimiques et le comportement pendant la transformation quadratique-monoclinique*. 2012, Paris, ENMP.
115. Aldebert, P. and J.-P. Traverse, *Structure and ionic mobility of zirconia at high temperature.* Journal of the American Ceramic Society, 1985. **68**(1): p. 34-40.
116. Schouler, E., *Etude de cellules à oxyde électrolyte solide par la méthode des impédances complexes*. 1979, PhD Thesis, Grenoble.
117. Gioia, A., *Influence de dopants M2O5 (M= Nb, Ta) sur les relations structure-résistivité électrique à hautes températures des matériaux réfractaires à haute teneur en zircone*. 2009, Montpellier 2.
118. Nahir, T.M., *Impedance Spectroscopy: Theory, Experiment, and Applications, Edited by Evgenij Barsoukov (Texas Instruments Inc.) and J. Ross Macdonald (University of North Carolina, Chapel Hill). John Wiley & Sons, Inc.: Hoboken, NJ. 2005.* 2005, ACS Publications.
119. McNealy, B.E. and J.L. Hertz, *On the use of the constant phase element to understand variation in grain boundary properties.* Solid State Ionics, 2014. **256**: p. 52-60.
120. Nahir, T.M., *Impedance Spectroscopy: Theory, Experiment, and Applications, Edited by Evgenij Barsoukov (Texas Instruments Inc.) and J. Ross Macdonald (University of North Carolina, Chapel Hill). John Wiley & Sons, Inc.: Hoboken, NJ. 2005.* 2005, ACS Publications. p. 197.
121. Maxwell, J.C., *A treatise on electricity and magnetism*. Vol. 1. 1873: Oxford: Clarendon Press.
122. Bergman, D.J., *The dielectric constant of a composite material—a problem in classical physics.* Physics Reports, 1978. **43**(9): p. 377-407.
123. Bergman, D.J., *Rigorous bounds for the complex dielectric constant of a two-component composite.* Annals of Physics, 1982. **138**(1): p. 78-114.
124. Mizusaki, J., et al., *Simple mathematical model for the electrical conductivity of highly porous ceramics.* Journal of the American Ceramic Society, 1996. **79**(1): p. 109-113.
125. Weppner, W., *Tetragonal zirconia polycrystals—a high performance solid oxygen ion conductor.* Solid State Ionics, 1992. **52**(1-3): p. 15-21.
126. Riffaud, A., *Oxygen semi-permeability and conductivity characterization of ceramics.* Internal report, Centre de Recherches et d'Etudes Européen, 2017. **RE2427**.

127. Schouler, E., N. Mesbahi, and G. Vitter, *In situ study of the sintering process of yttria stabilized zirconia by impedance spectroscopy.* Solid State Ionics, 1983. **9**: p. 989-996.
128. Déportes, C., et al., *Electrochimie des Solides Grenoble Sciences*. 1987, Grenoble.
129. Souquet, J.-L., M.L.F. Nascimento, and A.C.M. Rodrigues, *Charge carrier concentration and mobility in alkali silicates.* The Journal of chemical physics, 2010. **132**(3): p. 034704.
130. Kumar, A., D. Rajdev, and D. Douglass, *Effect of oxide defect structure on the electrical properties of ZrO_2.* Journal of the American Ceramic Society, 1972. **55**(9): p. 439-445.
131. Patterson, J.W., E. Bogren, and R.A. Rapp, *Mixed Conduction in $Zr_{0.85}Ca_{0.15}O_{1.85}$ and $Th_{0.85}Y_{0.15}O_{1.925}$ Solid Electrolytes.* Journal of the Electrochemical Society, 1967. **114**(7): p. 752–758.
132. Patterson, J., *Conduction domains for solid electrolytes.* Journal of the Electrochemical Society, 1971. **118**(7): p. 1033–1039.
133. Huggins, R., *Simple Method to Determine Electronic Conductivity in Mixed A Review.*
134. Nasrallah, M. and D. Douglass, *Ionic and electronic conductivity in Y_2O_3-doped monoclinic ZrO_2.* Journal of The Electrochemical Society, 1974. **121**(2): p. 255-262.
135. Chen, C., et al., *Microstructural development, electrical properties and oxygen permeation of zirconia-palladium composites.* Solid State Ionics, 1995. **76**(1-2): p. 23-28.
136. Chen, C., et al., *Oxygen permeation through oxygen ion oxide-noble metal dual phase composites.* Solid State Ionics, 1996. **86**: p. 569-572.
137. Kharton, V., et al., *Oxygen permeability and Faradaic efficiency of $Ce_{0.8}Gd_{0.2}O_{2-\delta}$–$La_{0.7}Sr_{0.3}MnO_{3-\delta}$ composites.* Journal of the European Ceramic Society, 2001. **21**(10-11): p. 1763-1767.
138. Kharton, V., et al., *Oxygen transport in $Ce_{0.8}Gd_{0.2}O_{2-\delta}$-based composite membranes.* Solid State Ionics, 2003. **160**(3-4): p. 247-258.
139. Bouwmeester, H. and P.J. Gellings, *The CRC handbook of solid state electrochemistry*. 1997.
140. Shaula, A., et al., *Oxygen permeability of mixed-conducting composite membranes: effects of phase interaction.* Journal of Solid State Electrochemistry, 2006. **10**(1): p. 28-40.
141. Anderson, M. and Y. Lin, *Carbonate–ceramic dual-phase membrane for carbon dioxide separation.* Journal of Membrane Science, 2010. **357**(1-2): p. 122-129.
142. Rui, Z., et al., *Ionic conducting ceramic and carbonate dual phase membranes for carbon dioxide separation.* Journal of membrane science, 2012. **417**: p. 174-182.
143. Patrício, S.G. and F.M. Marques, *Benchmarking the ambipolar conductivity of composite electrolytes for gas separation membranes.* International Journal of Energy Research, 2016. **40**(15): p. 2150-2161.
144. Rui, Z., et al., *Modeling and analysis of carbon dioxide permeation through ceramic-carbonate dual-phase membranes.* Journal of Membrane Science, 2009. **345**(1-2): p. 110-118.
145. Steil, M., J. Fouletier, and P.-M. Geffroy, *Surface exchange polarization vs. gas concentration polarization in permeation through mixed ionic-electronic membranes.* Journal of Membrane Science, 2017. **541**: p. 457-464.
146. Li, C., et al., *Modelling of oxygen transport through mixed ionic-electronic conducting (MIEC) ceramic-based membranes: An overview.* Journal of Membrane Science, 2018. **567**: p. 228-260.
147. Mauvy, F. and J. Fouletier, *Determination of Thermodynamic and Transport Properties of Non-Stoichiometric Oxides.* Stoichiometry and Materials Science: When Numbers Matter, 2012: p. 175.

148. Geffroy, P.-M., et al., *Understanding and identifying the oxygen transport mechanisms through a mixed-conductor membrane.* Chemical Engineering Science, 2017. **162**: p. 245-261.
149. Geffroy, P.-M., et al., *Characterization of electrical conduction and nature of charge carriers in mixed and ionic conductors.* Journal of Power Sources, 2017. **360**: p. 70-79.
150. Geffroy, P.-M., et al., *The impact of experimental factors on oxygen semi-permeation measurements.* Journal of The Electrochemical Society, 2012. **160**(1): p. F60.
151. Bouwmeester, H.J., et al., *Oxygen semipermeability of erbia-stabilized bismuth oxide.* Solid State Ionics, 1992. **53**: p. 460-468.
152. Bouwmeester, H.J., H. Kruidhof, and A. Burggraaf, *Importance of the surface exchange kinetics as rate limiting step in oxygen permeation through mixed-conducting oxides.* Solid state ionics, 1994. **72**: p. 185-194.
153. Dou, S., C. Masson, and P. Pacey, *Mechanism of oxygen permeation through lime-stabilized zirconia.* Journal of the Electrochemical Society, 1985. **132**(8): p. 1843.
154. Lin, Y.S., W. Wang, and J. Han, *Oxygen permeation through thin mixed-conducting solid oxide membranes.* AIChE journal, 1994. **40**(5): p. 786-798.
155. Durst, J., *"Understanding of HZFC blistering": XANES study of the oxidation state of Fe and Ti impurities.* Internal report, SGR Paris, 2018. **C15069, 4703**.
156. Galerie, A., J. Fouletier, and P. Sarrazin, *Les mécanismes de la corrosion sèche-Une approche cinétique: Une approche cinétique*. 2012: EDP Sciences.
157. Beerkens, R., H. de Waal, and F. Simonis, *Handbook for Glass Technologist.* TNO-TPD Glass Technology, Eindhoven, 1997.
158. Chatain, D., et al., *New experimental setup for wettability characterization under monitored oxygen activity: I, role of oxidation state and defect concentration on oxide wettability by gold.* Journal of the American Ceramic Society, 1993. **76**(6): p. 1568-1576.
159. Evaris, U., *The Corrosion of Metals.* Arnold, London, 1926: p. 93.
160. Bockris, J., *O'M.; Reddy, AKN Modern Electrochemistry, Vol. 2*. 1970, Plenum Press, New York. p. 1301-1305.
161. Douglass, D. and C. Wagner, *The Oxidation of Oxygen-Deficient Zirconia and Its Relationship to the Oxidation of Zirconium.* Journal of The Electrochemical Society, 1966. **113**(7): p. 671.
162. Vest, R., N. Tallan, and W. TRlPP, *Electrical properties and defect structure of zirconia: I, monoclinic phase.* Journal of the American Ceramic Society, 1964. **47**(12): p. 635-640.
163. Madeyski, A. and W. Smeltzer, *Oxygen diffusion in monoclinic zirconia.* Materials Research Bulletin, 1968. **3**(4): p. 369-375.
164. Kofstad, P. and D. Ruzicka, *On the defect structure of ZrO_2 and HfO_2.* Journal of The Electrochemical Society, 1963. **110**(3): p. 181.
165. Vest, R. and N. Tallan, *Electrical properties and defect structure of zirconia: II, tetragonal phase and inversion.* Journal of the American Ceramic Society, 1965. **48**(9): p. 472-475.
166. Kopp, A., H. Näfe, and W. Weppner, *Characterization of the electronic charge carriers in TZP.* Solid state ionics, 1992. **53**: p. 853-858.
167. Gupta, T., R. Grekila, and E. Subbarao, *Electrical conductivity of tetragonal zirconia below the transformation temperature.* Journal of the Electrochemical Society, 1981. **128**(4): p. 929.
168. Chevalier, J., et al., *The tetragonal-monoclinic transformation in zirconia: lessons learned and future trends.* Journal of the American Ceramic Society, 2009. **92**(9): p. 1901-1920.

169. Yang, J., M. Youssef, and B. Yildiz, *Oxygen self-diffusion mechanisms in monoclinic Zr O 2 revealed and quantified by density functional theory, random walk analysis, and kinetic Monte Carlo calculations.* Physical Review B, 2018. **97**(2): p. 024114.
170. Mauvy, F., et al., *Oxygen permeation fluxes through La2Cu0. 5Ni0. 5O4+ δ dense ceramics: Comparison with oxygen diffusion coefficients.* Solid State Ionics, 2007. **178**(19-20): p. 1200-1204.
171. Boulfrad, S., E. Djurado, and J. Fouletier, *Electrochemical characterization of nanostructured zirconias.* Solid State Ionics, 2009. **180**(14-16): p. 978-983.
172. Fabry, P. and M. Kleitz, *Electrochemical coloration and redox reactions in solid ionic conductors*, in *Electrode Processes in Solid State Ionics*. 1976, Springer. p. 331-365.
173. Salles, C., et al., *Long-term stability of iron-doped calcium titanate $CaTi_{0.9}Fe_{0.1}O_{3-\delta}$ oxygen transport membranes under non-reactive and reactive atmospheres.* Journal of Membrane Science, 2019. **583**: p. 171-179.
174. Busby, T., *Fusion cast refractory use is widespread in the melter.* The Glass industry, 1991. **72**(9).
175. Adams, R.W. and W.-C.J. Wei, *Refractory ceramics for contact with molten metal*. 1989, Google Patents.
176. Boussant-Roux, Y.M.L. and M.M. Gaubil, *Molten and cast refractory product with high zirconia content*. 2006, Google Patents.
177. Sokolov, V., *Aspects of obtaining and using fusion-cast high-zirconia refractories.* Refractories (Engl. Transl.);(United States), 1986. **27**.
178. Sokolov, V. and M. Gasparyan, *Synthesis and properties of fusion-cast refractories in the Al_2O_3–B_2O_3 system.* Refractories and Industrial Ceramics, 2004. **45**(3): p. 177-180.
179. Lataste, E., *Comportement mécanique et endommagement de réfractaires électrofondus sous sollicitation thermomécanique*. 2005, Thèse de Doctorat, Institut National des Sciences Appliquées de Lyon.
180. Fourment J., F.J., *Four de verrerie.* Techniques de l'ingénieur, 2000. **BE8848 V1**.
181. Kwon, O.H., et al., *Investigation of the electrical conductivity of sintered monoclinic zirconia (ZrO_2).* Ceramics International, 2017. **43**(11): p. 8236-8245.
182. Kröger, F., *Electronic Conductivity of Calcia-Stabilized Zirconia.* Journal of the American Ceramic Society, 1966. **49**(4): p. 215-218.
183. Poulton, D. and W. Smeltzer, *Oxygen diffusion in monoclinic zirconia.* Journal of the Electrochemical Society, 1970. **117**(3): p. 378-381.
184. Gong, J., et al., *Enhancement of the ionic conductivity of mixed calcia/yttria stabilized zirconia.* Materials Letters, 2000. **46**(2-3): p. 115-119.
185. Etsell, T. and S.N. Flengas, *Electrical properties of solid oxide electrolytes.* Chemical Reviews, 1970. **70**(3): p. 339-376.
186. Park, J.H. and R.N. Blumenthal, *Electronic Transport in 8 Mole Percent Y_2O_3-ZrO_2.* Journal of the Electrochemical Society, 1989. **136**(10): p. 2867-2876.
187. Lefrou, C., J. Fouletier, and P. Fabry, *Conductivité des électrolytes.* Techniques de l'ingénieur, 2010.
188. Uchino, T., et al., *A new model of ionic transport for single-and mixed-alkali oxide glasses based on ab initio molecular orbital calculations.* Journal of non-crystalline solids, 1992. **146**: p. 26-42.
189. Schaeffer, H., J. Mecha, and J. Steinmann, *Mobility of sodium ions in silica glass of different OH content.* Journal of the American Ceramic Society, 1979. **62**(7-8): p. 343-346.
190. Cabodi, I., *Nouveau produit électrofondu THTZ (très haute teneur en zircone) à très forte résistivité électrique pour application en fours à verre LCD – RR496.* Internal confidential report, 2009.

191. De Marchi, G., P. Mazzoldi, and A. Miotello, *Analysis of ionic conductivity in alkali and mixed-alkali aluminosilicate glasses.* Journal of non-crystalline solids, 1988. **105**(3): p. 307-312.
192. Mehrer, H., A.W. Imre, and E. Tanguep-Nijokep. *Diffusion and ionic conduction in oxide glasses*. in *Journal of Physics: Conference Series*. 2008. IOP Publishing.
193. Bunde, A., M.D. Ingram, and P. Maass, *The dynamic structure model for ion transport in glasses.* Journal of non-crystalline solids, 1994. **172**: p. 1222-1236.
194. Wiedenroth, A. and C. Rüssel, *The effect of MgO on the thermodynamics of the Fe^{2+}/Fe^{3+}-redox equilibrium and the incorporation of iron in soda-magnesia-aluminosilicate melts.* Journal of non-crystalline solids, 2003. **320**(1-3): p. 238-245.
195. Johnston, W., *Oxidation-reduction equilibria in iron-containing glass.* Journal of the American Ceramic Society, 1964. **47**(4): p. 198-201.
196. Gerlach, S., O. Claußen, and C. Rüssel, *A voltammetric study on the thermodynamics of the Fe^{3+}/Fe^{2+}-equilibrium in alkali–lime–alumosilicate melts.* Journal of non-crystalline solids, 1999. **248**(1): p. 92-98.
197. Barba-Rossa, G. and E. Janiaud, *Phénomène de bullage de dioxygène à faible température à l'interface entre un verre clair et un réfractaire à haute teneur en zircone.* Note Technique, Saint-Gobain Research Paris, 2019. **C15069 - 4493**.
198. Boloré, D., *Création et nucléation de bulles lors de la montée en température de verres recyclés mis en contact*. 2017, PhD Thesis, Université Pierre et Marie Curie - Paris VI.
199. Chopinet, M.-H., D. Lizarazu, and C. Rocanière, *L'importance des phénomènes d'oxydo-réduction dans le verre.* Comptes Rendus Chimie, 2002. **5**(12): p. 939-949.

Appendices

A. OXYGEN SENSOR

The operating principle of the oxygen sensor is based on the use of a solid electrolyte (zirconia stabilized with yttrium oxide) which is an ionic conductor at high temperature (T > 873K). The cell consists of a physically impermeable wall, made of solid oxide electrolyte, which separates two distinct atmospheres (Figure 109). The two surfaces of this wall are covered with a porous metallic layer (platinum = electrode material) which constitute the electrodes of the cell. The external electrode is in contact with the air (reference) and the gas to be analysed is led close to the measurement electrode by an alumina capillary. The electromotive force (e.m.f.) measured between the two electrodes satisfy Nernst's law [97, 101]:

$$E = \frac{RT}{4F} \ln\left(\frac{P_2}{pO_2(air)}\right)$$

With:

E: e.m.f. of the sensor (in V, negative value);

F: Faraday constant (96 485 $C.mol^{-1}$);

T: temperature (in K);

R: universal gas constant (8,314 $J.mol^{-1}.K^{-1}$);

pO_2 (air): reference oxygen partial pressure (pO_2 (air) = 0.2 bar);

P_2: measured oxygen partial pressure (in bar).

Then:

$$P_2 = 0.2 \times 10^{\frac{20183 \times E}{T}}$$

As an example, for E = - 0.15 V, at 700°C, the measured oxygen partial pressure is: 1.55×10^{-4} bar. The oxygen content in the gas is often expressed in ppm, i.e., 155 ppm in that case.

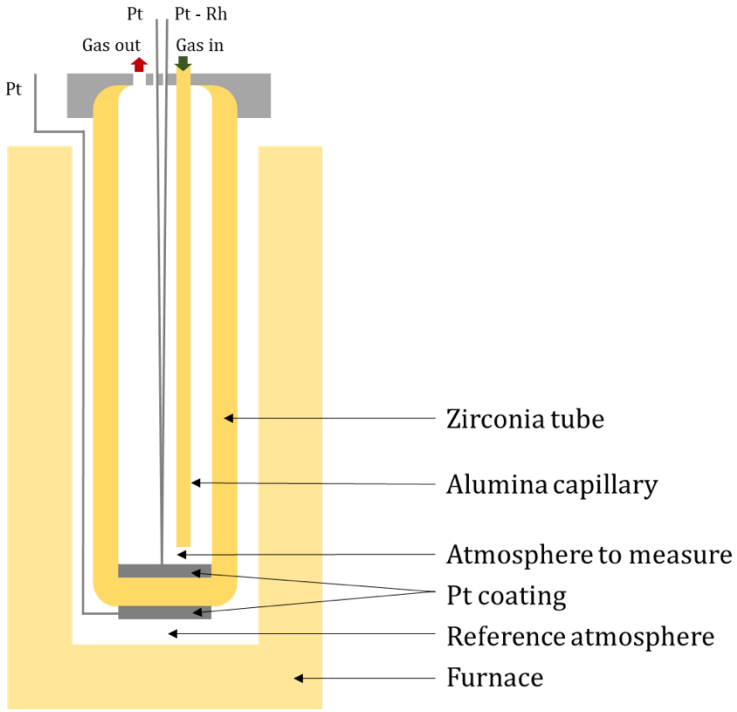

Figure 109: Oxygen sensor components [101].

B. FUSED-CAST REFRACTORIES PROCESS

Fused-cast refractory materials have been developed to constitute the internal walls of some glass furnaces. The refractories obtained by electrofusion are very compact because they have a very low closed porosity (less than 2%). Another advantage of this family is that it is possible to manufacture very large blocks with complex shapes. Two main families of fused-cast refractories are used in glass industry: AZS composed of $Al_2O_3/ZrO_2/SiO_2$ and HZFC with a very high zirconia content (>80 wt.% ZrO_2) [174, 175].

i. Fusion process

These materials are obtained through a manufacturing process in which the raw materials in the form of powders, are melted between 1800°C and 2400°C (Figure 110). These high temperatures necessary for the fusion of all the raw materials are reached with an electric arc furnace [176-178].

Figure 110: Fusion with the three graphite electrodes.

The operation of the furnace is discontinuous. A charge can vary from a few ten kg to several tons, and may require from a few ten seconds to several hours for melting. Because of the very high melting temperatures of the oxides, a very specific technology is used. The furnace tank is made of a double-layer frame made of steel and cooled by water. The molten liquid solidifies in contact with the walls and forms an insulating layer, protecting the metal from the high melting temperature reached

during the process. The specific energy required to reach the pouring temperature of the mixtures varies from 1000 to 3500 kWh/ton. Furthermore, during the melting, it is possible to change the oxidation state of the refractory by immerging the electrodes in the molten bath or by leaving them outside this bath ("arc melting"). In the case the electrodes are immerged in the bath, a very reduced refractory is obtained. On the contrary, when the fusion of the raw materials takes place with the electrodes outside the bath, a well oxidized refractory is obtained [179].

Once the material is liquid, it is poured into moulds (Figure 111), before undergoing an annealing step.

Figure 111: Pouring in the moulds.

It is a critical step in the manufacturing process of fused-cast blocks since it conditions the residual stresses and so the quality of the final product. The quality of the refractory has to be optimal to ensure a good behaviour during the first rise in temperature of the glass furnace also called "heat-up of the furnace" and during the whole lifecycle of the furnace. The cooling rate is then controlled by adjusting the thermal conductivity of the powder agent in which the mould is placed. Depending on the size of the block, this annealing step can last between several hours to several weeks. The blocks are then machined and finally pre-assembled to verify that they fit all together (Figure 112).

Figure 112: Pre-assembly after machining.

ii. Particularities

Electrofusion process can create heterogeneities in the blocks. It can be shrinkage cavities, structural heterogeneities and sedimentation which can have an influence on the future behaviour of the material in contact with molten glass and so an influence on the final glass product.

The shrinkage cavity appears during the solidification as density of the liquid is lower than the density of the solid refractory. This contraction causes the formation of a void cavity in the poured refractory. To control the location of the shrinkage cavity, a riser, which is an excess of liquid poured in the mould, can be used.

The chemical sedimentation within the refractory blocks is due to the difference in density between the different components of the material. The heaviest components naturally end up towards the bottom, like zirconia because of their high density. There is therefore a difference in composition between the bottom and the top of the fused-cast block resulting in a heterogeneity of the final material.

Another type of heterogeneity concerns the microstructure which differs between the skin (surface) and the core of the blocks. In fact, the grains are finer and more elongated at the surface than at the core.

The electrofusion process can also lead to the creation of reduced products because of the use of graphite electrodes at high temperature. Chemically, this reduction is expressed by a reduction of the impurities contained in the products. For example, iron can be found as metal nodules in the final product [78].

We must therefore be very careful during observations because of all these heterogeneities. In our study, special cares were taken while collecting the test samples, to ensure the representativeness of the results.

C. GLASS MAKING FURNACE

The tank of a glass furnace (Figure 113) is divided into three parts: the melting zone (from the doghouse to the weir block), the refining zone (between the weir block and the throat) and the working end (from the throat to the feeder).

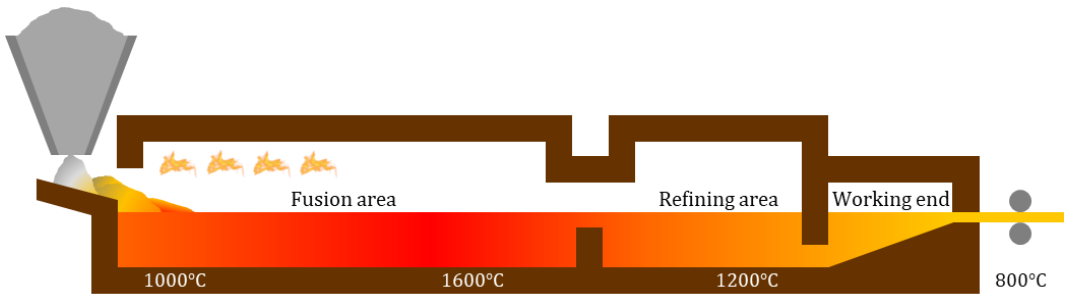

Figure 113: Different parts of glass tank furnace.

In the furnace there are several strong thermal gradients: between the inner and outer parts of the furnace, between the different areas previously defined and between the top and the bottom of the tank. In order to limit heat losses, a superstructure covers the entire tank [180].

As mentioned previously, the refining zone is an essential element in eliminating the bubbles formed during the fusion of the powders. This is the last step to remove the bubbles present in the glass matrix since the glass is then too viscous and traps the bubbles. However, this refining step is sometime not sufficient to eliminate the quantity of bubbles produced during melting.

D. CONDUCTIVTIY

i. Electrical conductivity of zirconia

At low temperatures, zirconium oxides are insulators but their conductivity increases with temperature. The main origin of the charge carriers is the defects created in the crystal lattice by thermal agitation or by the presence of impurities. In zirconia, conductivity has an ionic and an electronic contribution. Therefore, the charge carriers can be electronic (electrons or holes), ionic (oxygen vacancies or oxygen interstitials) or a mix of both contributions (MIEC = mixed ionic and electronic contribution). If the material is a mixed conductor (ionic and electronic), at low temperature the ionic conductivity is rather low and the conductivity of the material is rather electronic. It should be recalled that the mobility of electronic defects being $10^4/10^5$ times higher than the mobility of ionic point defects, a very low concentration of electronic defects can induce a significant electronic conductivity.

Monoclinic zirconia

Fundamental studies on monoclinic ZrO_2 without dopants have rarely been reported, maybe because of the difficulties in the manufacturing process and the mechanical instability of ZrO_2 to temperature variations [181]. Kröger proposed a Schottky type model involving both isolated oxygen vacancies and zirconium vacancies singly associated with oxygen vacancies [182] and Douglass and Wagner suggested an anti-Frenkel type model involving oxygen vacancies and interstitials [161]. It is predicted by both of these models that oxygen ionic conductivity may be considered to be predominant at moderate low oxygen pressures, between the extremes of n- and p-type electronic conductivity areas at low and high oxygen partial pressure.

According to Aldebert [115], monoclinic zirconia is a rather poor conductor, mainly electronic under air atmosphere. The determination of a low ionic conductivity is related to a low oxygen self-diffusion coefficient. By measuring hot-pressed samples, it has been reported that monoclinic ZrO_2 has extremely low electrical conductivity ranging from 2×10^{-6} S/cm to 6×10^{-5} S/cm at 990 °C [181].

According to Poulton and Smeltzer, monoclinic zirconia is an n-type electronic conductor at $pO_2 \leq 10^{-18}$ bar and a p-type electronic conductor at $pO_2 \geq 10^{-10}$ bar, with predominant oxygen ionic transport at intermediate pressures [183]. Electrical conductivity increases with increasing temperature at constant pO_2. At the lower temperatures, e.g. 600°C, conductivity changes less with pO_2 than at the higher temperatures (Figure 114) [130, 134].

The equilibrium with the oxygen partial pressure can be written:

$$\frac{1}{2}\, O_2 + \, V_O^{\bullet\bullet} + 2\, e' \, \leftrightarrow \, \, O_O^{\times} \quad (56)$$

or

$$\frac{1}{2}\, O_2 + \, 2\, e' \, \leftrightarrow \, \, O_i^{''} \quad (57)$$

Consequently, decreasing the oxygen pressure induces an increase of the electron concentration (the oxide becomes more electronic, by electrons), on the contrary, increasing the oxygen partial pressure induces a lowering of the electrons concentration, and so an increasing of the electron holes concentration, inducing an electronic conductivity of p-type. As shown in Figure 114, at high oxygen pressure, the electronic conductivity of zirconia is a p-type conductivity and at low oxygen pressure the additional conductivity is of n-type. Between ca. 10^{-10} and 10^{-18} atm, the ionic defects are the majority carriers.

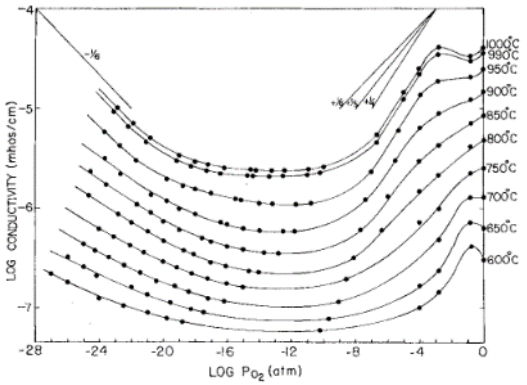

Figure 114: Effect of oxygen pressure on total electrical conductivity of ZrO_2 [130].

Tetragonal zirconia

A sharp increase of conductivity is observed at the monoclinic ↔ tetragonal transition [115]. According to Vest and al., tetragonal zirconia is a mixed electronic and ionic conductor. The n-type electronic conductivity observed at high temperatures and low oxygen partial pressures is interpreted on the basis of a defect model involving fully ionized oxygen vacancies (see equations (42) and (43)). Tetragonal zirconia is a mixed electronic and ionic conductor with a significant ionic contribution except for very low oxygen partial pressures as presented in Figure 115 [165].

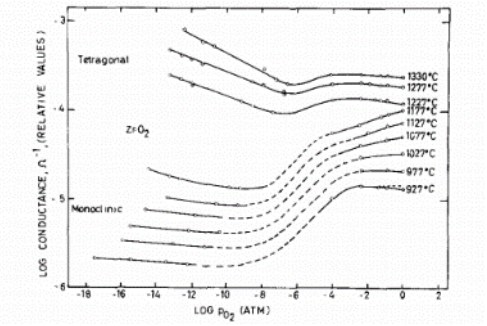

Figure 115: Conductance of the ZrO_2 specimen as a function of the partial pressure of oxygen [164].

Doped zirconia

The tetravalent Zr^{4+} can be substituted by trivalent Y^{3+} in the network leading to an increase of the oxygen vacancy concentration, according to:

$$Y_2O_3 = 2\,Y'_{Zr} + 3\,O_O^X + V_O^{\bullet\bullet} \qquad (58)$$

The same mechanism occurs for CaO, oxygen vacancies are formed when divalent calcium ions replace tetravalent zirconium ions [182, 184]:

$$CaO = Ca''_{Zr} + O_O^X + V_O^{\bullet\bullet} \qquad (59)$$

The ionic conductivity of trivalent oxide-stabilized cubic zirconia is higher than that of divalent oxide stabilized cubic zirconia [185].

The following nonstoichiometric defect reactions can be written, at low oxygen pressures [182, 186]:

$$O_O^X = 2e' + V_O^{\bullet\bullet} + \frac{1}{2} O_{2(g)} \qquad (60)$$

And at high oxygen pressures:

$$\frac{1}{2} O_{2(g)} + V_O^{\bullet\bullet} = O_O^X + 2h^{\bullet} \qquad (61)$$

The presence of doping elements with a valence higher than 4 (the one of zirconium) produces a reduction in oxygen vacancy concentrations, therefore a reduction in ionic conductivity.

$$Ta_2O_5 + V_O^{\bullet\bullet} = 2\,Ta_{Zr}^{\bullet} + 5\,O_O^X \qquad (62)$$

$$Nb_2O_5 + V_O^{\bullet\bullet} = 2\,Nb_{Zr}^{\bullet} + 5\,O_O^X \qquad (63)$$

$$V_2O_5 + V_O^{\bullet\bullet} = 2\,V_{Zr}^{\bullet} + 5\,O_O^X \qquad (64)$$

ii. Glass conductivity

Oxide glasses are the most common glasses. Oxide glasses are considered as solid electrolytes, because they are able to conduct ions. Evidently, this capacity of conduction depends on the type of glass and the elements to be transported through it. In fact, the transport of particles in the glass can be an ionic diffusion due to concentration gradients or a conduction of charged particles due to an electrical potential gradient.

In a simplified way, the phenomenon of diffusion can be described as the spontaneous movement of elements in an environment of heterogeneous composition, in the direction that tends to homogenize the environment, from the most concentrated to the least concentrated area. The rigorous description is more complex because, in concentrated environments, couplings between the movements of the different species can be witnessed [187].

The diffusive movement of ions in glasses is caused mainly by monovalent ions such as Li^+, Na^+, Ag^+ added intentionally as a network modifier or present as impurities. The movements of these cations affect several physical properties of glasses, as for example, electrical conductivity, electrical and mechanical relaxation [188].

Glasses are mostly ionic conductive since they contain alkali ions. Among the most used, the most mobile ions are Na^+. They are responsible for transforming bridging oxygens into non-bridging oxygens. In a general way, alkali glasses have ionic conductivity and non-alkali glasses exhibit a poor ionic conductivity [189, 190].

However, earth alkali ions increase the conductivity of glasses, but not as much as alkali ions. Moreover, the presence in the same glass of two alkaline ions or two alkaline earth ions creates an effect called « mixed alkali effect» which reduces the global ionic conductivity [191-193].

In silica-based glasses, Si is surrounded by 4 O in the form of a tetrahedron. The global composition being SiO_2 and not SiO_4, each O is shared between two Si. Each Si is linked by four bridging O to 4 other Si to form a network. For glasses with silica as forming oxide, the electronic contribution to the conductivity is very low and the charge carriers responsible for the conductivity are essentially the cations contained in the network.

Borate glasses are more resistant than silicate glasses for the same alkali content. The introduction of alkalis in silicate glasses leads to network cuts, while in borate glasses there are only bridging oxygen. On the other hand, adding boron to a siliceous glass does not prohibit the migration of Na^+ cations [190].

E. INFLUENCE OF IRON IN GLASS

As glass is made from raw materials, it inevitably contains impurities. The most common and so the most studied impurity is iron. Unless other special impurities are added in the composition, the color of the glass depends on its iron content. Color depends also on the conditions of production, which are influencing the impurities redox state. In glass melt and in final glass product, iron can be found in two redox states, Fe^{2+} and Fe^{3+}. At high temperature, Fe^{2+}, Fe^{3+} and the physically dissolved oxygen of a melt form an equilibrium [194-196]:

$$2\ Fe^{3+} + O^{2-} \rightleftarrows 2\ Fe^{2+} + \tfrac{1}{2}\ O_2 \qquad (65)$$

When the glass melt is cooled down, the equilibrium according to the equation (63) is shifted to the left side and the oxygen activity decreases. An increase in temperature leads to the reduction of the element, whereas a decrease in temperature corresponds to an oxidation of the element. If the molten glass is cooled quickly, only the physically dissolved oxygen can react with Fe^{2+} ions. The oxygen of the furnace atmosphere cannot participate because the diffusion coefficients are too low.

Several redox scales have been used by glassmakers. Since iron is systematically present in raw materials, glass manufacturers describe the oxidation state of glass as the ratio R between Fe^{2+} and total iron content (Fe^{2+} and Fe^{3+}) [20]:

$$R = \frac{[FeO]}{[Fe\ total]} \qquad (66)$$

However, this redox ratio is measured at room temperature and so the final redox ratio may not be representative of the redox conditions in the glass furnace at high temperatures. The equilibrium is shifted while changing the temperature [20, 51].

Iron was chosen to measure the oxidation state of a glass because it is always present in molten glass (at least at impurities level) but also because it strongly colors the glass. A visual estimation of the oxidation level of the glass is possible since the presence of Fe^{2+} colors the glass in blue and Fe^{3+} colors the glass in yellow. In industrial glasses the redox ratio varies between 0.1 for oxidized glasses and 0.9 for the most reduced glasses [197, 198]. The use of iron to measure redox state is therefore justified since R varies over the whole possible range. The equilibrium constant of reaction can be written:

$$K = \frac{a(Fe^{2+})^2}{a(Fe^{3+})^2} * \frac{P_{O2}{}^{\frac{1}{2}}}{a\,(O^{2-})} \qquad (67)$$

where $a\,(O^{2-})\frac{\gamma(Fe^{2+})^2}{\gamma(Fe^{3+})^2}$ is assumed equal to one; consequently, K can be written as [199]:

$$K' = \frac{[Fe^{2+}]^2}{[Fe^{3+}]^2} * P_{O2}{}^{\frac{1}{2}},\ then\ K'^{1/2} = \frac{[Fe^{2+}]}{[Fe^{3+}]} * P_{O2}{}^{\frac{1}{4}} \qquad (68)$$

The ratio of Fe^{2+}/Fe^{3+} (reduced to oxidized iron) in the glass melt is directly related to the partial oxygen pressure (proportional to the reciprocal fourth root of the partial oxygen pressure in the atmosphere) and the temperature [195]. Figure 116 shows the relationship between $R = \frac{[FeO]}{[Fe\ total]}$ and the oxygen partial pressure, at different temperatures.

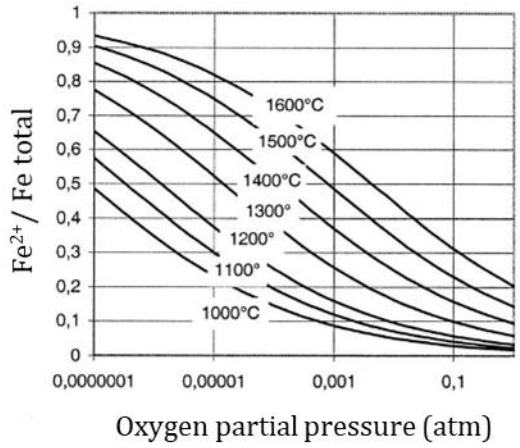

Figure 116: Relationship between pO_2 and R (redox state) as a function of temperature [195]

List of Figures

List of Tables

Résumé long

Durant la fabrication des verres, les matériaux tapissant les parois du four subissent de fortes sollicitations en raison de la composition de ces verres et de la température élevée de travail. Les matériaux choisis doivent être adaptés à ces conditions pouvant engendrer d'importants phénomènes de corrosion. Pour résoudre cette difficulté, Saint-Gobain SEFPRO développe et produit des réfractaires qui offrent de bonnes propriétés de résistance mécanique et chimique dans ces conditions extrêmes. Ces matériaux sont constitués d'un squelette de zircone (réfractaires électrofondus) et d'une phase vitreuse entourant cette phase cristallisée. Les matériaux réfractaires électrofondus avec un squelette zircone présentent une porosité ouverte très faible de l'ordre de 1% à 2% en moyenne. Les matériaux réfractaires frittés à base de zircon, également utilisés dans les fours verriers, présentent quant à eux une porosité ouverte généralement plus élevée pouvant atteindre jusqu'à 6%.

Un phénomène de bullage dans le verre fondu en contact de ces matériaux réfractaires peut avoir lieu lors de la fabrication du verre. Ce phénomène est d'une importance majeure car le bullage est source de défauts très problématiques dans les verres, dont une grande qualité est requise (verres électroniques, verre cristal, etc.). La maîtrise de ce phénomène présente donc un enjeu industriel important.

De nombreuses causes du bullage ont été identifiées dans des études passées, mettant notamment en cause la porosité du matériau réfractaire, les fissures présentes dans les blocs réfractaires, l'adsorption de gaz à la surface du réfractaire, l'affinage insuffisant du verre ou encore la présence d'impuretés dans le verre ainsi que des réactions électrochimiques entre le verre et le réfractaire. Cependant, aucun mécanisme complet expliquant le bullage dans sa globalité n'a pu être construit jusqu'à présent.

Il est vrai que le bullage est un phénomène complexe dans lequel interviennent de nombreux paramètres. L'objectif de cette recherche est de proposer un scénario cohérent du phénomène de bullage des verres au contact des réfractaires, afin de préciser les paramètres pertinents à l'origine du phénomène de bullage et d'établir un mécanisme du processus.

Le bullage d'un verre au contact de matériaux réfractaires est un phénomène difficile à mettre en évidence directement puisque peu de cas en conditions réelles d'utilisation sont précisément documentés. C'est pourquoi plusieurs tests en laboratoire, complémentaires à ceux déjà existants dans les centres de recherches de Saint-Gobain, ont été mis au point au cours de cette thèse afin de contrôler l'influence des différents paramètres. Ces expérimentations ont pour but d'étudier les matériaux réfractaires et de recréer le contact entre le verre et le réfractaire à haute température afin de construire le scénario de bullage d'un verre fondu en contact d'un matériau réfractaire à l'intérieur d'un four verrier.

Des caractérisations physico-chimiques et électriques des réfractaires étudiés ont été réalisées au cours de ce projet. Outre les tests standards réalisés à Saint-Gobain, des expériences XANES pour déterminer l'état redox des réfractaires ont été réalisées ainsi que des mesures de spectroscopie d'impédance en fonction de la température et de la pression partielle d'oxygène, afin d'estimer les conductivités ioniques et électroniques. Les réfractaires étudiés étant des matériaux composites biphasés, composés de zircone cristallisée et d'une phase vitreuse, des mesures de tomographie aux rayons X ont permis de reconstituer la distribution des deux phases afin d'évaluer leur éventuelle percolation et leur tortuosité en trois dimensions.

Des montages originaux ont également été réalisés au cours de ce travail pour des études in-situ du phénomène de bullage, comme des montages de semiperméation fonctionnant à haute température (jusqu'à 1500°C), couplés à un spectromètre de masse pour étudier les phénomènes de transport à travers le réfractaire et permettant l'étude « temporelle » du processus de bullage. De plus, un montage de goutte posée sous atmosphère contrôlée a été réalisé afin d'estimer la durée de vie d'une bulle dans les conditions étudiées.

Pour que le bullage ait lieu, il a été démontré que la température doit être suffisamment élevée afin que la viscosité du verre soit suffisamment faible pour permettre la nucléation des bulles. Cette viscosité limite sera atteinte à différentes températures en fonction de la composition du verre choisi.

Le réfractaire doit être complétement oxydé pour que le bullage se mette en place. Un matériau réfractaire est dit « oxydé » lorsque les impuretés de fer en présence sont oxydées. En effet, tant que le Fe(0) ou le Fe(II) captent l'oxygène pour s'oxyder et atteindre l'équilibre Fe(II)/Fe(III), l'oxygène ne sera pas disponible pour atteindre

l'interface verre/réfractaire et ainsi permettre le phénomène de bullage. Cependant, un matériau ne contenant pas d'impuretés de fer n'aura pas besoin de valider cette étape.

Les bulles engendrées par le phénomène sont uniquement composées d'oxygène et nous sommes en présence de matériaux très denses avec une porosité ouverte très faible. Le bullage n'est donc pas causé par une éventuelle perméabilité physique.

Étant donné la composition des bulles produites et la nécessité d'oxyder le réfractaire avant de pouvoir déclencher le bullage, l'atmosphère extérieure se doit d'être riche en oxygène. En effet, le bullage intense et permanent est absent sous atmosphère neutre.

Grâce à un montage développé au LEPMI, la présence du phénomène de semiperméabilité dans le mécanisme de bullage a pu être mise en évidence. Une différence d'activité en oxygène se crée entre la surface du matériau réfractaire en contact avec l'atmosphère et celle en contact avec le verre. Cependant, en configuration gaz | réfractaire | gaz, cette différence de pression partielle se retrouve nulle et ne peut donc plus être le moteur de la semiperméabilité à cause d'un phénomène de polarisation. C'est pourquoi la présence du verre fondu en contact du réfractaire est primordiale, ce dernier permettant d'évacuer l'oxygène qui pourrait s'accumuler à la surface.

Afin que la semiperméabilité puisse se produire, le matériau doit être un conducteur mixte, c'est-à-dire à la fois conducteur ionique et électronique. Une fois la semiperméabilité démontrée, la problématique majeure de ce travail de recherche a été de déterminer les chemins de la conductivité ionique et de la conductivité électronique.

Toutes les contributions électriques nécessaires au bullage se trouvent dans la phase zircone. Le rôle prépondérant de la zircone a ainsi été démontré au cours de cette thèse. En effet, plus le taux de zircone dans un réfractaire est élevée, plus le bullage est important. En conclusion, le flux dépend uniquement de la répartition de la phase zircone et non de la conductivité totale du réfractaire.

Pour qu'un bullage puisse se produire, les ions oxygène doivent pouvoir être acheminés de l'atmosphère extérieur jusqu'au contact avec le verre. Pour cela, un paramètre important doit être satisfait, la percolation de la phase zircone. Cette percolation varie en fonction du pourcentage de zircone et de la composition globale du matériau. En effet, la nature de la phase vitreuse associée peut influencer la

microstructure des grains zircone lors du procédé de refroidissement du bloc de réfractaire, au cours duquel les grains de zircone cristallisent.

L'arrêt du bullage a été observé dans le cas des matériaux électrofondus riches en zircone. Cet arrêt s'explique, soit par un blocage du flux d'ions oxygène O^{2-} à cause de la formation d'une couche isolante autour des grains de zircone ou à l'interface verre/réfractaire, soit à cause d'un changement de la chimie du verre, l'activité de l'oxygène de l'interface étant alors égale à celle en contact avec l'atmosphère extérieur.